UC Santa Barbara

UC Santa Barbara Electronic Theses and Dissertations

Title

Biomechanical Transmission as a Channel for Touch Information in Human Tactile Sensing

Permalink

https://escholarship.org/uc/item/8fm1x71b

Author

Tummala, Neeli

Publication Date

2024

Peer reviewed|Thesis/dissertation

eScholarship.org Powered by the California Digital Library
University of California

University of California
Santa Barbara

Biomechanical Transmission as a Channel for Touch Information in Human Tactile Sensing

A dissertation submitted in partial satisfaction
of the requirements for the degree

Doctor of Philosophy
in
Electrical and Computer Engineering

by

Neeli Tummala

Committee in charge:

Professor Yon Visell, Chair
Professor Michael Beyeler
Professor Elliot Hawkes
Professor Spencer LaVere Smith

September 2024

The Dissertation of Neeli Tummala is approved.

Professor Michael Beyeler

Professor Elliot Hawkes

Professor Spencer LaVere Smith

Professor Yon Visell, Committee Chair

June 2024

Biomechanical Transmission as a Channel for Touch Information in Human Tactile Sensing

Copyright © 2024

by

Neeli Tummala

Acknowledgements

This document would not exist without the support, encouragement, and guidance of many individuals.

I would like to thank my advisor, Yon Visell, for pushing me to become the researcher I did not know I could be. I am also deeply grateful to my Ph.D. committee, collaborators, mentors, and many inspiring colleagues I have met throughout my Ph.D. In particular, I would like to thank Hannes Saal, whose guidance and mentorship have been instrumental to my success; Stejara Dinulescu and Gregory Reardon, whose first- and co-first author works, respectively, are included in this dissertation; Yitian Shao and Bharat Dandu, whose research forms the core foundation for mine; and Spencer Smith, whose class inspired my future research trajectory. I am also especially thankful for the mentorship and guidance of Jerry Gibson, Stephanie Lin, Steve Conolly, and Brian Proulx.

I am grateful for the financial support I have received from U.C. Santa Barbara, the Link Foundation, the Society of Women Engineers, Women in Science and Engineering, and P.E.O. I am particularly thankful for the support of P.E.O. Chapter QA in Santa Barbara.

Finally, words on this page are not enough to express my immense gratitude and appreciation for my family and friends.

Curriculum Vitæ

Neeli Tummala

Education

2024	Ph.D. in Electrical and Computer Engineering, University of California, Santa Barbara.
2020	M.S. in Electrical and Computer Engineering, University of California, Santa Barbara.
2018	B.S. in Electrical Engineering and Computer Sciences, University of California, Berkeley.

Publications

Journal Articles

1. **N. Tummala**, G. Reardon, B. Dandu, Y. Shao, Y. Visell,"Pre-neuronal biomechanical filtering modulates and diversifies whole-hand tactile encoding," *bioRxiv*, 2024. Submission in progress.
2. G. Reardon, D. Goetz, M. Linnander, **N. Tummala**, Y. Visell, "Subwavelength Control of Vibrations in Thin Metamaterial Plates for Multitouch Surface Haptics," in preparation.
3. D. Goetz, G. Reardon, W. Heap, **N. Tummala**, Y. Visell, "Modal Vibrations of the Hand's Articulated Structure Shape Tactile Perception," in preparation.

Peer-Reviewed Conference Papers

1. **N. Tummala***, G. Reardon*, S. Fani, D. Goetz, M. Bianchi, Y. Visell, "SkinSource: A Data-Driven Toolbox for Predicting Touch-Elicited Vibrations in the Upper Limb," *2024 IEEE Haptics Symposium*, Long Beach, CA, 2024. (*Contributed equally)
2. **N. Tummala**, Y. Shao, Y. Visell, "Spatiotemporal Organization of Touch Information in Tactile Neuron Population Responses," *2023 IEEE World Haptics Conference (WHC)*, Delft, Netherlands, 2023, pp. 183-189.
3. S. Dinulescu, **N. Tummala**, G. Reardon, B. Dandu, D. Goetz, S. Topp, Y. Visell, "A Smart Bracelet for Tactile Communication and Interaction," *2022 IEEE Haptics Symposium*, Santa Barbara, CA, USA, 2022, pp. 1-7.

Awards

2024	**Best Conference Paper** *IEEE Haptics Symposium*, Long Beach, CA

2023	**Best Speaker Award** *Graduate Student Simulation Seminar*, Santa Barbara, CA
2023	**Best Talk Award** *Festival of Touch*, Marseille, France
2022	**Best Conference Paper Runner Up** *IEEE Haptics Symposium*, Santa Barbara, CA
2019, 2020, 2021	**Outstanding Teaching Assistant Award** *UC Santa Barbara*, Electrical and Computer Engineering Dept.

Scholarships and Fellowships

2023-2024	**Graduate Opportunity Fellowship** *UC Santa Barbara*
2023	**BD Biosciences Research Accelerator Award** *Women in Science and Engineering*, UC Santa Barbara
2023	**Amateur Radio Digital Communications Scholarship** *Society of Women Engineers*
2023	**Trainee Professional Development Award** *Society for Neuroscience Annual Meeting*, Washington D.C.
2022-2024	**Modeling, Simulation, and Training Fellowship** *Link Foundation*
2021, 2022, 2023	**Graduate Scholarships** *P.E.O. Foundation*
2021	**Intel Graduate Scholarhip** *Society of Women Engineers*

Professional Appointments

2019	**Research Intern**, Video Signal Processing Team *Teledyne FLIR*, Santa Barbara, CA

Abstract

Biomechanical Transmission as a Channel for Touch Information in Human Tactile Sensing

by

Neeli Tummala

The sense of touch arises from a complex interplay between biomechanical and neural processes that span large areas of skin. Little is understood about these processes and their interactions beyond the immediate area of touch contact due to experimental constraints on biomechanical and neural measurements. This Ph.D. dissertation addresses these challenges by developing data-driven computational methods to predict and analyze the widespread neuromechanical processes underlying manual touch. The research presented here seeks to answer the following questions: How does biomechanical transmission influence neural signals in the human tactile system, and what implications does that have for human tactile sensing in general? And how can we exploit biomechanical transmission for technology that interfaces with or takes inspiration from the human sense of touch?

This dissertation builds upon findings that manual touch interactions biomechanically transmit skin oscillations across the hand and arm (biomechanical transmission), exciting widespread mechanoreceptive sensory neurons (mechanoreceptors). Chapter 3 uses high-resolution optical vibrometry measurements of whole-hand skin oscillations to drive neural simulations of mechanoreceptor populations. The results demonstrate that the hand's biomechanics modifies skin oscillations in a frequency- and location-dependent manner that diversifies mechanoreceptor responses, enabling them to efficiently capture touch information. This research challenges existing characterizations of peripheral tac-

tile sensing and has implications for how tactile information is processed by the brain. Critically, this chapter emphasizes the importance of considering the influence of biomechanics on neural signals both at and beyond the location of touch contact.

Motivated by research conveying the significance of studying neural circuitry in natural settings, Chapter 4 extends the data-driven methodology presented in Chapter 3 to investigate whole-hand tactile encoding of active, unconstrained touch interactions. The results indicate that information about these interactions is organized within the spatial structure of the population responses at the level of individual digits. Additionally, this work demonstrates that biomechanical transmission enables mechanoreceptors in areas far from locations of touch contact to capture significant tactile information.

This concept of remote tactile sensing underpins the wrist-worn device developed in Chapter 5, which utilizes accelerometers to measure skin oscillations elicited by tactile sign language (TSL) letters performed on the hand. By extracting various temporal, spectral, and spectrotemporal features from these measurements and passing them into simple classifiers, the device achieves a translation accuracy of 94 %. This chapter presents the first digital input device for TSL users, enabling digital TSL transcription and communication by leveraging biomechanical transmission.

High-resolution measurements of skin oscillations, such as those employed in this dissertation, are often time- and resource-intensive. This presents an obstacle for touch research, given the demonstrated impact of biomechanical transmission on tactile sensing. To overcome these barriers, Chapter 6 introduces a free-to-use toolbox for predicting skin oscillations across the upper limb elicited by tactile stimuli applied at one or more locations on the hand. This toolbox enables the computational analysis of biomechanical transmission in the skin, reducing the need for physical measurements and supporting applications in neuroscience and haptics.

Contents

List of Figures

List of Tables

Chapter 1

Introduction

The sense of touch is critical for activities of daily living, which becomes evident when it is lost [5]. For instance, when tactile sensation in the hand is impaired due to anesthesia or neuropathy, mundane tasks like grasping a cup [6], lighting a match [7], or fastening shirt buttons [8] become prohibitively difficult, even when motor function is intact. The sense of touch supports these deceptively simple sequences of actions by relaying expected and, crucially, unexpected information about the environment to the brain.

Touch interactions performed with the hand modify its mechanical state through skin indentation, stretch, or vibration. The tactile sensation of these mechanical stimuli is primarily governed by a complex neuromechanical process that involves the biomechanics (structure and composition) of the hand and tens of thousands of widespread mechanoreceptive sensory neurons (mechanoreceptors) embedded in the skin. These mechanoreceptors encode touch information in sequences of electrical spikes that are transmitted to the brain, leading to the conscious perception of touch and supporting a variety of remarkable sensing and manipulation capabilities.

Technologies in fields such as robotics, prosthetics, and haptics seek to match these capabilities, but progress has been hindered by an incomplete understanding of the neu-

romechanical processes underlying the sense of touch. Technologies interfacing with other sensory systems have greatly benefited from knowledge about the interplay between biomechanics and neural signals. For example, research that revealed how the biomechanics of the ear dictates neural signals underlying human auditory perception revolutionized the cochlear implant [9, 10], making it the most successful neuroprosthetic device and restoring hearing to hundreds of thousands of people [11].

Two challenges maintain the gap in understanding the neuromechanical basis of the human tactile system. The first is accurately modeling or predicting the hand's biomechanical response during touch interactions. The hand is a heterogeneous network of multi-layered soft tissues, muscles, and skeletal structures. Adding to this complexity are touch-elicited skin oscillations that are biomechanically transmitted far from the location of touch contact, often across the entire hand and even the arm [1, 4, 12, 13, 14]. Thus, modeling or predicting changes in the mechanical state of the hand during touch events often requires simplifying assumptions or models restricted to a small region of skin.

The second challenge is measuring the responses of mechanoreceptor populations across the whole hand. It is currently only feasible to record the responses of a few mechanoreceptors at a time due to the significant time and precision required. However, any manual touch interaction excites thousands of mechanoreceptors across the entire upper limb due to the biomechanical transmission of skin oscillations [15, 16, 17]. While significant research has focused on understanding the responses of mechanoreceptors near the location of touch contact, far less is known about the responses of widespread mechanoreceptor populations, despite their contribution to perception [4, 17, 18].

Thus, characterizing and analyzing biomechanical transmission and mechanoreceptor responses across the upper limb will not only enable a more complete understanding of the human tactile system but also find widespread application in neuroscience, medicine,

robotics, prosthetics, and haptics. Toward this goal, this dissertation presents a data-driven method that combines biomechanical measurements with neural simulation to computationally predict the signals underlying human tactile sensing in the upper limb during manual touch interactions. This method is applied to elucidate the influence of biomechanical transmission on mechanoreceptor population responses in Chapter 3 and to investigate the structure of tactile information in whole-hand mechanoreceptor responses during natural touch interactions in Chapter 4. The findings demonstrate that biomechanical transmission supports tactile sensing by distributing diverse tactile information across large populations of spatially distributed mechanoreceptors. Chapter 5 introduces a wrist-worn device that translates tactile sign language by exploiting the biomechanical transmission of touch information to remote regions of skin. Finally, recognizing that skin measurements require significant time and resources, Chapter 6 presents a free-to-use toolbox enabling users to computationally predict skin oscillations across the upper limb elicited by arbitrary tactile stimuli applied to the hand.

The content and contributions of this dissertation are detailed in the following sections.

1.1 Overview

Chapter 2 serves as the foundational background to situate the research within this dissertation. It provides an overview of the biomechanical and neural processes underlying the human sense of touch, along with a review of previous studies that have measured, modeled, and analyzed these processes. By identifying gaps in existing literature, this chapter sets the stage for the contributions of this dissertation. Furthermore, Chapter 2 explores potential applications where the methods and insights derived from this research may prove beneficial.

Chapter 3, based on [19], employs data-driven neural simulations to examine the interplay between biomechanical and neural processes underlying manual touch interactions. This chapter extends beyond the typical focus on mechanoreceptors close to the stimulus contact site and examines neural responses across the entire hand. To overcome the practical challenges of measuring responses from mechanoreceptor populations, vibrometry measurements of skin oscillations across the whole hand are used to drive spatially distributed neuron models, each validated on recordings from individual mechanoreceptors. The findings reveal that as skin oscillations travel, they are modified by the biomechanics of the hand before they reach the widespread mechanoreceptors. This pre-neuronal biomechanical filtering, which varies with stimulus frequency and hand location, diversifies the response characteristics and spiking activity of whole-hand mechanoreceptor populations, thereby enhancing their ability to capture tactile information. These findings update widely held characterizations of mechanoreceptors, highlighting the importance of a population-level understanding of tactile encoding that integrates both neural and non-neural factors. Additionally, it sheds light on unexplained aspects of human touch perception and physiology, such as the perception of polyharmonic tactile stimuli and the distribution of mechanoreceptors in the hand.

While Chapter 3 offers valuable insights into whole-hand tactile encoding, the stimuli are delivered to a passive, restrained hand in a controlled laboratory setting. In contrast, Chapter 4, based on [16], is motivated by neuroscience research emphasizing the importance of studying sensory systems in natural settings. The data-driven methodologies from Chapter 3 are applied to study how commonly performed active touch interactions like tapping, grasping, and sliding are encoded by mechanoreceptor populations in the hand. Specifically, Chapter 4 explores how information about natural touch interactions is spatiotemporally organized within these population responses. To achieve this, it employs a matrix feature representation of spiking population responses and simple

classifiers, such as a support vector machine and k-nearest neighbors, to quantify the amount of encoded touch information. This work addresses open questions in touch research, including whether tactile information is encoded through the rate or timing of mechanoreceptor responses and how this information may be integrated spatially and temporally in higher-order somatosensory processing. The findings reveal that the spatial organization of responses is more crucial than the temporal organization, with most tactile information preserved when the spatial structure maintains separation between the digits. Additionally, Chapter 4 finds that mechanoreceptors distant from the location of touch contact encode significant tactile information. This result supports the findings from Chapter 3, showing that biomechanical transmission distributes tactile information to widespread mechanoreceptors throughout the hand.

Chapter 5, based on [20], introduces a wearable haptic device that captures touch information disseminated across the hand by biomechanical transmission. The device consists of four accelerometers mounted on the wrist that measure touch-elicited skin oscillations during the performance of tactile sign language (TSL) letters. These letters involve tapping, sliding, grabbing, and pinching gestures performed by the signer on the receiver's hand. By employing simple classifiers such as a support vector machine and a random forest, the device classifies TSL letters with an accuracy of 94 %. This chapter introduces the first digital input device for TSL users, facilitating TSL transcription for digital communication and important events like court proceedings. Additionally, the underlying principle and methodology of the device show promise for consumer wearables like smartwatches by leveraging biomechanical transmission to leave the hand unencumbered.

The skin measurements utilized in Chapters 3, 4, and 5 are time and resource-intensive, presenting an obstacle in touch research given the critical role of biomechanical transmission in the tactile system demonstrated by Chapters 3 and 4. Chapter 6, based

on [21], introduces a free-to-use toolbox for predicting touch-elicited skin oscillations across the upper limb in response to arbitrary tactile stimuli applied at one or more hand locations. This toolbox enables the computational analysis of biomechanical transmission in the upper limb, serving applications in haptics and neuroscience. Chapter 6 validates the methodology underlying the toolbox through several experiments that confirm the linearity of biomechanical transmission in the skin and compare the toolbox outputs with actual measurements across a wide range of frequencies. While the toolbox does not eliminate the need for skin measurements, it offers an accessible method to explore biomechanical transmission *in silico*, potentially saving researchers time and resources.

1.2 Contributions

This dissertation presents several contributions summarized here by chapter.

Chapter 3

- The experimental methodology introduced in Chapter 3 contributes the most biologically plausible representation of tactile encoding by whole-hand mechanoreceptor populations currently feasible. This data-driven approach employs optical vibrometry to capture biomechanically transmitted skin oscillations with high spatiotemporal resolution during localized tactile stimulation. These vibrometry measurements then drive a population of computationally simulated mechanoreceptors distributed throughout the hand. Their spiking responses are computed using neuron models extensively trained and validated on physiological data in prior research. Notably, this method yields spiking responses from mechanoreceptors not only adjacent to the site of touch contact but also those excited by widespread skin oscillations transmitted throughout the hand. The responses of

these remote mechanoreceptors have received little attention in prior research on tactile sensing. The method presented in Chapter 3 is a unique tool for examining tactile encoding by whole-hand mechanoreceptor populations and shedding light on subsequent processing in the brain.

- Chapter 3 leverages this data-driven method to analyze whole-hand biomechanical transmission and its role in distributing tactile signals to mechanoreceptors throughout the hand. The findings demonstrate that biomechanical transmission imparts filtering that alters the frequency content of tactile signals in a complex, location-dependent manner before neurotransduction. As a result, biomechanical filtering modulates and diversifies the responses of widespread mechanoreceptors, thereby increasing the encoding efficiency of tactile information in the hand. This research greatly revises widely accepted descriptions of these mechanoreceptors as having highly stereotyped response characteristics. Additionally, Chapter 3 highlights the role of biomechanical transmission in the encoding of tactile signals in the periphery, with implications for perceptual processing in the brain. This work has garnered recognition within the scientific community, evidenced by receiving the Best Talk Award at the 2023 Festival of Touch symposium.

Chapter 4

- Chapter 4 extends the data-driven methodology presented in Chapter 3 to analyze how a large dataset of active, unconstrained touch interactions is encoded by whole-hand mechanoreceptor populations. This research overcomes limitations in current neural recording techniques, which cannot measure mechanoreceptor population responses during unconstrained motion, to address the recognized importance of investigating neural processing in natural settings. Chapter 4 provides a basis for

future investigations on the under-explored topic of tactile encoding during natural touch interactions to illuminate both peripheral and central aspects of human tactile sensing.

- Chapter 4 is one of the first studies to analyze the spatial organization of touch information in whole-hand mechanoreceptor responses with high granularity, in contrast to the focus on temporal organization in prior research. The results demonstrate that tactile information is best encoded by mechanoreceptor population responses when the separation between digits is preserved within the spatial structure. This aligns with previous studies on the spatiotemporal structure of whole-hand skin oscillations during the same interactions. Moreover, the findings show that mechanoreceptors far from the contact location encode significant tactile information, supporting evidence that tactile perception can be preserved despite sensory impairment at the contact location. The methods and analyses conducted in Chapter 4 provide a versatile framework for future investigations into whole-hand tactile encoding by offering flexibility in manipulating the structure and feature representation of mechanoreceptor population responses in both space and time.

Chapter 5

- Chapter 5 introduces the first input device designed to support the digital communication of tactile sign language (TSL). For TSL users, this device enables remote communication and digital transcription of important events, such as court proceedings or personal milestones. Furthermore, the device achieves high classification accuracy of signed letters (94 %) using simple, unobtrusive, and unoptimized methods. This work opens avenues for future research, including real-time translation during TSL signing and decoding the emotion or sentiment conveyed by the

signer. The contributions of this work were recognized by the Best Conference Paper Runner-Up award at the 2022 IEEE Haptics Symposium.

- The research conducted in Chapter 5 leverages biomechanical transmission to decode touch interactions in a manner that leaves the hand unencumbered and does not compromise user privacy by recording video or other sensitive data. This work has the potential to guide the development of wearable consumer devices, such as smartwatches, to remotely interpret touch interactions for digital input.

Chapter 6

- Chapter 6 presents SkinSource, a free-to-use toolbox for predicting, visualizing, and analyzing touch-elicited skin oscillations in 3 axes across four different upper limbs. It is built upon a large dataset of vibrometry measurements obtained with an array of accelerometers placed on four participants. SkinSource allows users to computationally investigate biomechanical transmission across the entire upper limb for an infinitely large stimulus space. The toolbox enables the application of stimuli with diverse frequency and amplitude components at 20 different locations on the hand, either individually or simultaneously. Crucially, users can utilize SkinSource to systematically analyze biomechanical transmission entirely in computation, reducing the need for time-consuming or expensive measurements. The toolbox can support research on human tactile sensing and guide the design and engineering of haptic sensing and feedback devices. The significance of this work is highlighted by its receipt of the Best Conference Paper award at the 2024 IEEE Haptics Symposium.

- Chapter 6 demonstrates that the upper limb can be approximated as a linear transmission medium. This conclusion was reached through the analysis of high-resolution optical vibrometry measurements collected during the application of

tactile stimuli with a wide range of frequency and amplitude components. This finding enables the use of tools designed for analyzing linear time-invariant (LTI) systems, a mature area of research, presenting numerous opportunities for future investigations of biomechanical transmission. Additionally, these results validate the methodologies applied in both Chapter 3 and Chapter 6.

Chapter 2

Background

This chapter presents background and context for this dissertation, which focuses on modeling and analyzing the biomechanical and neural processes underlying human tactile sensing in the hand using data-driven methods.

Our hands are our primary tools for interacting with the world. We use them in a variety of exploration, sensing, and manipulation tasks to execute goal-directed movements and collect information from the environment [22]. But without the sense of touch, our hands are relatively ineffective. The impairment of tactile sensation by anesthesia, disease, or traumatic injury dramatically reduces the ability to perform manual tasks in a way that cannot be fully compensated for by other senses like vision and audition [5, 6, 7, 8, 23].

Underlying human tactile perception and manipulation capabilities is a complex neuromechanical process that begins with the biomechanics of the hand. A touch interaction, such as grasping an object, modifies the mechanical state of the hand by applying force, pressure, vibration, or stretch to the skin. The contact event between the skin and the object also generates skin oscillations that are biomechanically transmitted across the whole hand and even the arm. This transmission process is mediated by wave propaga-

tion in soft tissue and rigid body movement of the skeletal structure. Biomechanically transmitted skin oscillations are instrumental for texture perception [24], object manipulation [25, 26], and tool use [27]. Section 2.1 further discusses background on biomechanical transmission. Chapters 3 and 6 characterize biomechanical transmission across the upper limb with high spatiotemporal resolution, and Chapter 5 leverages biomechanical transmission in a haptic sensing device.

Changes in the biomechanical state of the hand directly drive neural circuitry that produces the sense of touch. Touch-elicited skin oscillations excite widespread mechanoreceptive sensory neurons (mechanoreceptors) embedded in the skin. Each mechanoreceptor encodes information about the touch interaction in trains of electrical spikes that are transmitted to the brain. How aspects of the touch interaction, such as force, edge orientation, or texture, are encoded by populations of mechanoreceptors is an open question. While prior work has made significant progress in understanding tactile encoding by small populations of mechanoreceptors near the location of contact between the skin and an object, less is known about the influence of biomechanical transmission on whole-hand mechanoreceptor population responses. Section 2.2 covers further background on tactile sensing in the human hand, Section 2.3 discusses the influence of biomechanics on sensory systems, and Chapters 3 and 4 analyze the role of biomechanical transmission in mechanoreceptor population responses.

The gap in knowledge about the interplay between biomechanical transmission and mechanoreceptor populations stems from two challenges. First, it is difficult to characterize biomechanical transmission due to the complex and heterogeneous morphology of the hand. Current methods for measuring and modeling biomechanical transmission during touch interactions often focus on small regions of skin or lack sufficient spatiotemporal resolution. Second, current techniques for measuring mechanoreceptor responses are time-consuming and tedious, precluding measurement from an entire population of

mechanoreceptors. Several simulations exist that combine mechanical and neural modeling to predict mechanoreceptor population responses, but these again focus on small regions of skin or rely on oversimplified assumptions. These challenges and prior works are further discussed in Sections 2.1 and 2.2. Chapter 6 presents an open-source toolbox for predicting touch-elicited skin oscillations, and Chapters 3 and 4 present a novel data-driven methodology for predicting whole-hand mechanoreceptor responses with high spatiotemporal resolution.

The work presented in this dissertation has implications for many areas, including neuroscience, medicine, prosthetics, robotics, and haptics. Section 2.4 provides more specific background in these application areas.

2.1 Biomechanical Transmission in the Hand

The human hand is a network of 27 bones and 29 muscles interconnected by a network of ligaments and tendons surrounded by skin [28]. Two types of skin cover the surface of the hand: glabrous skin on the volar surface and hairy skin on the dorsal surface. Glabrous and hairy skin differ in compliance, thickness, and nerve innervation. Hairy skin is thin and flexible, while glabrous skin is thick, inflexible, and covered in papillary ridges, which form fingerprints. The skin consists of several layers: the outer epidermis, the intermediary dermis, and the underlying hypodermis, which is composed of fat and connective tissue. The epidermis is composed of five sublayers, while the dermis is composed of two. These layers exist in both glabrous and hairy skin but are thinner and contain less connective tissue in hairy skin. While this dissertation incorporates measurements of biomechanical transmission in both types of skin (glabrous skin: Chapter 3; hairy skin: Chapters 4, 5, and 6), it focuses on the neural responses of mechanoreceptors embedded within the glabrous skin (Chapters 3 and 4).

2.1.1 Contact Biomechanics

During manual touch interactions, normal and tangential forces are applied to the skin at the location of contact. This results in a change in the mechanical state (stresses and strains) of the skin, which directly dictates the tactile information available to embedded mechanoreceptors. A large body of prior work has focused on measuring the local mechanical response of the skin during contact events, primarily at the fingertip. Such studies include the measurement of surface strain [29, 30, 31] and sub-surface deformations [32, 33] of the skin during touch interactions and biomechanical skin properties such as stiffness, thickness, and anisotropy [34, 35, 36, 37, 38] near the location of mechanical contact. Significant effort has also been applied to modeling the local biomechanical response of the skin during touch contact [39]. This includes analytical [40, 41], finite element [42, 43], and viscoleastic [38, 44] models. Notably omitted from this dissertation is the exploration of friction at the location of touch contact, a phenomenon that significantly influences contact biomechanics during tactile interactions [45, 46]. Although friction during touch is a rich area of study, it falls outside the scope of the work presented here.

2.1.2 Whole-Hand Biomechanical Transmission

In addition to local stresses and strains, touch contact elicits skin oscillations that are biomechanically transmitted across the entire hand and arm [1, 4, 12, 13, 14]. These oscillations contain information about the contact events that produce them—for example, the skin oscillations measured at the wrist during scanning of a texture at the fingertip contain frequency content that reflects the texture [12]. Chapter 5 leverages this property by using skin oscillations measured at the wrist to classify tactile sign language (TSL) letters signed on the hand. Both the soft tissues and the rigid skeletal structure of the

hand mediate biomechanical transmission.

The soft tissues of the hand exhibit both elastic and viscous behavior and permit the propagation of waves far from the location of contact during touch events. The propagation occurs through shear and compression waves in bulk tissue and through Rayleigh waves at the surface of the skin [47, 48]. Surface Rayleigh waves and shear waves dominate wave propagation in the tactile frequency range (0 to 1000 Hz), while compression waves dominate at frequencies outside of the tactile range ($>$ 5000 Hz). Surface Rayleigh waves and shear waves travel slowly through the skin at frequency-dependent speeds generally below 40 m/s. Within the hand, experiments have shown that these waves travel at speeds between 3 and 25 m/s [13, 49]. The resulting wavelengths are between approximately 10 and 100 mm in the tactile frequency range. Due to these relatively large wavelengths, surface Rayleigh waves experience little decay with depth within distances relevant to mechanoreceptors ($<$ 2 mm) [50]. Moreover, prior research has demonstrated that Rayleigh waves travel cooperatively through all skin layers [14].

Due to the skin's viscoelastic properties [35, 37], wave propagation is dispersive, imparting frequency-dependent attenuation to touch-elicited skin oscillations [4, 13, 49]. The attenuation of skin oscillations due to soft tissue viscoelasticity is monotonic with distance from the location of contact. However, Chapter 3 of this dissertation shows non-monotonic decay of skin oscillations with distance from the contact location, particularly at low frequencies. The areas of non-monotonicity correspond with anatomical features of the hand, such as the metacarpophalangeal joint (MCP) of the stimulated digit and the thenar and hypothenar eminences in the palm. These findings present evidence that the hand's skeletal structure and morphology affect the biomechanical transmission of touch-elicited skin oscillations. Prior research also supports the hand's morphology and skeletal structure playing a role in mediating biomechanical transmission [51, 52, 53].

2.1.3 Experimental Measurement Techniques

A number of methods are used to measure the biomechanical transmission of oscillations in the skin. Measurement methods that do not involve physical contact with the skin include laser vibrometry [4, 13, 38, 54, 55, 56] (Chapter 3), capacitative sensors [48, 47], and high-speed camera imaging [57]. Methods that involve physical contact with the skin include accelerometers [1, 20, 58, 59] (Chapters 4, 5, and 6), microphones [12], piezoelectric film sensors [60], phono cartridges [49, 61], and elastography [62]. These techniques have provided significant insights into biomechanical transmission in the skin. However, they can be difficult to perform because they are time-intensive and often require expensive or custom-made equipment. Moreover, the resulting measurements are often limited to small areas of skin or lack sufficient spatiotemporal resolution to capture whole-hand tactile information.

2.1.4 Computational Models

To address these challenges, several methods have been developed to model biomechanical transmission in the upper limb. These include simple viscoelastic mass-spring-damper models [38, 52, 63, 61], finite element models [64, 65, 66], equation-based analytical models [14, 57], and empirical models [4, 13, 67]. These prior works have provided detailed insight into the coarse biodynamic response or overarching properties of biomechanical transmission in the upper limb. However, these models employ simplifying assumptions that limit their accuracy or focus on small areas of skin, such as the fingertip, which limits their generalizability to predicting whole-hand mechanoreceptor population responses (Chapters 3 and 4).

Unlike the aforementioned examples of explicit models that describe biomechanical transmission with concrete equations or systems, this dissertation presents an entirely

data-driven implicit model for predicting touch-elicited skin oscillations across the whole hand (Chapter 3) and upper limb (Chapter 6). This method involves measuring the Green's function or impulse responses of the upper limb by applying a brief mechanical impulse to the hand and measuring the resulting skin oscillations with a laser Doppler vibrometer or an array of accelerometers. These measured impulse responses capture the physics of biomechanical transmission in the skin. With them, the skin oscillations elicited by an arbitrary input stimulus can be accurately predicted by convolving the stimulus with the impulse responses. This approach enables systematic computational experiments in lieu of time-consuming mechanical measurements. It is accurate because biomechanical transmission in the skin is linear and time-invariant (LTI), demonstrated by experiments in prior literature [54] and in Chapter 6 of this dissertation. This impulse response method has also been used for a variety of other applications, including RLC circuit analysis [68], audio processing [69], cerebral hemodynamic response modeling [70], and geophysics [71].

2.2 Tactile Sensing in the Hand

Tens of thousands of mechanoreceptors embedded in the glabrous skin mediate the neural process that follows changes in the biomechanical state of the hand [72, 73]. These mechanoreceptors transduce changes in the mechanical state of the skin into electrical impulses that signal information about the touch event to the brain. A main theme in this dissertation is understanding the role of whole-hand biomechanical transmission in tactile sensing by populations of mechanoreceptors in the hand (Chapters 3 and 4).

2.2.1 Mechanoreceptors

The term mechanoreceptor, as used in this dissertation, is a low-threshold mechanoreceptor (LTMR) afferent neuron that terminates in one or more mechanosensory end organs embedded in the skin [74, 75, 76]. LTMRs are myelinated Aβ nerve fibers with conduction velocities ranging from 16 to 100 m/s [74]. The mechanosensory end organs innervated by LTMRs vary in structure and location in the skin. These terminal end organs also play a role in biomechanically filtering the tactile stimuli (mechanical stresses) that excite the associated LTMR. While the exact mechanism of mechano-to-neural transduction varies based on LTMR subtype and end organ, it is generally mediated by mechanically gated ion channels located on the LTMR's axon terminals within the mechanosensory end organs [77, 78, 79]. Mechanical stimuli applied to the skin during touch events—such as pressure, stretch, or vibration–create mechanical forces that open the ion channels. This process alters the ionic concentration inside the cell, potentially leading to membrane depolarization. An electrical action potential, or spike, is generated if this depolarization reaches a sufficient voltage threshold.

Mechanoreceptors in the glabrous skin can be broadly classified into four main subtypes based on their response properties, which are determined by the specific mechanosensory end organ and subtype of LTMR innervating them [72, 80]. These mechanoreceptors are distinguished by two properties: the adaptation rate of their spiking responses to sustained indentation (rapidly adapting or slowly adapting) and the size of their receptive fields (Type I or Type II). Slowly adapting (SA) mechanoreceptors continue to respond throughout the duration of sustained indentations, while rapidly adapting (RA) mechanoreceptors primarily respond to changes in indentation, such as the onset or offset. Type I mechanoreceptors have small receptive fields and are located in more superficial layers of the skin, while Type II mechanoreceptors have larger receptive fields and are

embedded in deeper tissues.

Although the exact number and density of mechanoreceptors in the hand are unknown, there are estimated to be approximately 17,000 mechanoreceptors innervating the glabrous skin of an adult human hand [72, 81, 82]. Of those, 25 % are SA-I LTMRs that terminate in Merkel cell-neurite complexes located in the epidermis, 19 % are SA-II LTMRs that terminate in Ruffini corpuscles embedded in the dermis, 43 % are RA-I LTMRs that terminate in Meissner corpuscles situated in dermal papillae, and 13 % are RA-II LTMRs that terminate in Pacinian corpuscles that lie within the dermis. Although each type of mechanoreceptor is traditionally associated with the perception of specific stimuli (for example, SA-I LTMRs with the perception of coarse texture) [80], such distinctions can be misleading as all mechanoreceptor types are activated during most natural touch interactions [75, 83]. In this dissertation, mechanoreceptors are referred to by the name of their associated end organs (i.e., RA-II LTMRs innervating Pacinian corpuscle end organs are referred to as Pacinian corpuscle neurons).

Pacinian Corpuscle Neurons (PCs)

Of the four mechanoreceptor types, Chapters 3 and 4 of this dissertation focus on the Pacinian corpuscle neurons, or PCs. PCs are exquisitely sensitive to transient stimuli [84, 85], including widespread skin vibrations [86] that are readily excited during any touch interaction [1, 12, 26]. Due to their sensitivity and location in the deep dermis of the glabrous skin, PCs are described as having extensive receptive fields that encompass most, if not all, of the hand [87, 88]. Because of these characteristics, PCs play a crucial role in manual tasks such as object manipulation [25], texture perception [89], and tool use [26, 27].

The sensitivity of PCs arises from the highly sensitive RA-II LTMRs that innervate them, which respond to stimulus amplitudes as low as in the tens of nanometers [90].

The RA-II LTMRs terminate in corpuscle end organs, which are on the order of a millimeter and are composed of concentric lamellar cell layers surrounding the LTMR axon terminal [91, 92, 93]. This structure enables the corpuscle to biomechanically filter the mechanical stimuli before they excite the LTMR axon terminal [75].

More specifically, the surrounding corpuscle gives PCs their characteristic rapidly adapting properties [94] and sensitivity to vibrations between 20 and 1000 Hz [95]. The corpuscle also acts as a bandpass filter that endows PCs with frequency-dependent sensitivity [96]. PC frequency sensitivity can be quantified by determining the minimum amplitude of a sinusoidal stimulus required to elicit phase-locked spiking, or entrainment, where the PC fires once per cycle of the stimulus. PCs typically exhibit entrainment to oscillatory stimuli across a range of stimulus amplitudes [90, 97, 98], creating a nonlinear relationship between the stimulus amplitude and the PC firing rate—measured as the number of spikes per second. Entrainment threshold curves determined in numerous studies have revealed that PCs are most sensitive to frequencies between 200 and 300 Hz, with a rapid decrease in sensitivity at frequencies outside of this range, yielding a U-shaped curve [90, 93, 99, 100]. Furthermore, the frequency sensitivity of PCs, as determined by entrainment threshold curves, aligns with human perceptual thresholds for frequencies above 20 Hz [101, 102].

Due to their sensitivity and large receptive fields, PCs across the entire hand and arm are excited during manual touch interactions [15, 17, 18] (Chapters 3 and 4). The exact number of PCs in the glabrous skin of the hand is unknown but estimated to be in the hundreds [3, 103] to thousands [81, 82]. The density of PCs in the hand is also not fully known. It is estimated that PCs are present in the fingertips at a slightly higher density than elsewhere in the hand [81, 82]. Studies have also demonstrated that PCs are found concentrated near joints and along blood vessels [3, 103]. The relatively large number of PCs in the hand, coupled with their large receptive fields and extreme sensitivity, raises

questions about response redundancy among PCs in a whole-hand population. Chapter 3 explores this mystery, proposing that the filtering effects of hand biomechanics mitigate response redundancy by diversifying PC spiking activity.

2.2.2 Neural Pathway for Tactile Information

In humans, tactile information from peripheral mechanoreceptors regarding discriminative touch and proprioception travels along the dorsal column-medial lemniscal pathway to the brain [101, 104]. First, touch-elicited spikes propagate along the axon of the LTMR towards its cell body located in the dorsal root ganglia adjacent to the spinal cord. Once in the spinal cord, these signals synapse with second-order neurons that project to the thalamus, a relay station for sensory information. From the thalamus, third-order neurons convey tactile information to the primary somatosensory cortex (S1), the first major cortical site of tactile processing. From there, tactile information is transmitted to other areas of the brain, including the secondary somatosensory cortex (S2) and the primary motor cortex (M1). While S1 plays a critical role in touch perception, tactile information also undergoes initial processing at earlier stages of the pathway, including in the spinal cord dorsal horns [74]. This process underlies our conscious perception of touch and supports our manipulation capabilities. Sensations of pain, temperature, and crude touch are mediated by the spinothalamic tract, which is a different somatosensory pathway that also conveys conscious tactile information but is outside of the scope of this dissertation.

2.2.3 Neural Encoding of Tactile Information

Populations of mechanoreceptors excited by touch contact convey sensory information to the brain via electrical spikes. The amplitude of these spikes is constant and, therefore,

does not carry information. Rather, tactile information is conveyed by the frequency or timing of the spikes [105]. Understanding how tactile information is encoded in the spiking responses of mechanoreceptors in the hand and how that translates to perception is an open area of research with a multitude of applications in neuroscience, haptics, prosthetics, and other areas (Section 2.4). Although tactile perception during most touch interactions is a function of responses in all four types of mechanoreceptors [83], this section will mainly focus on tactile encoding by PCs.

Information theory, initially developed for the analysis of communication systems, provides a framework for understanding the neural encoding of sensory information [106]. It encompasses methods to quantify, analyze, and interpret the information content of neural signals, as well as how this information is encoded, represented, and transmitted within the nervous system. A concept borne out of information theory with particular relevance to this dissertation is the encoding efficiency hypothesis. This hypothesis posits that neural circuitry maximizes the amount of information encoded while minimizing redundancy [107, 108, 109, 110]. This concept has only been briefly explored in the context of tactile encoding [2]. Chapter 3 employs measures such as Shannon information entropy, latent dimensionality, and response correlations to demonstrate how biomechanical filtering supports tactile encoding efficiency by reducing redundancy across whole-hand PC populations. Chapter 4 further demonstrates how information theoretic techniques such as classifiers [111] and metric space analysis [112, 113] can be used to quantify the amount and elucidate the organization of tactile information within neural responses.

The specific mechanisms by which tactile information is encoded in mechanoreceptor responses—such as through rate coding or spike timing coding—remains a central question [114, 115, 116]. Rate codes rely on the number of spikes produced by a mechanoreceptor within a certain time period, while spike timing codes depend on the precise timing of individual spikes. Chapter 4 explores the implications of these codes for how PCs en-

code natural touch gestures. Prior research indicates that PCs primarily use spike timing coding, employing millisecond precision to convey details about the frequency content of tactile stimuli [112]. However, encoding stimulus intensity presents a more complex challenge for PCs due to their characteristic entrainment behavior—producing a set number of spikes per cycle of an oscillatory stimulus, regardless of variations in stimulus amplitude [90, 97]. This behavior results in response plateaus, with PC responses remaining the same across a wide range of stimulus amplitudes. Consequently, individual PCs cannot directly encode stimulus intensity.

This limitation highlights the importance of exploring responses from populations of PCs (and other mechanoreceptor types) to fully understand tactile encoding [83, 98, 117, 118]. Chapter 3 underscores this point by demonstrating that whole-hand PC populations encode more tactile information than a subset of PCs close to the location of contact. Furthermore, by considering PC population responses, Chapter 3 also sheds light on the open question of how humans perceive tactile signals with complex spectral content [119]. The findings demonstrate that PCs away from the contact location are tuned to a variety of frequencies outside of the typical 200 to 300 Hz range, providing support for unconfirmed hypotheses about the basis for the perception of polyharmonic stimuli [120, 121].

In addition to the importance of population response, neuroscience research highlights the need to study neural circuitry within the contexts for which it evolved—natural settings rather than only controlled laboratory conditions [122, 123, 124, 125]. While existing studies on natural sensory encoding have primarily focused on the visual and auditory systems [109, 126, 127, 128, 129], there is comparatively little research on tactile encoding of natural stimuli [1, 2, 15, 55, 130, 131] despite its acknowledged importance [132]. The limited exploration of natural touch can be attributed, in part, to the challenges posed by the precision and time demands of current peripheral neural recording techniques

(described further in Section 2.2.4). Chapter 4 seeks to overcome this challenge by leveraging data-driven simulations to elucidate how PC populations encode information about natural touch gestures.

2.2.4 Experimental Techniques for Measuring Mechanoreceptor Responses

There are various techniques for measuring spiking responses from mechanoreceptors in the hand. In humans, microneurography is the preferred method, involving the insertion of a tungsten needle electrode into the median or ulnar nerves of the upper limb [118, 133, 134, 135]. This method enables recordings from single mechanoreceptors in awake humans, allowing integration with psychophysical experiments. However, microneurography demands significant precision and time, making it infeasible to record responses from populations of mechanoreceptors. An alternative, less invasive approach involves the use of surface electrodes to record mechanoreceptor spiking responses [136, 137]. However, these measurements often have low signal-to-noise ratios and make it difficult to isolate signals from individual mechanoreceptors.

In contrast, fiber splitting [100, 112, 118] and dissection [138, 139] are standard recording techniques in animal studies that produce high quality measurements. However, these methods are highly invasive and require anesthetizing or sacrificing the animal, precluding measurements of mechanoreceptor responses during active or natural touch interactions. Additionally, these techniques do not preserve the influence of skin biomechanics on the spiking responses and are not feasible for population recordings.

Recent work has introduced an invasive method to measure responses from dorsal root ganglion (DRG) neurons in awake, freely moving animals, offering a new avenue to study mechanoreceptor activity in more naturalistic conditions [131]. Additionally,

there is ongoing development of non-invasive multi-site electrode arrays that enable the simultaneous recording of responses from multiple DRG neurons [140]. However, these technologies are still emerging and face challenges in widespread application.

Given the limitations of current mechanoreceptor recording techniques—such as the need for high precision, the restriction to single-unit recordings, and the requirement for controlled laboratory conditions—simulation emerges as a valuable tool. Simulations can overcome some of these constraints by allowing researchers to model mechanoreceptor population activity without the technical and ethical challenges of direct measurement. Chapters 3 and 4 present data-driven methodologies for simulating whole-hand PC population responses, while Chapter 6 contributes a toolbox for predicting the touch-elicited skin oscillations that drive mechanoreceptor responses across the upper limb.

2.2.5 Computational Models of Mechanoreceptor Responses

The challenges of neural recording techniques for measuring mechanoreceptor responses necessitate simulation to better understand tactile encoding in the human hand [117]. Various neuron models, including integrate-and-fire [141, 142, 67, 143], Izhikevich [144], Hodgin-Huxley [145], and Freeman-Johnson [146, 147] models, have been developed to simulate the spiking responses of individual mechanoreceptors. These models focus on the responses of isolated receptors, disregarding the influence of skin biomechanics. Integrate-and-fire, Izhikevich, and Hodgkin-Huxley neuron models simulate the dynamics of the mechanoreceptor's membrane voltage to predict neuronal firing patterns in response to stimuli, while Freeman-Johnson models are specifically focused on the empirical response characteristics to vibratory stimuli without directly simulating the underlying membrane voltage dynamics. Other less common models exist, such as an electromechanical circuit model combined with a spike synthesizer [148]. Of the

model types, integrate-and-fire neuron models are the most popular due to their simplicity and computational efficiency, making them suitable for population simulations. More complex models like the Hodgkin-Huxley or Izhikevich models are preferred when there is a need to analyze neuronal firing patterns beyond simple spiking. While these models provide valuable insight into neural encoding by individual mechanoreceptors, a comprehensive understanding of tactile encoding necessitates simulations that consider population responses and integrate the skin's biomechanical contributions [149].

Various approaches have been developed to model the population responses of mechanoreceptors, each differing in how they simulate the mechanical response of the skin and the resulting spiking responses of mechanoreceptors [117, 149]. Broadly, the mechanical component of these simulations can be categorized into data-driven models [67, 98, 143, 150], finite-element models [151, 152], and analytical models based on continuum mechanics [153]. For the mechanoreceptor responses, methods range from integrate-and-fire [67, 143, 152, 154] and Hodgkin-Huxley [151] neuron models to data-driven firing rate equations [98, 150, 153]. These simulations have significantly advanced our understanding of tactile encoding by mechanoreceptor populations, revealing insights into how mechanoreceptors collectively encode aspects of tactile stimuli, such as vibration intensity [98, 150], edge orientation [155], tool interactions [27], and various standard experimental stimuli [15].

However, each simulation approach has limitations, which typically include constraints to modeling only a small skin area, oversimplifications in biomechanical skin responses or neural response mechanisms (i.e., modeling only the firing rates rather than precise spike timing), or prohibitive computational demands. To address these challenges, Chapters 3 and 4 present a technique for simulating whole-hand PC population responses. This method leverages data-driven predictions of widespread biomechanical transmission to drive integrate-and-fire neuron models [67] trained and validated on neu-

rophysiological recordings [98]. Chapter 6 further details the data-driven approach for predicting biomechanical transmission across the upper limb. This computationally efficient approach achieves high spatiotemporal resolution in modeling both biomechanical and neural responses across the whole hand.

2.3 Pre-Neuronal Biomechanics in Sensory Systems

Pre-neuronal biomechanical processes mediate neural circuitry in many sensory systems. In the vestibular system, the body's biomechanics shape the statistics of natural vestibular stimuli prior to neural processing [156]. A more well-studied biomechanical system is the basilar membrane in the cochlea, which acts as a biomechanical filter that maps acoustic signals to vibrations that excite auditory nerve fibers at frequency-specific locations on the membrane before neural processing [157, 158]. Moreover, the cornea and lens of the eye act as biomechanical filters that focus light onto the retina [159, 160]. The role of pre-neuronal biomechanics in sensory neural processing has also been studied in other animals, such as how the mechanical properties of whiskers influence tactile sensing information available to the rodent vibrissal system [161, 162, 163]. In short, the pre-neuronal effects of biomechanics cannot be decoupled from underlying sensory neural processes—they must be studied together [164, 165, 166].

Understanding the interplay between the biomechanical and neural processes in sensory systems is important for several applications, including sensory neuroscience, medicine, biomedical engineering, and artificial sensing systems. In sensory neuroscience, studying this interplay sheds light on sensory system function and human perception [167], as well as insights into the evolutionary adaptations of sensory systems [14, 168, 169]. Cochlear implants [9, 10] and diagnoses and corrective interventions for vision loss [170] are prime examples of how knowledge about pre-neuronal biomechan-

ics can also lead to advances in medicine and biomedical engineering. Knowledge about the effect of biomechanical processes on neural processes has also been leveraged for artificial sensing systems, such as biomimetic tactile sensors [171] and robotic whiskers [172]. Such applications are further discussed in Section 2.4.

2.3.1 Tactile System

In the tactile system, the skin is the primary interface between the environment and the mechanoreceptors. Therefore, changes in the biomechanical state of the hand, local or otherwise, directly mediate the neural responses of mechanoreceptors embedded in the skin that eventually give rise to tactile perception. Prior research has identified pre-neuronal effects of biomechanics in the tactile system, such as introducing response latency [137, 173]. Moreover, the viscoelastic nature of the skin has been shown to play a role in mechanoreceptor responses by acting as a low-pass filter [174] and retaining memory of prior mechanical stimuli [175]. Importantly, research has demonstrated that hand biomechanics perform pre-neuronal computations on tactile signals, potentially aiding subsequent neural encoding and perceptual processing [2, 30] (Chapter 3). Indeed, biomechanical transmission has provided an explanation for some surprising aspects of human touch perception [4, 17, 18, 56]. Work presented in this dissertation may shed light on unexplained aspects of human touch perception, such as the perception of complex vibrotactile stimuli [119, 120, 121] and intensity [98].

Critically, studying biomechanical transmission in the skin facilitates the simulation and analysis of mechanoreceptor population responses [67, 149], which is crucial for developing a comprehensive understanding of the tactile system [25, 83, 117]. For example, it enables the analysis of the spatial and temporal organization of touch information in mechanoreceptor population responses [15] (Chapter 4), addressing important questions

in sensory neuroscience, such as rate versus spike timing codes [112, 114, 115, 116]. Furthermore, analysis of biomechanical transmission has revealed evolutionary insights into the tactile system, such as how wave propagation dictates the depth of PCs in the skin of various mammals [14]. Such studies exploring the evolutionary aspects of sensory systems provide a unique lens into biomechanical and neural architecture and morphology. Chapter 3 may shed light on other evolutionary aspects of the human tactile system, such as encoding efficiency [2] and the number [81, 82] and distribution [3, 103] of PCs in the hand.

Understanding the relationship between biomechanics and peripheral neural encoding in the tactile system, especially at the population level, is challenging due to experimental constraints. Computational methods combining mechanical and neural data have been developed to address this, providing new insights into the tactile system. For instance, these methods have been applied to study tool use [27], proprioception [176, 177], and the detection of dynamic tactile signals [61]. Similarly, this dissertation applies computational modeling and data-driven simulations to investigate neuromechanical interactions within the hand at the population level, contributing an approach that overcomes experimental constraints to improve our understanding of the human tactile system.

2.4 Application Areas

The work in this dissertation on measuring and predicting biomechanical transmission in the upper limb and investigating the subsequent effects on whole-hand mechanoreceptor population responses has applications in a broad range of areas, including medicine, prosthetics, robotics, and haptics. Specific applications and prior work in these areas are described in the following subsections.

2.4.1 Health and Medicine

The biomechanical properties of the skin change with age [178, 179]. Aging also causes changes in mechanoreceptor morphology, function, and density [82, 180]; for example, it is hypothesized that the number of PCs in the hand decreases with age [92, 103]. These changes lead to a decline in tactile sensitivity [181] and spatial acuity [182], which can significantly affect daily functioning and quality of life. As a result, understanding age-related biomechanical and neural changes is an active area of research. The mechanical properties of the skin also change as a result of various diseases such as scleroderma or Ehlers-Danlos syndrome [39].

Research has been conducted to develop diagnostic methods for these diseases and age-related changes by characterizing the mechanical properties of the skin. Methods include applying vibrations and measuring resulting wave propagation [36, 62, 179, 183] or developing models of biomechanical transmission in the skin to provide a computational diagnostic testbed [38, 57]. Another study introduced a method to quantify skin deformation during the application of von Frey monofilaments [184], which are commonly used to assess a decline in tactile acuity and sensitivity due to neuropathy, stroke, or traumatic injury. Moreover, measuring and modeling biomechanical transmission aids in understanding the impact of extended vibration exposure, common in occupational power tool use [52, 53, 63, 185].

2.4.2 Tactile Sensory Prostheses

By 2050, it is estimated that 3.6 million individuals in the United States will be living with limb loss [186], a deficit that significantly impacts day-to-day function and quality of life [187]. Prosthetic limbs have been developed to replace the lost limb. Traditionally, the focus of prosthesis development has been forward kinematic control rather than tactile

feedback [188]. However, studies have demonstrated that daily activities are prohibitively difficult to perform without the sense of touch [5, 6, 7, 8, 23]. This underscores the need for developing tactile feedback methods [189], which significantly improve user acceptance, embodiment, confidence, and task performance [190, 191].

At the periphery, methods for conveying tactile feedback include nerve stimulation and sensory substitution via mechanical or electrical feedback [192, 193, 194]. Sensory substitution devices have also been developed for individuals who have lost tactile sensation due to circumstances such as diabetic neuropathy, stroke, or traumatic injury [195, 196]. Among the most promising approaches for providing informative and realistic feedback are biomimetic methods that mimic the human tactile system [197, 198, 199, 200, 201, 202, 203, 204]. A better understanding of the influence of biomechanics on mechanoreceptor responses could help bridge the gap between artificial tactile feedback and the rich sensations felt from an intact, fully functional limb. Similar to how insights into the interplay between biomechanics and neural encoding in the auditory system have been pivotal in developing the cochlear implant [9, 10]—a sensory prosthesis that has restored hearing for hundreds of thousands of individuals [11]—analogous understandings in the tactile system could inform advancements in prosthetic limbs. Tactile feedback in prosthetic limbs also involves sensing tactile information from the environment, which is discussed in the following section on robotics.

2.4.3 Robotic Tactile Sensing

A longstanding goal in robotics is to develop robots that can perform dexterous manipulation tasks at or above the level of their human counterparts. Significant research has focused on developing artificial tactile perception for robots [205], given that tactile feedback is crucial for manipulation and sensing tasks [6, 8]. A promising approach,

like for prosthetic limbs, is to draw inspiration from the human hand and its underlying tactile system [206, 207, 208, 209, 210]. This has led to the creation of electronic skins (e-skins), often composed of a soft skin-like polymer with embedded sensors that function as artificial mechanoreceptors [171, 211, 212]. Along with these advances in hardware, biomimetic algorithms reflecting how mechanoreceptors encode tactile information in their spiking responses have been developed [213, 214, 215, 216, 217, 218, 219].

Advancements in understanding the population encoding mechanisms of mechanoreceptors in response to diverse tactile interactions may enable more flexible and robust artificial perception algorithms. Additionally, with e-skins that act as biomechanical transmission mediums, tactile information can be widely transmitted beyond the immediate point of contact with the environment, as in the skin. Knowledge and concepts from studying biomechanical transmission in the human hand can then be applied to artificial tactile sensing. For example, Chapters 3, 4, and 5 demonstrate that sensors can be situated remotely from the contact site, which not only improves robustness but also reduces device complexity, allowing a more sparse distribution of sensors [220].

2.4.4 Haptic Technologies

Haptic technologies interface with the sense of touch. Perhaps the most common haptic devices are smartphones or tablets that provide simple vibration feedback when receiving a notification or typing on a keyboard. Haptic feedback devices are also becoming increasingly prevalent for gaming, virtual and augmented reality (VR/AR), teleoperation, and interpersonal communication. Since most haptic devices first interface with the skin, biomechanical transmission plays a role in haptic device use and, in some cases, can be leveraged for sensing and feedback purposes.

Tactile Sensing

Touch-elicited skin oscillations transmit information about the contact events across widespread areas of skin [12]. Such acoustic information can be captured remotely from the contact location using wearable sensors, such as accelerometers [1, 58] and microphones [12], and interpreted using feature extraction and classification methods. The skin can then become a versatile input device, allowing users to perform touch interactions that can be digitally identified or transcribed [221]. For example, wearable haptic devices that measure biomechanical transmission have been developed to recognize touch interactions at various locations on the body [60, 222, 223] or external surfaces [224] for digital interface manipulation. Chapter 5 presents a haptic wristband device that digitally transcribes tactile sign language letters signed on the hand by leveraging biomechanical transmission.

Haptic Feedback

Haptic devices that deliver mechanical feedback, such as vibration, generate widespread skin oscillations. Studies have shown that it is important to consider biomechanical transmission when developing haptic feedback devices because it plays a role in touch perception [59, 225]. Notably, feedback-elicited skin oscillations can impact perception in unexpected or unwanted ways, such as diminishing a user's ability to sense the direction of a stimulus [56]. But, biomechanical transmission can also be harnessed to create novel haptic feedback techniques. For example, a prior study developed a method using a single actuator to create sensations that spatially expanded or contracted by leveraging the frequency-dependent attenuation properties of the skin [4]. Additionally, biomechanical transmission has been utilized to enhance interpersonal communication [226] and to focus sensation at a specified location on the arm [227]. Developing

a better understanding of biomechanical transmission in the skin may enable the creation of new haptic feedback devices and techniques for more realistic and diverse tactile experiences. Chapter 6 allows users to computationally test haptic feedback patterns or sensing paradigms that leverage biomechanical transmission, which may guide haptic device design.

Chapter 3

Pre-neuronal Biomechanical Filtering Modulates and Diversifies Whole-Hand Tactile Encoding

During manual touch interactions, widespread mechanoreceptors are excited by skin oscillations transmitted biomechanically across the whole hand. However, little is understood about how biomechanical transmission influences the responses of mechanoreceptors, particularly outside the region of direct touch contact. This chapter characterizes the filtering effects of hand biomechanics on skin oscillations using high-resolution vibrometry measurements. It further develops measurement-driven neural simulations to understand the impact of biomechanical filtering on whole-hand mechanoreceptor population responses. The data-driven methodology introduced here is extended in Chapter 4 to analyze whole-hand tactile encoding of natural touch interactions, while Chapter 6 adapts the biomechanical aspect into a free-to-use computational toolbox for applications in neuroscience and haptics. Additionally, Chapter 5 presents a wearable haptic sensing device that leverages biomechanical transmission to translate tactile sign language.

The content of Chapter 3 is adapted from [19]:

N. Tummala, G. Reardon, B. Dandu, Y. Shao, H. P. Saal, Y. Visell, Pre-neuronal biomechanical filtering modulates and diversifies whole-hand tactile encoding. *bioRxiv*, 2024. DOI: `https://doi.org/10.1101/2023.11.10.565040`.

Abstract

Touching an object elicits skin oscillations that are biomechanically transmitted throughout the hand, driving responses in numerous exquisitely sensitive Pacinian corpuscle neurons (PCs). Previous studies have documented PC response properties using stimuli applied adjacent to the receptor location. However, activity in the majority of PCs is evoked by transmitted skin oscillations that are further modified by biomechanical filtering. The significance of this filtering mechanism and its influence on tactile processing have not been elucidated. Here, we combined vibrometry imaging and computational experiments to characterize the effects of biomechanical filtering on spiking activity in whole-hand PC populations. We observed complex, distance- and frequency-dependent patterns of biomechanical filtering shaped by tissue mechanics and hand morphology. This biomechanical modulation diversified PC population spiking activity, enhancing tactile encoding efficiency. These findings indicate that biomechanics furnishes a pre-neuronal mechanism that facilitates efficient tactile processing.

Significance

Manual touch interactions initiate a dynamic interplay between the biomechanics of the skin and the responses of tactile sensory neurons throughout the hand. The properties

of isolated sensory neurons have been described, but the influence of biomechanics on neuronal population responses is not well understood. Our study uses mechanical imaging and computational techniques to reveal the prominent effects of skin biomechanics in modulating and diversifying the responses of widespread sensory neurons. This research highlights the value of an integrative, population-level understanding that accounts for both neural and non-neural factors in sensory processing. Our findings also suggest that the brain should integrate information from widely distributed sensory neurons, an idea that has implications for neuroscience, haptic engineering, and sensing technologies

3.1 Introduction

The sense of touch is stimulated when the skin comes into contact with the environment. During such contact events, perceptual information is often regarded as originating from the responses of tactile sensory neurons terminating near the contact location. But the sense of touch is also invoked when the environment is explored indirectly through a probe, such as a tool, fingernail, or whisker. Such probes are not innervated by sensory neurons. Instead, perceptual information is mediated by "internal contacts" that biomechanically couple the probe to skin innervated by tactile sensory neurons [228]. The same biomechanical couplings that mediate indirect touch are also involved during direct touch. In both cases, these couplings facilitate the transmission of touch-elicited skin oscillations to regions far from the contact location [14, 48], which excites remote tactile sensory neurons [174].

Indeed, manual touch interactions, such as texture exploration [12, 24], dexterous manipulation [25], and tool use [27], generate prominent skin oscillations that are transmitted across the hand. The biomechanics of the hand transforms localized contact forces into spatially distributed skin oscillations that carry information about the initial con-

tact event [1, 12, 55]. These oscillations excite widespread Pacinian corpuscle neurons (PCs) [13, 14, 15, 16] that encode the transmitted tactile information in their spiking responses.

There is ample evidence that the brain exploits these widespread skin oscillations and PC responses in touch perception. For example, humans can discriminate between different surface textures [17] or vibration frequencies [18] applied to their anesthetized finger by exploiting information transmitted to remote PCs. The perceptual significance of widespread PC responses is also exemplified by vibrotactile summation and masking effects between stimuli applied at distant hand locations [229, 230]. These perceptual results are consistent with observations that PCs readily respond to subtle vibrations of the ground or other substrates evoked by a distant contact event [84, 131]. In several species, this facilitates the detection of substrate vibrations for long-range perception and communication [231, 232]. Indirectly evoked PC responses also mediate the perception of contact events during object manipulation and tool use [25, 26, 27].

Recent studies suggest that the biomechanics of the hand modifies transmitted skin oscillations by applying filtering effects, such as the frequency- and location-dependent attenuation imparted by the soft tissues of the hand [4, 13]. However, the modulatory effects of biomechanical filtering on PC spiking activity throughout the hand are unknown. Existing peripheral neural recordings reveal PC response characteristics to be highly stereotyped, with the highest frequency sensitivity between 200 to 300 Hz [90, 93, 97, 99, 100]. These recordings, however, are obtained from PCs adjacent to the stimulus contact location. As a result, they do not capture the effects of biomechanical filtering that would modulate the responses of more distant PCs. Thus, the influence of biomechanical filtering on tactile encoding by whole-hand PC populations and its implications for tactile sensing has received little prior attention.

It is not straightforward to deduce the influence of hand biomechanics on PC pop-

ulation responses due to the complex and heterogeneous morphology of the hand. Furthermore, extant experimental techniques preclude the simultaneous recording of neural signals from populations of PCs [149]. To overcome these limitations, we captured high-resolution vibrometry measurements of skin oscillations across the whole hand. We then used these measurements to drive whole-hand populations of spiking PC neuron models. We first analyzed the vibrometry measurements to determine the frequency- and location-dependent patterns of biomechanical filtering across the hand. Using our data-driven neural simulation methodology, we then characterized the influence of biomechanical filtering on the tuning characteristics of individual PCs distributed across the hand and on tactile encoding by whole-hand PC populations. Our findings reveal that biomechanical filtering furnishes a pre-neuronal mechanism that modulates and diversifies PC spiking activity across the hand, thereby supporting efficient tactile processing in the periphery.

3.2 Imaging Whole-Hand Biomechanical Transmission

We characterized the transmission of skin oscillations across the glabrous skin of several human hands (n = 7, P1 to P7). Mechanical impulses (0.5 ms duration) were applied at four distinct contact locations, and evoked skin oscillations were recorded at 200 to 350 spatially distributed locations via optical vibrometry (sample rate 20 kHz, grid spacing 8 mm; see Methods, and Fig. 3.1A). These impulse measurements characterized biomechanical transmission across the hand within the frequency range relevant to PCs (20 to 800 Hz). The dispersive nature of biomechanical transmission altered both the temporal structure and frequency content of skin oscillations (Fig. 3.1B, D). As a consequence, we

observed the pairwise temporal and spectral correlation of skin oscillations at different locations to decrease with increasing pairwise distance (Fig. 3.1C, D)).

Due to the linearity of biomechanical transmission in the small signal regime [21, 54], the impulse measurements accurately encoded the transmission of skin oscillations in the hand, which was confirmed in validation experiments (Fig. 3.5). This allowed us to compute the whole-hand skin oscillations that would be evoked by an arbitrary input waveform by convolving the input waveform with the impulse measurements (see Methods, and Fig. 3.6A). Using this technique, we computed the skin oscillations evoked by diverse tactile input signals, including sinusoids, diharmonics, and bandpass-filtered noise, via *in silico* experiments. This method preserved the effects of biomechanical filtering, including the phase and amplitude of evoked skin oscillations (Fig. 3.1E, F).

3.3 Biomechanically Mediated PC Spiking Activity

PC spiking responses are driven by deformations of the corpuscle caused by mechanical oscillations of surrounding tissues [93]. Thus, we sought to characterize the influence of biomechanical filtering on PC spiking responses. However, current experimental techniques preclude the *in vivo* measurement of PC population responses [149]. To overcome this limitation, we determined the spiking responses of whole-hand PC populations *in silico*, using the computed skin oscillations to drive a population of spiking PC neuron models that were fit to physiological data in prior research [67] (Fig. 3.6A). Each PC neuron model was driven by skin oscillations at its location in the hand. The spatial distribution of PCs across the hand was selected based on findings from a prior anatomical study [81]. We used this methodology to obtain whole-hand PC population spiking responses evoked by arbitrary tactile inputs supplied at any of four contact locations on the hand.

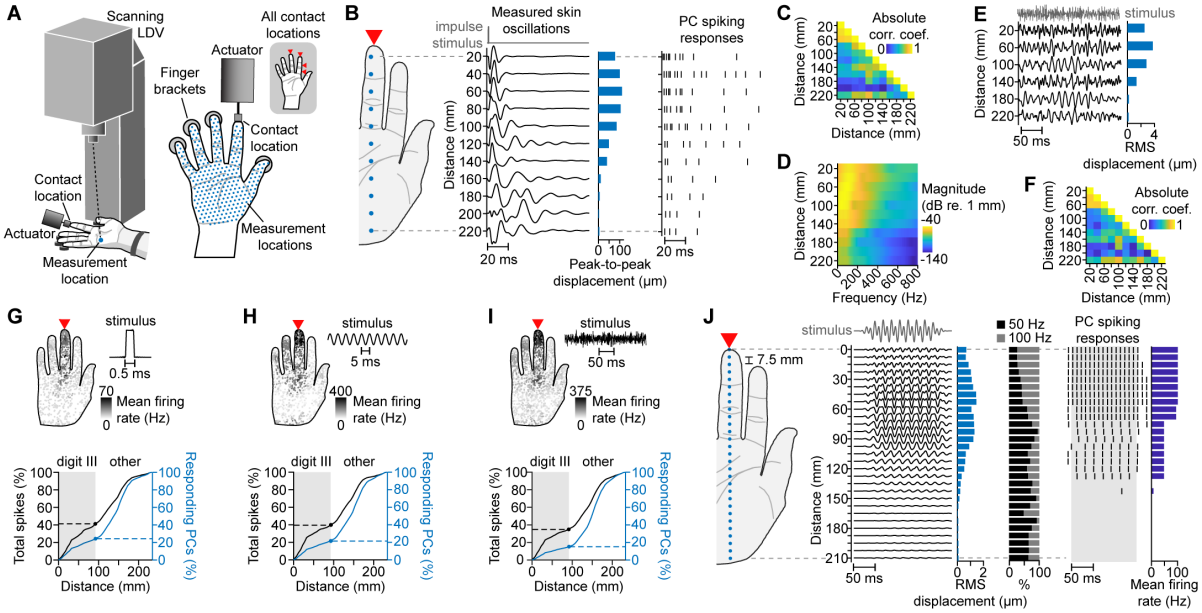

Figure 3.1: **Evoked skin oscillations drive location-specific spiking responses in PCs throughout the hand.** (**A**) Scanning laser Doppler vibrometer (LDV) measurement setup. (**B**) Left: vibrometry measurements of skin oscillations at selected locations (blue dots) elicited by an impulse (0.5 ms pulse width) applied at the digit III distal phalanx (DP) (red arrow). Right: PC spiking responses evoked by respective skin oscillations, shown for PC neuron model type 4. (**C**) Absolute Pearson correlation coefficients between skin oscillations shown in (B). (**D**) Magnitude spectra of skin oscillations shown in (B). (**E**) Reconstructed skin oscillations elicited by a bandpass-filtered noise stimulus (top trace, 50 to 800 Hz band) applied at the digit III DP. (**F**) Absolute Pearson correlation coefficients between skin oscillations at different distances from the contact location shown in (E). (**G**) Upper panel: PC mean firing rates elicited by an impulse applied at the digit III DP (red arrow; 15 µm max. peak-to-peak displacement across hand). Lower panel: cumulative percent of spikes (black) and responding PCs (blue) located within increasing distances from the contact location. Shaded region: results within digit III. (**H**) As in (G), for a 200 Hz sinusoidal stimulus (15 µm max. peak-to-peak displacement across hand). (**I**) As in (G), for a bandpass-filtered noise stimulus (50 to 800 Hz band, 5 µm max. RMS displacement across hand). (**J**) PC spiking responses (right, PC neuron model type 4) evoked by skin oscillations (middle) at selected locations (left, blue dots) elicited by a diharmonic stimulus ($f_1 = 50$ Hz, $f_2 = 100$ Hz) applied at the digit III DP (red arrow). Light blue bars: RMS displacements of skin oscillations; black and gray bars: percent of skin oscillation frequency magnitude spectrum composed of 50 Hz (black) or 100 Hz (gray) components; dark blue bars: PC firing rates calculated from spikes within shaded region. All plots show data from Participant 5 (P5).

All stimuli evoked spiking activity in PCs throughout the hand, consistent with predictions from theory and findings from prior studies [12, 13, 14]. The majority of the elicited spiking activity and responding PCs were in hand regions far removed from the contact location. This was true for all stimulus types, including brief impulses (Fig. 3.1G), sinusoids (Fig. 3.1H and Fig. 3.6C), and bandpass-filtered noise stimuli (Fig. 3.1I) and Fig. 3.6E). In each case, the patterns of evoked spiking activity reflected the effects of biomechanical filtering (Fig. 3.6B, D). For example, a brief impulse evoked PC spiking responses that varied based on hand location and exhibited sustained firing for more than 20 ms, reflecting the dispersive effects of biomechanical transmission (Fig. 3.1B).

PC responses also exhibited characteristic entrainment behavior (phase-locking to the oscillations of periodic stimuli) that was modified by biomechanical filtering. For example, a diharmonic stimulus applied at the fingertip evoked distance-dependent patterns of entrainment (Fig. 3.1J). Receptors near the contact location (< 60 mm) entrained to the higher frequency signal component (100 Hz), while more distant receptors entrained to the lower frequency component (50 Hz). This distance-dependent entrainment behavior arose due to the greater attenuation of higher frequency skin oscillations with distance (Fig. 3.1J, black and gray bars), an effect of tissue viscoelasticity [4, 48]. Thus, PC spiking activity is altered by effects of biomechanical filtering that vary with the location of the receptor in the hand.

3.4 Spatial Dependence of Biomechanical Filtering

To more fully characterize the spatial dependence of biomechanical filtering, we analyzed the frequency-dependent transmission of skin oscillations across the hand. Applied sinusoidal stimuli (frequencies between 20 and 800 Hz) elicited widespread skin oscillations, with distance-dependent amplitudes that varied greatly with stimulus frequency

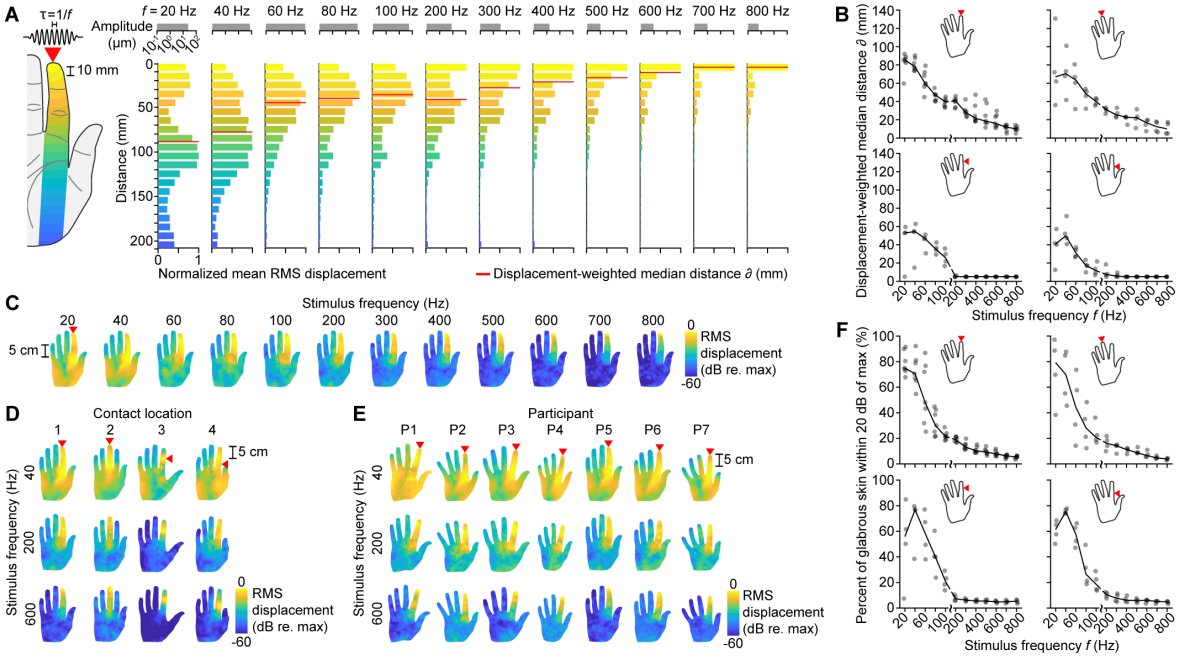

Figure 3.2: **Biomechanical filtering in the hand is frequency- and location-dependent.** (**A**) Normalized root mean square (RMS) skin displacements averaged within 10 mm-wide bands at increasing distances from the contact location elicited by sinusoidal stimuli of various frequencies (20 to 800 Hz). Amplitude scale bars (top, gray) show maximum peak-to-peak displacement across the hand at each frequency. Red lines: median transmission distance; red arrow: contact location. Shown for P5. (**B**) Median transmission distance of RMS skin displacement distributions across frequency for all participants and contact locations. Red arrows: contact location; lines: median across participants; dots: data points for each participant. (**C**) RMS displacement across the hand elicited by sinusoidal stimuli of various frequencies (20 to 800 Hz). Red arrow: contact location. Shown for P5. (**D**) As in (C), for other contact locations. Shown for P5. (**E**) As in (C), for P1 to P7. (**F**) Percent of glabrous skin where RMS skin displacement is within 20 dB of the maximum RMS displacement, for all participants and contact locations. Plots can be read as in (B).

(Fig. 3.2A); results for other participants and contact locations: see Fig. 3.7). At low frequencies ($\leq 100\,\text{Hz}$), the median transmission distance extended well beyond the stimulated digit, and the amplitude decay was non-monotonic with distance from the contact location. In contrast, higher-frequency components were concentrated within the stimulated digit and exhibited relatively monotonic decay with distance. We obtained similar findings for all participants and contact locations (Fig. 3.2B). These complex, frequency-dependent patterns of biomechanical filtering are a function of soft tissue viscoelasticity and the heterogeneous morphology of the hand.

We further observed the influence of the hand's morphology and skeletal structure in the spatial patterns of biomechanical filtering across the whole hand (Fig. 3.2C-E; results for all participants and contact locations: see Fig. 3.8). At low frequencies ($\leq 100\,\text{Hz}$), transmission was notably enhanced near the metacarpophalangeal (MCP) joint of the stimulated digit and in the lateral and contralateral extensions of the palmar surface (thenar and hypothenar eminences). These whole-hand patterns of biomechanical filtering also demonstrated that low-frequency stimuli evoked prominent oscillations (amplitudes within 20 dB of maximum) over a substantial fraction of the hand surface (mean 50 %; Fig. 3.2F). In contrast, higher frequencies evoked skin oscillations that were confined to a smaller proportion of the hand surface (mean 8 %). These findings were consistent across contact locations and participants.

3.5 Biomechanical Filtering Modulates PC Tuning

We next examined how biomechanical filtering modulates the tuning characteristics of PCs, as reflected in their frequency-dependent entrainment behavior (Fig. 3.1J). To do this, we analyzed whole-hand PC spiking activity evoked by sinusoidal stimuli of various frequencies (20 to 800 Hz). We characterized the frequency-dependent sensitivity of PCs

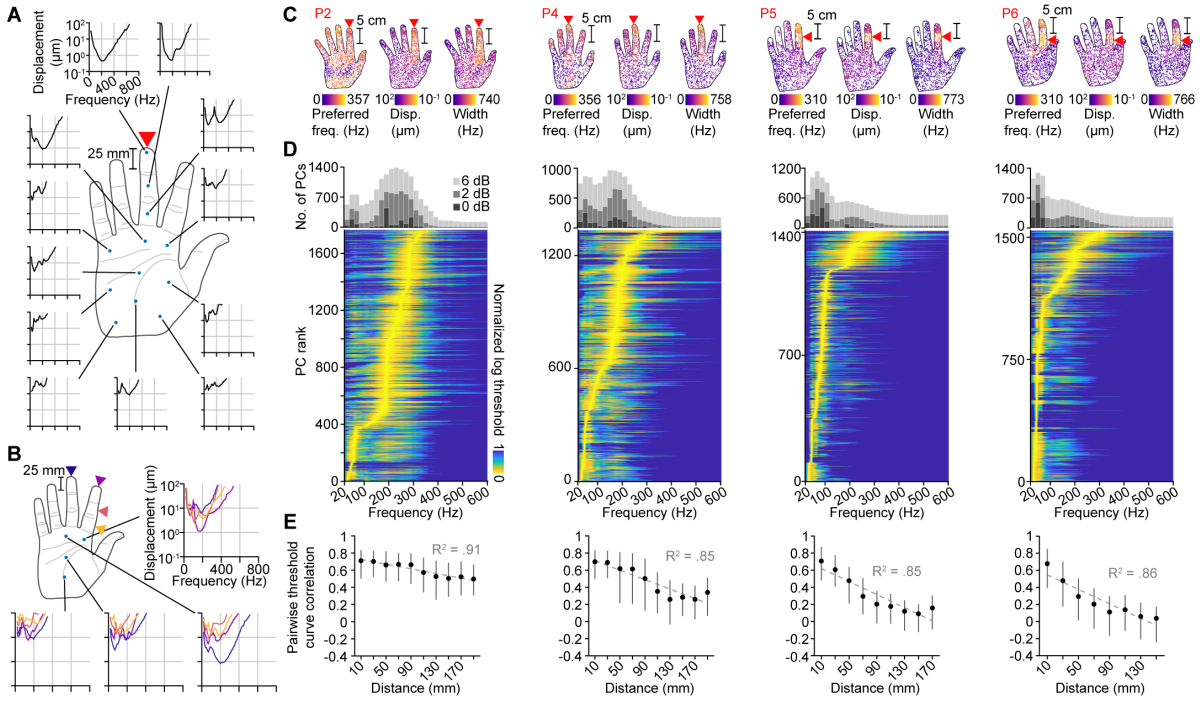

Figure 3.3: **Biomechanical filtering diversifies PC response characteristics.** (**A**) Entrainment threshold curves of PCs at selected locations (blue dots). Red arrow: Contact location. Shown for PC neuron model type 4 and P1. (**B**) Entrainment threshold curves of PCs at selected locations (blue dots) for each of four contact locations (colored arrows). Line colors correspond to contact locations. Shown for PC neuron model type 4 and P1. (**C**) Preferred frequency (left), minimum curve value (middle), and curve width (right) for each PC in the hand. Red arrow: contact location; red text: participant number. (**D**) Lower panel: Entrainment threshold curves for all PCs in the hand rank ordered by preferred frequency. Upper panel: Number of PCs at each frequency with entrainment threshold curve values within 0 dB (light gray), +2 dB (medium gray), and +6 dB (dark gray) of the curve minimum. Participants and contact locations as in (C). (**E**) Pearson correlation coefficients between all pairs of entrainment threshold curves of PCs located within 10 mm of the contact location and those of PCs located within 20 mm-wide bands at increasing distances from the contact location. Center distance for each band shown. Dots: median; error bars: IQR; gray dotted lines: linear fit of medians; gray text: R^2 value for linear fit. Participants and contact locations as in (C).

by computing entrainment threshold curves, which represent the minimum displacement required to evoke entrainment at each frequency (see Methods). PCs located near the contact location exhibited U-shaped entrainment threshold curves with preferred (most sensitive) frequencies between 200 and 300 Hz (Fig. 3.3A and Fig. 3.9A). This result is consistent with established descriptions of PC function, which are based on *in vivo* experiments where the stimulus is applied adjacent to the PC [90, 93, 97, 99, 100]. However, we obtained diverging findings for the larger number of PCs located outside the contact region. Entrainment threshold curves for remote PCs varied greatly and exhibited multiple prominent minima, reflecting location-specific effects of biomechanical filtering (Fig. 3.3A and Fig. 3.9B, C). Moreover, PC entrainment threshold curves varied as the contact location varied (Fig. 3.3B).

We further analyzed the distribution of frequency tuning across whole-hand PC populations by rank ordering all entrainment threshold curves by preferred frequency (Fig. 3.3C, D; results for all participants and contact locations: see Fig. 3.10). Within each population, PCs exhibited diverse preferred frequencies, ranging from 25 to 420 Hz (Fig. 3.11A-D). The preferred frequencies of PCs located near the contact location were consistent with values obtained in prior studies (200 to 300 Hz), as noted above. However, PCs located outside the contact region exhibited a wider range of frequency sensitivities (Fig. 3.11E-H). Strikingly, across all participants and contact locations, a substantial proportion of PCs in a population preferred frequencies below 100 Hz (mean 47 %). In addition, PCs at greater distances from the contact location exhibited more narrowly tuned curves and higher thresholds, indicating greater specificity in frequency preference and lower sensitivity (Fig. 3.3C).

However, the entrainment threshold curves exhibited complex shapes that varied greatly with hand location in a manner not adequately summarized by preferred frequency, curve width, or minimum threshold. To characterize distance-dependent varia-

tions in the threshold curves, we instead calculated pairwise correlations between threshold curves of PCs at the contact location and those within regions at progressively greater distances from the contact location (Fig. 3.3E; results for all participants and contact locations: Fig. 3.12). For all participants and contact locations, the median pairwise correlation between threshold curves decreased with increasing distance from the contact location (0.027 to 0.095 per 20 mm; $R^2 = 0.71$ to 0.91). Together, these findings demonstrate that pre-neuronal biomechanical filtering diversifies frequency response characteristics in whole-hand PC populations.

3.6 Biomechanical Filtering Diversifies Tactile Encoding

We next asked whether this diversification enhanced information encoding in PC population spiking responses, particularly for the large proportion of PCs outside the contact region. To address this, we characterized the dimensionality and information content of PC population spiking activity as a function of distance from the contact location. Informed by prior research [98, 112], we employed a diverse set of stimuli containing sinusoidal, diharmonic, and bandpass-filtered noise signals with various frequency and amplitude parameters (Table 3.1, Table 3.2, Table 3.3). We used principal component analysis to assess the latent dimensionality of PC firing rates in subpopulations of PCs within increasing maximum distances from the contact location. For all participants and contact locations, dimensionality, calculated as the number of principal components needed to capture 99 % of the variance in the firing rates, increased with distance. The dimensionality was 2 to 5 times higher at distances greater than 100 mm from the contact location than at distances less than 20 mm (Fig. 3.4A). Thus, PCs at increasing

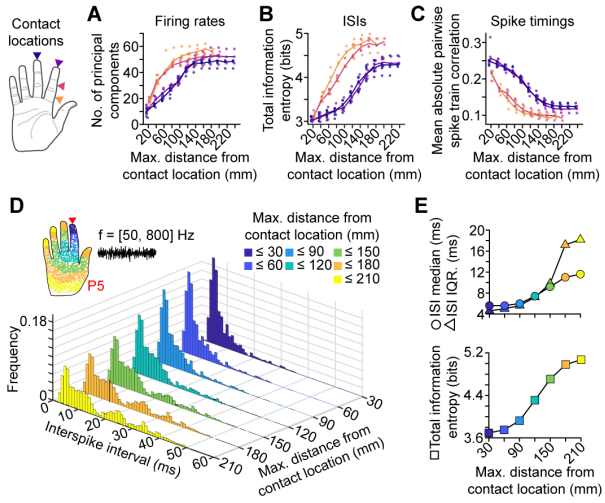

Figure 3.4: **Biomechanical filtering diversifies PC spiking activity.** ((**A**) Number of principal components explaining 99 % of the variance in the firing rates of PCs within increasing distance ranges from the contact location. Colors indicate contact location; dots: data points for each participant; lines: median across participants. Analyses are conducted on PC spiking activity evoked by a diverse stimulus set. (**B**) Total information entropy of interspike interval (ISI) distributions (1 ms bin width) constructed from the spiking activity of PCs within increasing distance ranges from the contact location. Plot can be read as in (A). (**C**) Mean absolute spike train correlation between all pairs of PCs both located within increasing distances from the contact location. Spike trains were binned with a bin width of 1 ms. Plot can be read as in (A). (**D**) ISI histograms constructed from the spiking activity of PCs located within increasing distances from the contact location (hand inset) in response to a bandpass-filtered noise stimulus (50 to 800 Hz band, 5 µm max. RMS displacement across hand, 175 ms duration) applied at the digit II DP of P5. (**E**) Median (circles), interquartile range (triangles), and total information entropy (squares) of the ISI histograms in (D).

distances from the contact location captured progressively more variance, highlighting the facilitative role of biomechanical filtering in PC population encoding.

In addition to firing rates, PCs signal information about touch events via spike timing [112]. We characterized information encoded in PC spike timing by computing the Shannon information entropy of interspike interval (ISI) histograms constructed from the spiking activity of PC subpopulations within increasing maximum distances from the contact location. For all stimuli, ISIs were generally larger and more broadly distributed with increasing distance (Fig. 3.4D, E and Fig. 3.13). Consequently, information encoded in the ISIs increased monotonically with distance by a factor of more than 1.4 before plateauing at 140 to 180 mm from the contact location (Fig. 3.4B). The findings were robust to variations in ISI histogram bin widths (Fig. 3.14A-G).

We also analyzed the correlations between spiking responses evoked in subpopulations of PCs within increasing maximum distances from the contact location. Consistent with the ISI findings, as distance increased, the spiking responses of remote PCs became progressively less correlated with the spiking responses of PCs near the contact location, as quantified by mean pairwise spike train correlations (Fig. 3.4C and Fig. 3.14H-N). Together, these information encoding measures demonstrate that biomechanical filtering diversifies PC spiking activity by enabling remote PCs to encode information not captured by PCs near the contact location, thereby supporting tactile encoding efficiency [107, 108]. The plateaus in the computed measures also indicate that some response redundancy is preserved within the population responses.

3.7 Discussion

Our study combined high-resolution vibrometry measurements of whole-hand biomechanical transmission with neural simulations leveraging extensively validated neuron

models [67]. The results shed light on the pre-neuronal role of biomechanical filtering in modulating and diversifying PC population spiking activity. These findings indicate that previously documented response characteristics of isolated PCs, including entrainment threshold curves, do not accurately capture the behavior of most PCs within the human hand. Because the majority of PCs that respond during touch events are distant from the contact location, neural activity in remote PCs represents a dominant proportion of the total population response and can thus be expected to affect downstream tactile processing and, ultimately, perception.

The perceptual significance of widespread PC responses is well established by studies that reveal prominent vibrotactile summation and masking effects arising between stimuli applied at distant hand locations [229, 230]. There is also ample evidence that biomechanically facilitated activity in remote PCs influences perception. Prior experiments have demonstrated that in subjects with impaired tactile sensation due to anesthesia, nerve compression, or traumatic injury, tactile perception in both the high-frequency ($> 80\,\mathrm{Hz}$) and flutter range ($\sim 20\,\mathrm{Hz}$) can be mediated by remote PCs [18, 233, 234]. Prior research also shows that fine surface textures explored with the anesthetized finger can be perceptually discriminated [17]. These discriminative abilities were found to be facilitated by spiking activity in remote PCs evoked by skin oscillations transmitted far from the contact location [12].

Prior studies have also demonstrated the significance of biomechanical transmission for the perception of artificial haptic feedback. For example, the propensity of lower-frequency skin oscillations to travel greater distances has been exploited to realize frequency-controlled haptic effects that are perceived to expand or contract in spatial extent from a single localized site of stimulation [4]. Moreover, a recent study reported prominent effects of biomechanical transmission on the perception of tactile motion stimuli supplied via airborne ultrasound [56].

Accounting for the effects of biomechanics on peripheral tactile encoding may also shed light on touch perception in other settings. For example, perceived vibrotactile intensity is highly frequency-dependent [235, 236], but the observed dependence conflicts with predictions derived based on responses of PCs adjacent to the contact location [98]. Moreover, our understanding of the perception of polyharmonic stimuli is incomplete. A proposed model for the perception of stimuli with complex frequency spectra invoked the existence of mechanoreceptor subpopulations that vary in frequency tuning [120, 121]. However, this model has not gained traction because such subpopulations have not been previously observed. Indeed, established characterizations of PC function based on stimulation near the receptor location depict PC frequency sensitivity as highly stereotyped.

Our findings may also shed light on a number of peculiar aspects of PC innervation of the hand. Despite the stereotyped response properties of isolated PCs and their large receptive fields, which span most of the hand, PCs in the glabrous skin number in the hundreds or more [3, 81, 82, 103]. Together, these characteristics may be interpreted to imply tremendous response redundancy, which would be at odds with encoding efficiency hypotheses [107, 108]. However, our results demonstrate that biomechanical filtering diversifies PC response characteristics, thereby reducing PC population response redundancy and enhancing encoding efficiency. Furthermore, prominent clusters of PCs are observed near the MCP joints in human hands [3, 103]. Near those locations, we observed elevated oscillation amplitudes at low frequencies ($< 100\,\mathrm{Hz}$), suggesting that PCs may be preferentially located in regions of the hand where biomechanical transmission is facilitated.

The frequency-dependent patterns of biomechanical transmission and filtering we observed are generally consistent with prior characterizations of mechanical propagation near the contact location [4, 13, 37], taking into account likely differences in contact conditions. Here, we present whole-hand measurements at significantly greater spatiotempo-

ral resolution than was used in prior studies. This made it possible to resolve previously unobserved effects of biomechanical transmission and filtering throughout the hand, including the non-monotonic decay of oscillation amplitude with distance and the contact location-dependent variations in filtering.

Despite the observed complexity of biomechanical transmission in the hand, several characteristics were conserved across multiple hands and contact locations. These included the frequency-dependent variations in transmission amplitude with distance, the elevated transmission distances at low frequencies ($\leq 100\,\mathrm{Hz}$), and the enhancement of transmission near the MCP joints. These features demonstrate how biomechanical filtering generates spatial and spectral structure that the brain could learn and exploit, similar to hypotheses for efficient encoding of whole-hand touch events [2], object slippage [30], and tool use [27].

Overall, the pronounced effects of biomechanics that we observed in the PC system exemplify how pre-neuronal mechanisms can play a crucial role in sensory processing, which is supported by analogous findings in other sensory systems. For example, the effect of biomechanical filtering on tuning properties across PC populations in the hand is somewhat comparable to the frequency-place transform that is biomechanically affected by the mammalian cochlea [237, 238]. Moreover, the biomechanics of the human body filters the frequency content of motion inputs to the vestibular system during natural movement, which likely has consequences for underlying neural circuitry [156]. Similar conclusions about the impact of biomechanics in sensory processing have been drawn in studies of the rodent vibrissal system, where the mechanics of the whiskers are instrumental to tactile neural coding [162, 163].

3.8 Methods

3.8.1 *In Vivo* Optical Vibrometry

Mechanical oscillations across the volar hand surface were imaged with a scanning laser Doppler vibrometer (SLDV; model PSV-500, Polytec, Inc., Irvine, CA; sample frequency 20 kHz) fastened to a pneumatically isolated table. During each recording, the hand was fixed to the table in an open, palm-up posture via custom-fit 3D-printed supports that were fastened to the table and adhered to the fingernails of all but the stimulated digit (Fig. 3.1A). Participants (n = 7, 5 male) were 20 to 45 years of age (mean 27.4 years) and were recruited from the student and staff population at the authors' institution. The sample size was determined based on previously published research employing similar methodologies [13, 1, 2, 4]. Participants were seated in a reclined chair with the arm relaxed, supported by a foam armrest, and constrained with Velcro straps. All participants gave their informed, written consent prior to the data collection. The study was approved by the Human Subjects Committee of the University of California, Santa Barbara (Protocol Number 9-18-0676).

The SLDV imaged spatially and temporally resolved skin oscillations at sampling locations distributed on a uniform grid covering the entire volar hand surface (grid spacing 8 mm, 200 to 350 locations). The sampling grid exceeded the Nyquist criterion threshold for frequencies in the tactile range (0 to 1000 Hz), at which spatial wavelengths are between 20 to 100 mm [2]. Oscillations were imaged in the normal direction to the skin surface. Prior vibrometry measurements have demonstrated that most of the energy in evoked skin oscillations is concentrated in oscillations normal to the skin surface [4] and that stress in the normal direction is highly predictive of PC spiking responses [67].

All data were captured from the right hands of participants. Hand lengths ranged from 18 to 21.6 cm (mean 19.9 cm) as measured from the tip of digit III to the bottom

of the hand at the middle of the wrist. Each hand was positioned 36 cm below the SLDV aperture, which ensured that the measurements captured at least 95 % of the signal variance at all measurement locations. Each participant's hand shape and the 2D spatial coordinates of all measurement locations were captured via the integrated SLDV geometry processor and camera. Measurements were interpolated to obtain skin oscillations at other locations on the 2D hand surface (see Supplemental Methods).

Measured skin oscillations were evoked by mechanical impulses (rectangular pulse, duration 0.5 ms) applied at each of the four contact locations described below. Measurements were synchronized to the stimulus onset. Each measurement was obtained as the median of 10 captures and bandpass filtered to the vibrotactile frequency range (20 to 1000 Hz). Frequency analysis was performed by computing magnitude spectra, which were smoothed using a moving median window (width: 3 samples) to remove measurement artifacts. Numerical frequency-domain integration was employed to obtain skin displacement from velocity. Stimuli were delivered via an electrodynamic actuator (Type 4810, Brüel & Kjær) driven with a laboratory amplifier (PA-138, Labworks). The actuator terminated in a plastic probe (7×7 mm contact surface) that was adhesively attached to the skin at the stimulus contact location. The actuator and probe were configured to avoid obstructing the optical path used for the SLDV measurements.

Stimuli were applied at each of four different contact locations (CL) that were registered to standard anatomical positions on the hand: the distal phalanx (DP) of digit II along the axis of the finger (CL 1, n = 7 participants), the DP of digit III along the axis of the finger (CL 2, n = 4), the intermediate phalanx (IP) of digit II perpendicular to the axis of the finger (CL 3, n = 4), and the proximal phalanx (PP) of digit II perpendicular to the axis of the finger (CL 4, n = 4) (Fig. 3.1A). These measurements took approximately 10 minutes per contact condition per participant. Measurements for CL 2, 3, and 4 were captured from a subset of participants from which measurements for CL

1 were captured (P1, P4, P5, and P6).

3.8.2 Computing Skin Oscillations Evoked by Arbitrary Stimuli

Theory and experimental findings [21, 54] indicate that biomechanical transmission in the hand is linear for the stimulus magnitudes employed here. Consequently, the transmission of evoked skin oscillations may be mathematically described by a wave equation of the form $L\,u(\mathbf{x},t) = 0$, where L is a linear partial differential operator encoding wave transport, $\mathbf{x}$ is a skin location, t is time, and $u(\mathbf{x},t)$ is the evoked skin oscillation pattern. From linear systems theory, an arbitrary force stimulus $F(t)$ applied to the skin at location $\mathbf{x}_0$ evokes oscillations $u(\mathbf{x},t)$ given by

$$u(\mathbf{x},t) = g_{\mathbf{x}_0}(\mathbf{x},t) * F(t), \tag{3.1}$$

where $*$ denotes convolution in time and $g_{\mathbf{x}_0}(\mathbf{x},t)$ is the Green's function encoding the excitation of skin oscillations evoked by a unit Dirac impulse applied at $\mathbf{x}_0$. We empirically determined the Green's functions for each hand and contact location $\mathbf{x}_0$ using the impulse-driven skin oscillation measurements described above. The skin oscillations evoked by arbitrary stimuli $F(t)$ were numerically computed using Equation 3.1.

To confirm the accuracy of this method, we compared the numerically computed oscillations with measured oscillations evoked by sinusoidal stimuli $F(t)$ with frequencies ranging from 20 to 640 Hz. The measurement procedure was identical to the one described above, apart from the input waveform. Consistent with linear systems theory, we found that the numerically computed oscillations closely approximated the actual measurements at all frequencies (Fig. 3.5). Because the numerical methodology avoids the need for time-intensive experiments, we used it to determine skin oscillations evoked by arbitrary stimuli in the remainder of the experiments.

Stimuli

We analyzed skin oscillations $u(\mathbf{x}, t)$ evoked by sinusoidal, diharmonic, and bandpass-filtered noise stimulus waveforms $F(t)$. For sinusoidal stimuli, $F(t) = F_0 \sin(2\pi f t)$, where f is frequency and F_0 is force amplitude. Force amplitudes were approximately 0.25 N, except as noted. For diharmonic stimuli, $F(t) = F_1 \sin(2\pi f_1 t) + F_2 \sin(2\pi f_2 t)$, with independent force amplitudes F_1 and F_2. F_1 and F_2 were selected to ensure that the maximum evoked peak-to-peak skin displacements D_{pp} were equal, where

$$D_{pp} = \max_{\mathbf{x}} \left\{ \max_{t} \{u(\mathbf{x}, t)\} - \min_{t} \{u(\mathbf{x}, t)\} \right\}. \tag{3.2}$$

Bandpass-filtered noise stimuli were synthesized using a spectral Gaussian white noise algorithm [239], then bandpass filtered to the desired frequency range. Each bandpass-filtered noise stimulus was generated from the same Gaussian white noise trace, then scaled by a force amplitude F_0.

3.8.3 Whole-Hand Neural Simulations

PC population spiking responses were obtained *in silico* by using the skin oscillations to drive a population of spiking neuron models extracted from a simulation package (Touchsim [67], Python) (3.6A), similar to the methodology applied in prior work investigating PC population responses during whole-hand touch events [16]. The PC neuron models consisted of four PC types, each trained and validated in a prior study on electrophysiology recordings from non-human primates [98]. Each PC neuron model type varies slightly in its response properties (3.9A). The PC neuron models supply a nonlinear mapping from skin displacement to spiking output and accurately reproduce experimentally identified PC response characteristics, including response thresholds that

vary across several orders of magnitude over the vibrotactile frequency range [90, 100] and frequency-dependent thresholds of entrainment [93, 97, 99]. The stimulus amplitudes used in this work fell within the range over which the PC models were validated.

Whole-hand PC populations were assembled by sampling a random distribution weighted by spatial densities σ reported in prior studies [81, 82]: $\sigma = 25\,\mathrm{cm}^2$ in the distal phalanges and $\sigma = 10\,\mathrm{cm}^2$ in the rest of the hand. Except where otherwise noted, the PC neuron model type for each PC in a population was randomly selected to be one of the four PC neuron model types noted above. Each PC was driven by the time-varying skin oscillations $u(\mathbf{x}_m, t)$, where $\mathbf{x}_m$ is the PC location. This produced a spike train represented as an ordered sequence $Y_m = \{t_1, t_2, ..., t_Q\}$, where t_i are spike times and Q is the number of stimulus-evoked spikes.

3.8.4 PC Entrainment Threshold Curves

Entrainment threshold curves were constructed to characterize PC frequency sensitivity. At each frequency (20 to 800 Hz), the force amplitude of the sinusoidal input stimulus was varied to determine the entrainment threshold for each PC in the whole-hand population. The entrainment threshold was identified as the minimum input force amplitude at which one spike was elicited per cycle of the sinusoidal stimulus. For each mth PC and frequency f, the threshold curve $E_m(f)$ recorded the maximum peak-to-peak displacement of skin oscillations evoked across the hand (D_{pp}, Eq. 3.2) at the identified entrainment force amplitude. The maximum D_{pp} across all conditions was 100 µm. In prior literature, threshold curves were determined by placing the stimulating probe near the hotspot of the terminating neuron [90, 93, 97, 99, 100] (Fig. 3.9A). Here, however, we analyzed threshold curves for all PCs across the hand with the stimulus contact location held constant. This preserved the effects of biomechanical transmission and filtering

that were not captured in prior approaches. For each PC, the preferred (most sensitive) frequency was computed as $f^* = \arg\min_f\{E_m(f)\}$. The width of each threshold curve was determined as the full width of the threshold curve (not necessarily contiguous) at half-minimum and characterized the sensitivity bandwidth of the respective PC.

Correlation Analysis

The pairwise similarity of entrainment threshold curves for different PCs was assessed using the Pearson correlation coefficient c_{ij}, where i and j index the threshold curves of PCs in a population. We conducted this analysis by separating whole-hand PC populations into PC subpopulations P_k located within different distance ranges from the stimulus contact location, where $k = 0, 1, \ldots, K$ indexes the distance range. P_0 contained all N_0 PCs located within 10 mm of the contact location. For $k > 0$, P_k contained all N_k PCs located at distances d_k from the contact location satisfying $(20(k-1)+10) \leq d_k < (20k+10)$ mm. Distances on the 2D hand surface were computed from the SLDV geometry data using Djikstra's algorithm. We computed the mean pairwise correlation σ_k between all PC threshold curves in P_0 and all PC threshold curves in P_k as

$$\sigma_k = \frac{1}{N_0 N_k} \sum_{i=1}^{N_0} \sum_{j=1}^{N_k} c_{ij}. \tag{3.3}$$

We computed the mean pairwise correlation σ_0 between PC threshold curves in P_0 as

$$\sigma_0 = \frac{2}{N_0(N_0-1)} \sum_{i=1}^{N_0} \sum_{j=i+1}^{N_0} c_{ij}. \tag{3.4}$$

3.8.5 PC Population Spiking Activity Analysis

Efficient encoding hypotheses posit that neural sensory circuitry should minimize redundancy [107, 108]. We assessed encoding efficiency by analyzing mean firing rates and

spike timing, both of which are salient to tactile encoding [115, 240, 241]. To this end, we assembled a diverse set of stimuli encompassing commonly occurring tactile signals based on prior studies [98, 112]. The stimulus set contained 60 sinusoidal, 117 diharmonic, and 50 bandpass-filtered noise stimuli that varied in amplitude and frequency parameters (see Supplementary Methods, and Table 3.1, Table 3.2, Table 3.3). We obtained spike trains evoked in whole-hand PC populations for each stimulus ($N = 227$), contact location ($N = 4$), and participant ($N = 4$ or $N = 7$ depending on the contact location).

To assess the redundancy in spiking responses of remotely located PCs, we constructed PC subpopulations P^r located within increasing distances $d_r = 20r$ mm from the contact location. The subpopulations formed a nested array of sets, $P^1 \subset P^2 \subset \cdots \subset P^R$, successively encompassing larger numbers of PCs, N^r, where $N^r = N^{r-1} + \Delta N^r$. We analyzed spiking responses from each subpopulation using principal component analysis (PCA), interspike interval (ISI) information entropy, and spike train correlations.

Firing Rate Latent Dimensionality Analysis

To assess the latent dimensionality of spiking activity from each subpopulation r, principal component analysis (PCA) was performed on the matrix of time-averaged firing rates M^r_{mn}, where m indexed PCs and n indexed the stimuli. The data matrix M^r_{mn} was standardized across stimuli (zero-mean and unit standard deviation). To assess the latent dimensionality of the subpopulation firing rates, we computed the minimum number $B(r)$ of principal components that captured at least 99 % of the variance. A higher value of $B(r)$ indicated greater firing rate heterogeneity in subpopulation r.

Interspike Interval Information Entropy Analysis

We computed interspike intervals (ISIs) from spike trains $\mathbf{s}^n_m$ evoked in each PC m by each stimulus n. From these data, we computed normalized ISI histograms for each PC

subpopulation P^r. In the main results (Fig. 3.4B), the histogram bin size was $\Delta t = 1\,\text{ms}$ because PCs encode touch information with millisecond precision [112]. We obtained similar results for values of Δt between 0.5 and 2 ms (Fig. 3.14A-G). Let p_q^r be the probability of an ISI t from P^r falling in the range $t_q \leq t < t_{q+1}$, where $t_q = q\,\Delta t$. We assessed information in spike timing by computing the Shannon information (entropy) $H(r)$, given by

$$H(r) = -\sum_{q=1}^{Q} p_q^r \log_2(p_q^r). \tag{3.5}$$

We also applied the same analysis to individual stimuli (Fig. 3.4D) and Fig. 3.13). Higher ISI entropy values $H(r)$ indicated more information and less redundancy in spike timing activity.

Spike Train Correlation Analysis

We computed spike train correlations [242, 243, 244] using binned spike train vectors with bin width $\Delta t = 1\,\text{ms}$ (Python package elephant [245]) (Fig. 3.4C). We obtained similar results for values of Δt between 0.5 and 2 ms (Fig. 3.14H-N). For each stimulus n and PC subpopulation P^r, we assessed pairwise spike train correlations by computing Pearson correlation coefficients $c_{ij}^n(r)$ between each pair of binned spike trains $\mathbf{s}_i^n$ and $\mathbf{s}_j^n$, where i and j index PCs in P^r. We computed the mean spike train correlation $c(r)$ for each subpopulation P^r using

$$c(r) = \frac{2}{M(M-1)N} \sum_{n=1}^{N} \sum_{i=1}^{M} \sum_{j=i+1}^{M} |c_{ij}^n(r)|, \tag{3.6}$$

where M is the number of PCs in a subpopulation P^r and N is the number of stimuli. Lower spike train correlations indicated less redundancy within population spike timing activity. In contrast to the ISI entropy analysis, spike train correlations took into account

the relative differences in spike times between different PCs.

3.9 Supplementary Methods

3.9.1 Skin Oscillation Interpolation Across Hand Surface

Green's functions were measured at discrete locations $\mathbf{x}_k$ in 2D pixel space and mapped to real space using participants' hand lengths. The sampling grid exceeded the Nyquist criterion threshold for frequencies in the tactile range (0 to 1000 Hz), which exhibit spatial wavelengths between 20 to 100 mm [2]. This enabled us to determine Green's functions and skin oscillations at arbitrary locations $\mathbf{x}$ via interpolation. Data was first extrapolated to the boundary of the 2D hand surface outside the convex hull bounded by the measurement locations using distance weighting. The skin displacements at boundary locations $\mathbf{x}_b$ were computed as

$$u(\mathbf{x_b}, t) = \frac{\sum_{k=1}^{N} \phi(\mathbf{x}_b, \mathbf{x}_k) u(\mathbf{x}_k, t)}{\sum_{k=1}^{N} \phi(\mathbf{x}_b, \mathbf{x}_k)},$$
$$\text{where } \phi(\mathbf{a}, \mathbf{b}) = \begin{cases} 1 - \frac{d(\mathbf{a},\mathbf{b})}{\alpha} & d(\mathbf{a}, \mathbf{b}) \leq \alpha \\ 0 & d(\mathbf{a}, \mathbf{b}) > \alpha \end{cases}, \tag{3.7}$$

where $d(\mathbf{a}, \mathbf{b})$ was the Euclidean distance between locations $\mathbf{a}$ and $\mathbf{b}$ in pixel space and N was the total number of measured locations. We selected $\alpha = 90$ pixels to ensure at least two measured locations contributed to the extrapolation of the displacement at boundary locations. The extrapolated displacements $u(\mathbf{x}_b, t)$ and the sampled measurements $u(\mathbf{x}_k, t)$ were used to compute displacements at arbitrary locations $u(\mathbf{x}, t)$ inside the 2D hand surface using nearest neighbor interpolation.

3.9.2 Stimulus Set for PC Population Spiking Activity Analysis

The stimulus set consisted of 60 sinusoidal, 117 diharmonic, and 50 bandpass-filtered noise stimuli presented at various amplitudes. The sinusoidal stimuli were 100 ms in duration and comprised 12 frequencies and 5 amplitudes per frequency (stimulus parameters: see Table 3.1). The diharmonic stimuli were 100 ms in duration and comprised 13 frequency pairs and 9 amplitude combinations per pair (Table 3.2). The bandpass-filtered noise stimuli were 1000 ms in duration and comprised 10 frequency bands and 5 amplitudes per band (Table 3.3).

For the sinusoidal stimuli, the force amplitudes of the stimuli were selected to yield skin oscillations with a specific maximum peak-to-peak displacement across all hand locations (D_{pp}, Eq. 3.2). For the diharmonic stimuli, force amplitudes were selected independently for each sinusoidal component to yield specified values of D^1_{pp} and D^2_{pp}, the maximum peak-to-peak displacement across all hand locations for each sinusoidal component separately (see Methods). For the bandpass-filtered noise stimuli, we instead determined the force amplitude by specifying D_{RMS}, the maximum RMS displacement of skin oscillations across all hand locations. The maximum peak-to-peak displacement across the whole hand evoked by any stimulus in the stimulus set was 200 µm.

For the sinusoidal and diharmonic stimuli, the minimum D_{pp} for a given frequency component was the smallest displacement that elicited entrainment in one of the four PC models via direct stimulation (i.e., without the effects of biomechanical filtering). The exception was 800 Hz for which D_{pp} =10 µm, which was below the entrainment threshold at that frequency. The maximum D_{pp} for each frequency component was either 100 µm or the D_{pp} which yielded a maximum peak-to-peak skin acceleration of $50 \times \mathrm{g} = 490\,\mathrm{m/s^2}$, whichever was smaller. This ensured that displacements remained in a regime where the skin could be considered approximately linear and in which the PC

models were validated. For sinusoidal stimuli, the 5 amplitudes were equally spaced in log space between the identified minimum and maximum D_{pp}. For diharmonic stimuli, 3 amplitudes were selected for each frequency component and equally spaced in log space between the identified minimum and maximum D_{pp}. Stimuli were then presented for each combination of amplitudes ($3 \times 3 = 9$ amplitude combinations per frequency pair). For each bandpass-filtered noise stimulus, the selected D_{RMS} were 0.5, 1, 5, 10, and 20 µm.

3.10 Supplementary Tables

Frequency (Hz)	D_{pp} amplitudes (µm)
50	2.3, 5.9, 15.2, 38.9, 100
75	1.6, 4.5, 12.7, 35.6, 100
100	1.1, 3.4, 10.5, 32.4, 100
150	0.5, 1.9, 7.1, 26.6, 100
200	0.3, 1.4, 5.8, 24.2, 100
250	0.4, 1.4, 5.9, 24.3, 100
300	0.6, 2.2, 7.8, 28.2, 100
400	2.1, 5.2, 13, 32.2, 80
500	2.8, 5.8, 11.8, 24.3, 50
600	7.3, 10.8, 16, 23.7, 35
700	21, 21.9, 23, 24, 25
800	10, 11.9, 14.1, 16.8, 20

Table 3.1: Sinusoidal stimulus set parameters for PC population spiking activity analysis.

Frequencies (Hz)	D^1_{pp} amplitudes (µm)	D^2_{pp} amplitudes (µm)
50/100	2.3, 15.2, 100	1.1, 10.5, 100
50/150	2.3, 15.2, 100	0.5, 7.1, 100
50/250	2.3, 15.2, 100	0.4, 5.9, 100
50/500	2.3, 15.2, 100	2.8, 11.8, 50
50/800	2.3, 15.2, 100	10, 14.1, 20
100/200	1.1, 10.5, 100	0.3, 5.8, 100
100/300	1.1, 10.5, 100	0.6, 7.8, 100
100/500	1.1, 10.5, 100	2.8, 11.8, 50
100/800	1.1, 10.5, 100	10, 14.1, 20
200/400	0.3, 5.8, 100	2.1, 13, 80
200/600	0.3, 5.8, 100	7.3, 16, 35
200/800	0.3, 5.8, 100	10, 14.1, 20
400/800	2.1, 13, 80	10, 14.1, 20

Table 3.2: Diharmonic stimulus set parameters for PC population spiking activity analysis.

Frequency band (Hz)	D_{RMS} amplitudes (µm)
50 to 100	0.5, 1, 5, 10, 25
50 to 250	0.5, 1, 5, 10, 25
50 to 500	0.5, 1, 5, 10, 25
50 to 800	0.5, 1, 5, 10, 25
100 to 250	0.5, 1, 5, 10, 25
100 to 500	0.5, 1, 5, 10, 25
100 to 800	0.5, 1, 5, 10, 25
250 to 500	0.5, 1, 5, 10, 25
250 to 800	0.5, 1, 5, 10, 25
400 to 800	0.5, 1, 5, 10, 25

Table 3.3: Bandpass-filtered noise stimulus set parameters for PC population spiking activity analysis.

3.11 Supplementary Figures

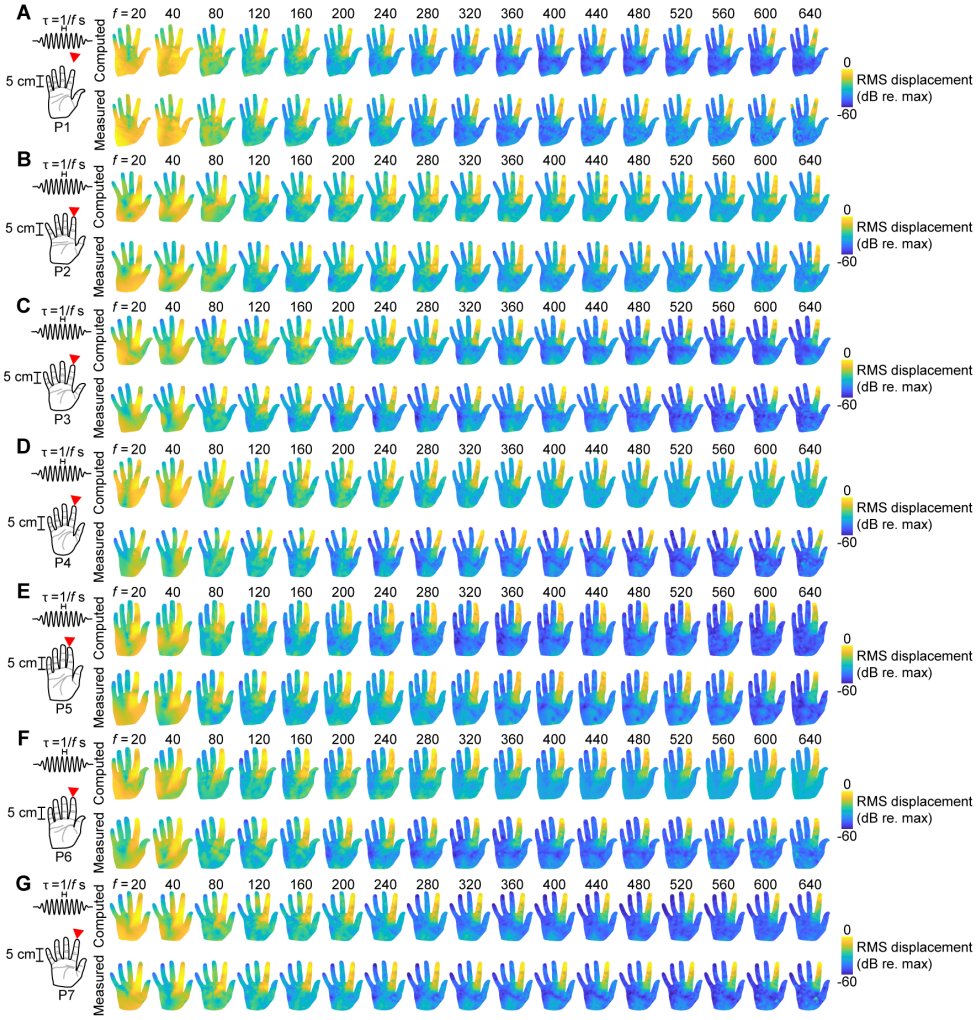

Figure 3.5: **Numerically determined versus measured whole-hand RMS skin displacements across frequency.** (**A**) Normalized root mean square (RMS) whole–hand skin displacements (log scale) elicited by windowed sinusoidal stimuli of various frequencies (20 to 640 Hz) applied at the digit II distal phalanx (DP) of Participant 1 (P1). Top row: numerically determined skin oscillations (Materials and Methods). Bottom row: experimentally measured skin oscillations. (**B**) As in (A) for P2. (**C**) As in (A) for P3. (**D**) As in (A) for P4. (**E**) As in (A) for P5. (**F**) As in (A) for P6. (**G**) As in (A) for P7.

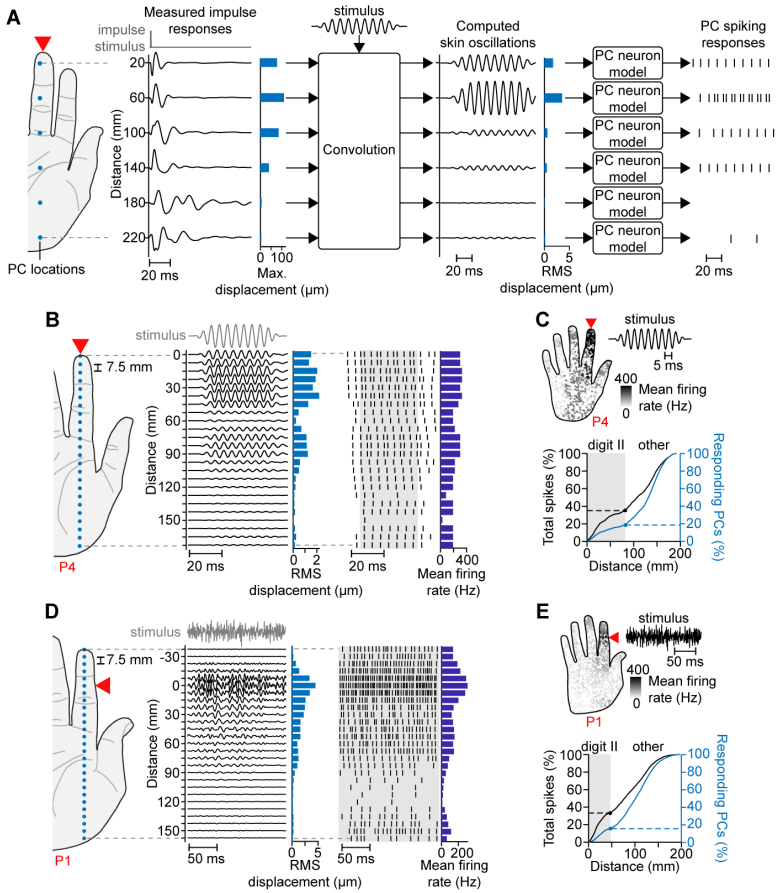

Figure 3.6: **Measurement-driven neural simulation methodology.** (**A**) Skin oscillations are computed at PC locations (blue dots) in response to an arbitrary stimulus via convolution with measured impulse responses (Materials and Methods). The computed skin oscillations are input to integrate-and-fire PC neuron models to produce spiking responses. Here, the stimulus is a 100 Hz sinusoid applied at the digit III DP of P5. (**B**) PC spiking responses (right) evoked by skin oscillations (middle) at selected locations (left, blue dots) elicited by a 100 Hz sinusoidal stimulus applied at the digit III DP of P4 (10 µm max. peak-to-peak displacement across hand). Shown for PC model type 4. Light blue bars: RMS skin displacements; dark blue bars: PC mean firing rates calculated from spikes within the shaded region. (**C**) Upper panel: PC mean firing rates elicited by the stimulus in (B). Lower panel: cumulative percent of total spikes (black) and responding PCs (blue) located within increasing distances from the contact location. Shaded region: results within digit II. (**D**) As in (B) for a bandpass noise stimulus (20 to 800 Hz band, 5 µm max. RMS displacement across hand) applied at the digit II intermediate phalanx (IP) of P1. (**E**) As in (C) for the stimulus in (D).

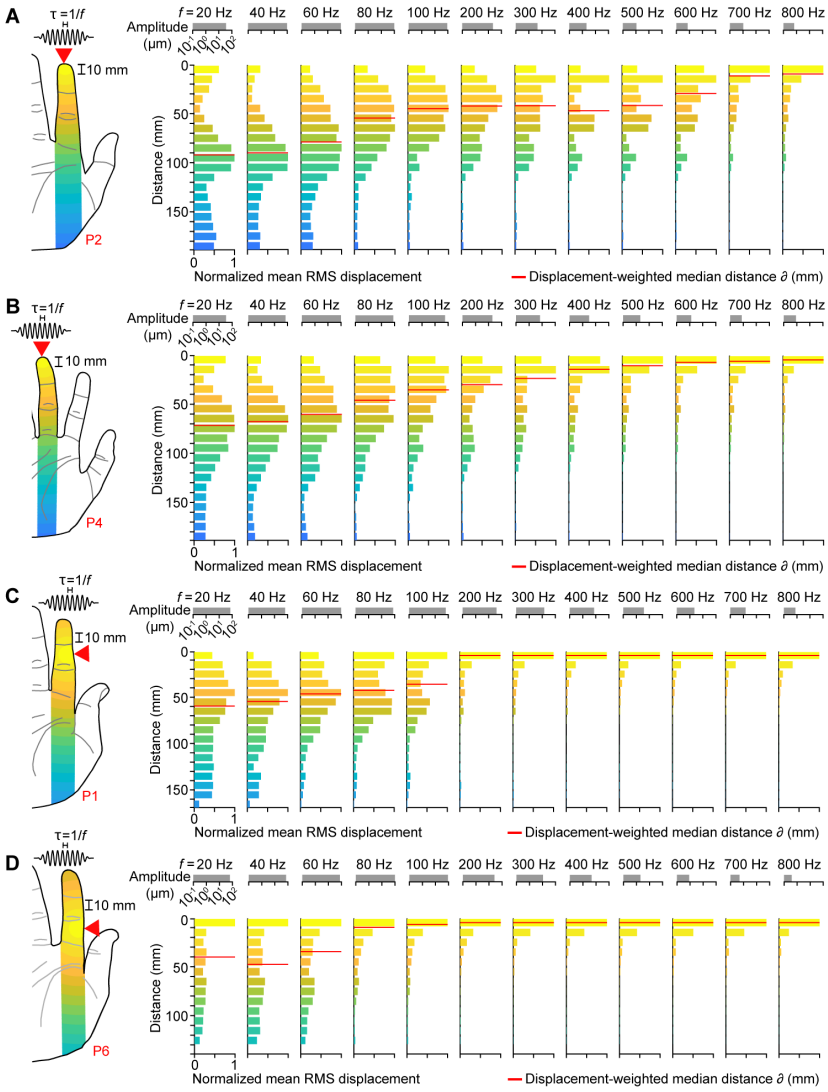

Figure 3.7: **RMS skin displacement distributions across frequency for other contact locations and participants.** (**A**) Normalized root mean square (RMS) skin displacements averaged within 10 mm-wide bands at increasing distances from the contact location (digit II DP) elicited by sinusoidal stimuli of various frequencies (20 to 800 Hz) for P2. Amplitude scale bars (top, gray) show maximum peak-to-peak displacement across the hand at each frequency. Horizontal red lines: median transmission distance; red text: participant number; red arrow: contact location. (**B**) As in (A) for P4 and stimuli applied at the digit III DP. (**C**) As in (A) for P1 and stimuli applied at the digit II IP. (**D**) As in (A) for P6 and stimuli applied at the digit II PP.

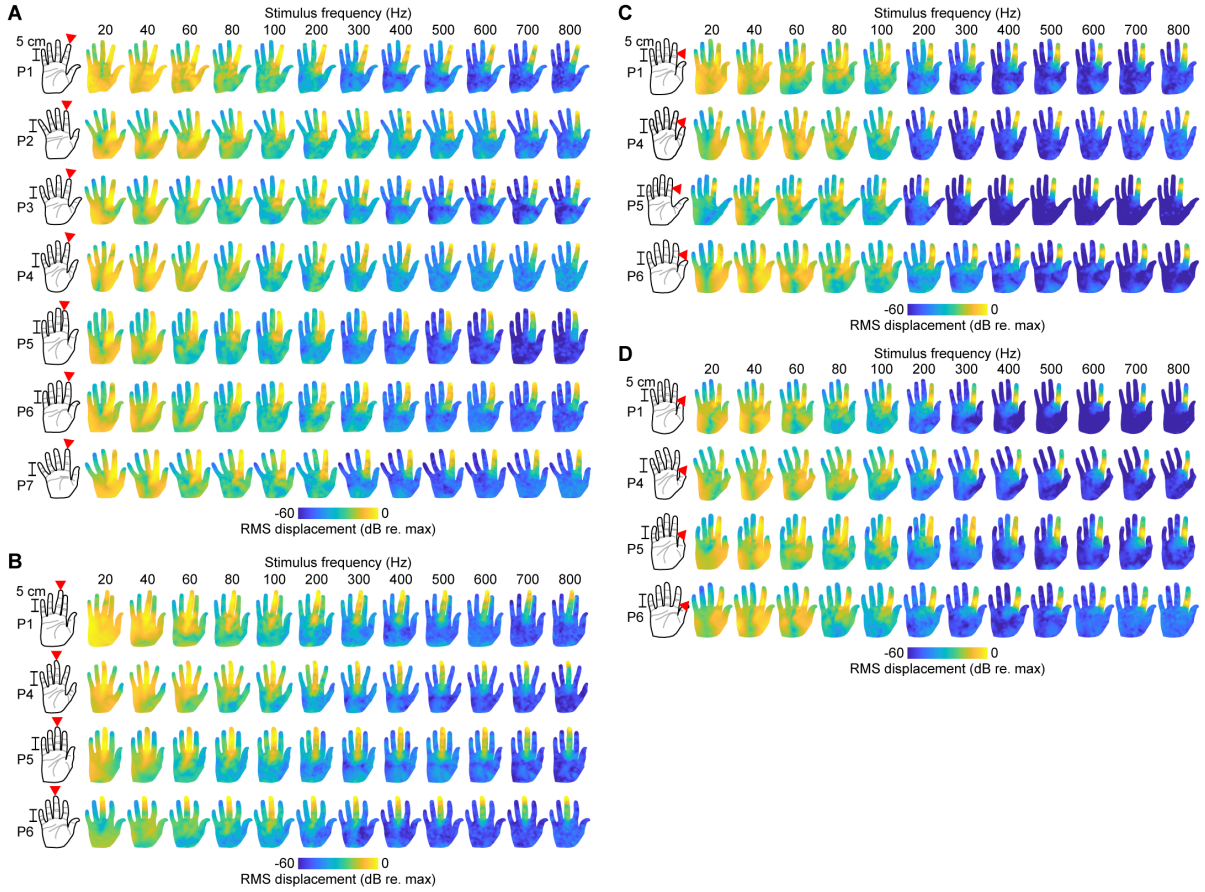

Figure 3.8: **Whole-hand RMS skin displacements across frequency for all contact locations and participants.** (**A**)Normalized whole-hand RMS skin displacements (log scale) elicited by sinusoidal stimuli of various frequencies (20 to 800 Hz) applied at the digit II DP. Shown for all participants. Red text: participant number; red arrow: contact location. (**B**) As in (A) for stimuli applied at the digit III DP. (**C**) As in (A) for stimuli applied at the digit II IP. (**D**) As in (A) for stimuli applied at the digit II PP.

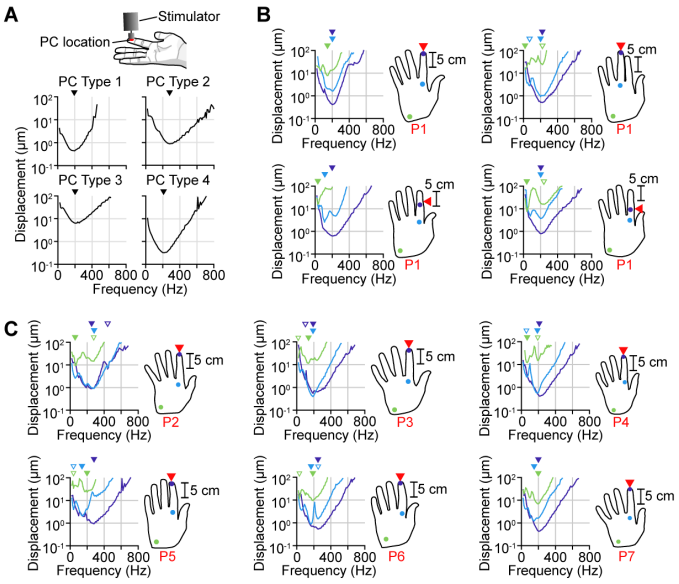

Figure 3.9: **PC entrainment threshold curves for other contact locations and participants.** (**A**) Entrainment threshold curves for PCs located directly underneath the contact location. Shown for all four types of PC neuron models. Triangles above curves: global minimum. (**B**) Entrainment threshold curves for PCs at three locations on the hand for stimuli applied at four different contact locations. Shown for PC model type 4. Red arrow: contact location; red text: participant number; color: PC locations; filled triangles above curves: global minimums; unfilled triangles above curves: other local minima (prominence > 6 dB). (**C**) As in (B), for other participants.

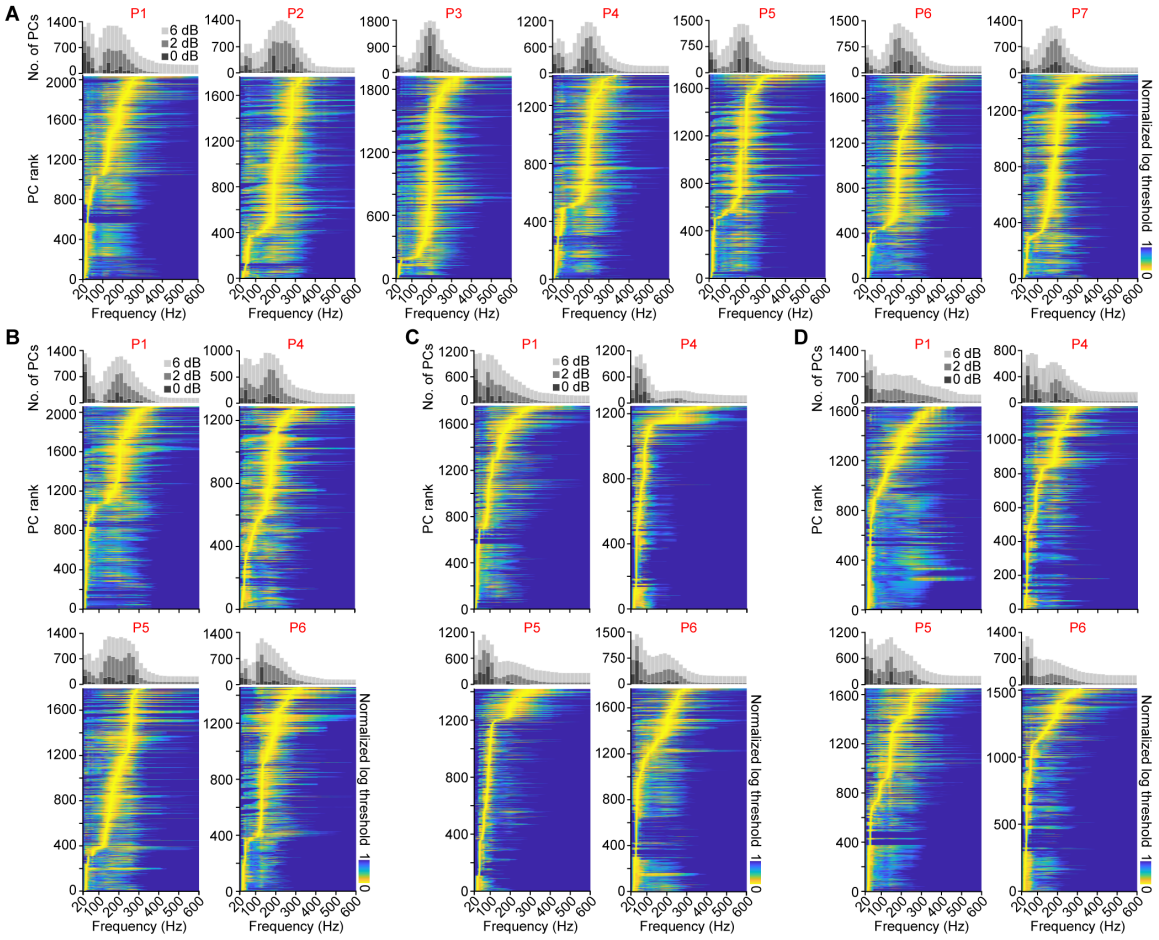

Figure 3.10: **Rank-ordered PC entrainment threshold curves for all contact locations and participants.** (**A**) Entrainment threshold curves for all PCs in the whole-hand population rank-ordered by preferred frequency for stimuli applied at the digit II DP. Each curve is shown on a log scale and normalized from 0 to 1. Histograms show the number of PCs at each frequency with entrainment threshold curve values within 0 dB (light gray), +2 dB (medium gray), and +6 dB (dark gray) of the minimum. Red text: participant number. (**B**) As in (A), for stimuli applied at the digit III DP. (**C**) As in (A), for stimuli applied at the digit II IP. (**D**) As in (A), for stimuli applied at the digit II PP.

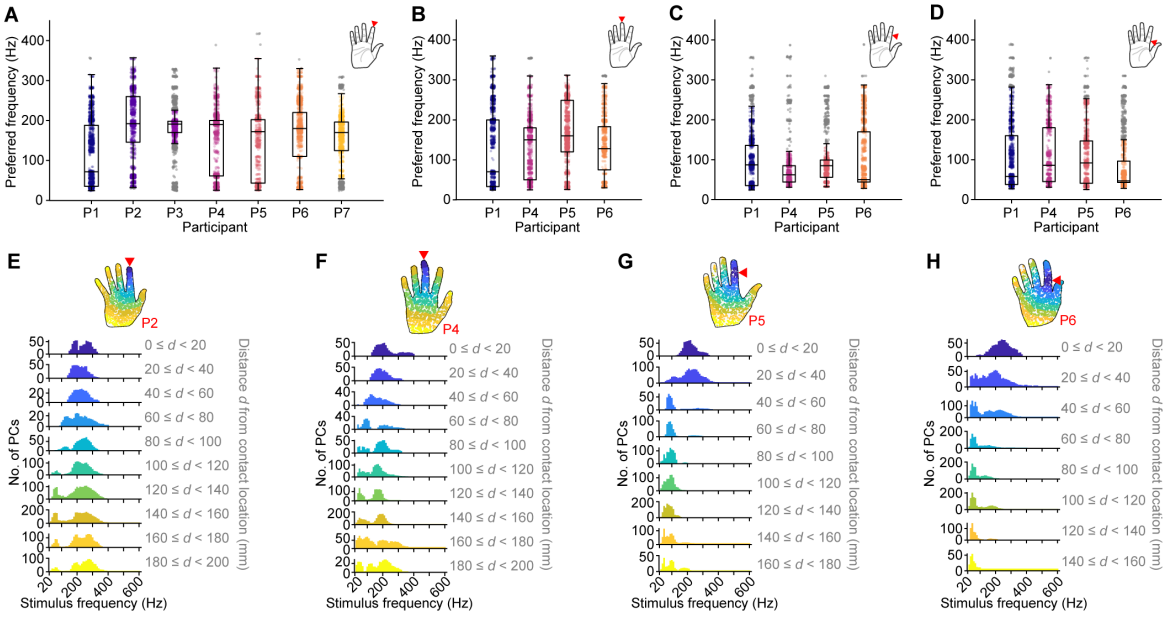

Figure 3.11: **Frequency sensitivity in whole-hand PC populations.** (**A**) Preferred entrainment frequencies across whole-hand PC populations for each participant for stimuli applied at the digit II DP. Red arrow in hand plot (top right): contact location; lower box limits: 25th percentile; upper box limits: 75th percentile; lines within boxes: 50th percentile; whiskers: range of data within one IQR from the lower or upper box limits; colored dots: preferred frequencies within the whiskers; gray dots: outliers. (**B**) As in (A), for stimuli applied at the digit III DP. (**C**) As in (A), for stimuli applied at the digit II IP. (**D**) As in (A), for stimuli applied at the digit II PP. (**E**) Histograms summarizing the number of PCs at each frequency with entrainment threshold curve values within +2 dB of the global minimum for stimuli applied at the digit II DP. PC subpopulations corresponding to each histogram are constructed by selecting PCs located within 20 mm-wide bands at increasing distances from the contact location. Histogram color corresponds to the colored PC subpopulations shown in the hand plot (top). Gray text: distance d from contact location; red arrow: contact location; red text: participant number. (**F**) As in (E), for stimuli applied at the digit III DP. (**G**) As in (E), for stimuli applied at the digit II IP. **H** As in (E), for stimuli applied at the digit II PP.

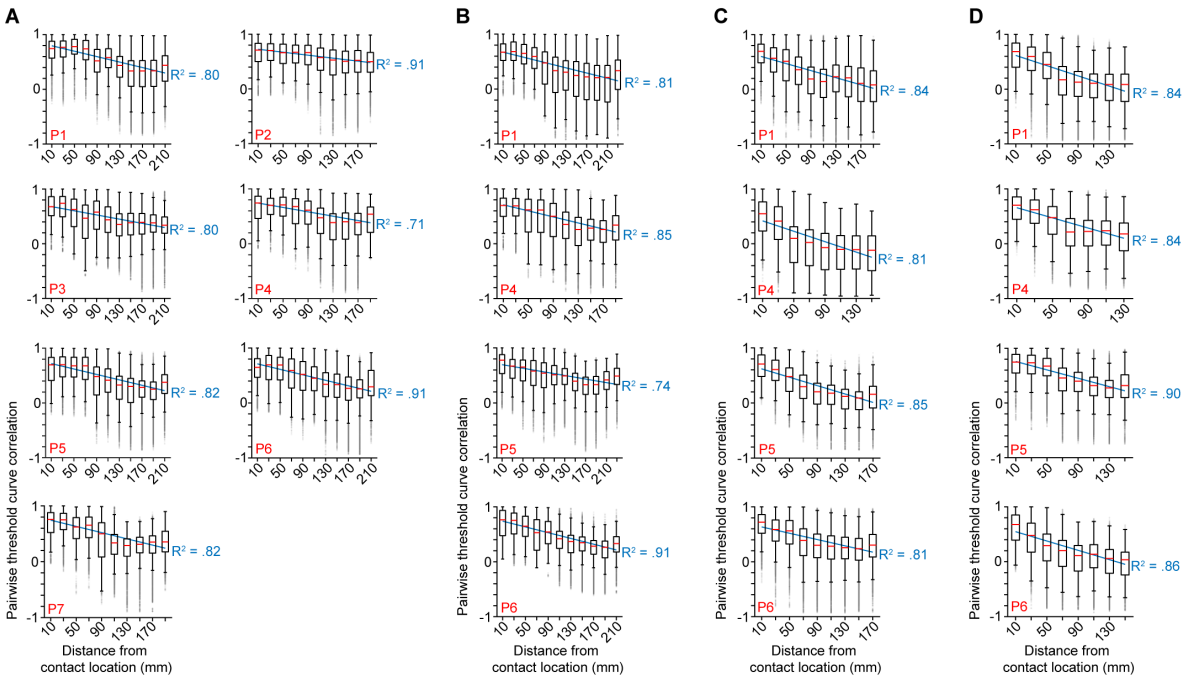

Figure 3.12: **Entrainment threshold curve correlations between PC subpopulations at various distances from the contact location.** (**A**) Pearson correlation coefficients between pairs of entrainment threshold curves of PCs located within 10 mm of the contact location (digit II DP) and those of PCs located within 20 mm-wide bands at increasing distances from the contact location. X-axis labels denote the center distance of each band. Red midlines: median; lower box limits: 25th percentile; upper box limits: 75th percentile; whiskers: range of data within one IQR from the lower or upper box limits; gray dots: outliers; gray dotted lines: linear fit of medians; gray text: R^2 value for linear fit; red text: participant number. (**B**) As in (A) for a contact location at the digit III DP. (**C**) As in (A), for a contact location at the digit II IP. (**D**) As in (A), for a contact location at the digit II PP.

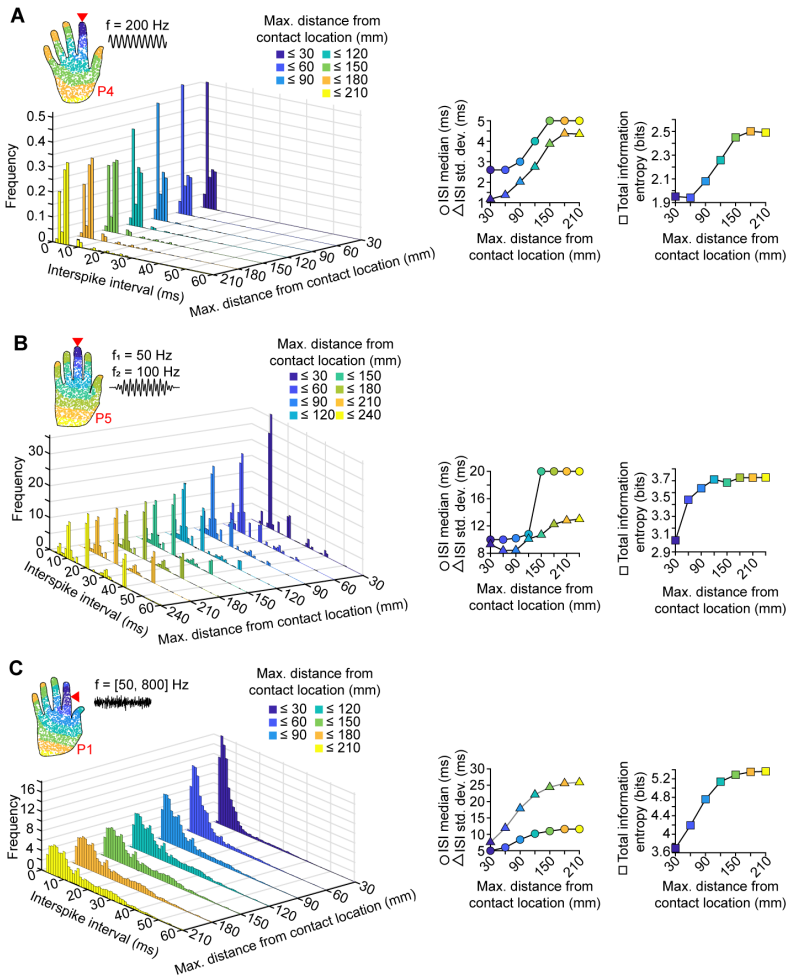

Figure 3.13: **ISI distributions constructed from PCs located within increasing distances from the contact location.** (**A**) Left panel: Histograms comprising interspike intervals (ISIs) from PCs located within increasing distances from the contact location (hand inset) in response to a sinusoidal stimulus (200 Hz, 15 µm max. peak-to-peak displacement across hand). Right panel: median (circles), standard deviation (triangles), and total information entropy (squares) of the ISI histograms shown above. Color: maximum distance from the contact location; red arrow: contact location; red text: participant number. (**B**) As in (A), for a diharmonic stimulus (f_1 = 50 Hz, f_2 = 100 Hz, 10 µm max. peak-to-peak displacement across hand for both f_1 and f_2). (**C**) As in (A), for a bandpass-filtered noise stimulus (50 to 800 Hz band, 5 µm max. RMS displacement across hand).

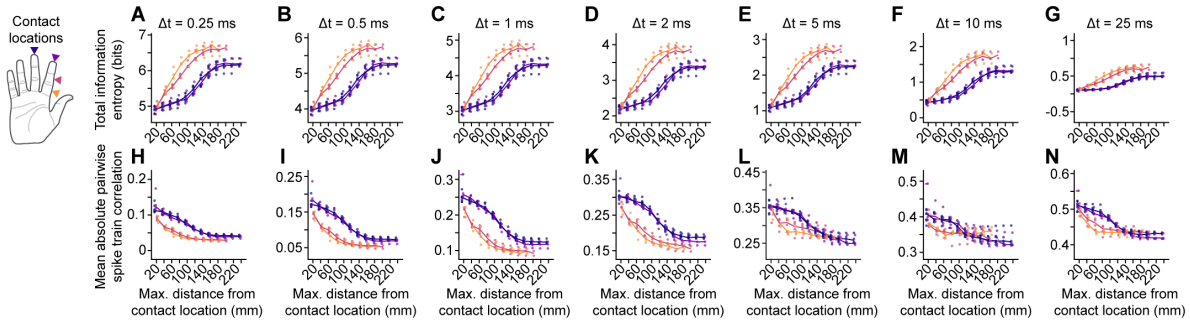

Figure 3.14: **Information entropy of ISI histograms and mean spike train correlations for different bin sizes.** (**A**) Total information entropy (bits) of histograms comprising ISIs from PCs located within increasing distances from the contact location in response to a diverse stimulus set (see Methods) for an ISI histogram bin width of $\Delta t = 0.25\,\text{ms}$. Colors: contact location corresponding to arrows in hand plot (top left); dots: data points for all participants; lines: median. (**B**) As in (A), for an ISI histogram bin width of $\Delta t = 0.5\,\text{ms}$. (**C**) As in (A), for an ISI histogram bin width of $\Delta t = 1\,\text{ms}$. (**D**) As in (A), for an ISI histogram bin width of $\Delta t = 2\,\text{ms}$. (**E**) As in (A), for an ISI histogram bin width of $\Delta t = 5\,\text{ms}$. (**F**) As in (A), for an ISI histogram bin width of $\Delta t = 10\,\text{ms}$. (**G**) As in (A), for an ISI histogram bin width of $\Delta t = 25\,\text{ms}$. (**H**) Mean absolute spike train correlation between all pairs of PCs located within increasing distances from the contact location for a spike train histogram bin width of $\Delta t = 0.25\,\text{ms}$. Colors: contact location corresponding to arrows in hand plot (top left); dots: data points for all participants; lines: median. (**I**) As in (H), for a spike train histogram bin width of $\Delta t = 0.5\,\text{ms}$. (**J**) As in (H), for a spike train histogram bin width of $\Delta t = 1\,\text{ms}$. (**K**) As in (H), for a spike train histogram bin width of $\Delta t = 2\,\text{ms}$. (**L**) As in (H), for a spike train histogram bin width of $\Delta t = 5\,\text{ms}$. (**M**) As in (H), for a spike train histogram bin width of $\Delta t = 10\,\text{ms}$. (**N**) As in (H), for a spike train histogram bin width of $\Delta t = 25\,\text{ms}$.

Chapter 4

Spatiotemporal Organization of Touch Information in Tactile Neuron Population Responses

Neuroscience research has emphasized the importance of investigating sensory systems in natural settings, but this is a challenging task for the tactile system due to experimental constraints. This chapter builds on the vibrometry-driven neural simulation methodology from Chapter 3 to examine how active, unconstrained touch interactions—including tapping, sliding, and grasping with one or more fingers—are spatiotemporally encoded by whole-hand mechanoreceptor populations. It also demonstrates that mechanoreceptors far from the locations of direct touch contact can encode tactile information by leveraging biomechanical transmission. Building on this idea, Chapter 5 presents a wearable device that utilizes biomechanical transmission to capture and interpret remote touch contact. Furthermore, Chapter 6 enables the computational analysis of biomechanical transmission across the upper limb in response to touch interactions applied at one or more locations on the hand, such as those investigated in this chapter.

The content of Chapter 4 is adapted from [16], © 2023 IEEE. Reprinted, with permission, from

N. Tummala, Y. Shao, Y. Visell, Spatiotemporal Organization of Touch Information in Tactile Neuron Population Responses. *2023 IEEE World Haptics Conference (WHC)*, 2023. DOI: https://doi.org/10.1109/WHC56415.2023.10224467.

Abstract

Manual touch interactions elicit widespread skin vibrations that excite spiking responses in tactile neurons distributed throughout the hand. The spatiotemporal structure of these population responses is not yet fully understood. Here, we evaluate how touch information is encoded in the spatiotemporal organization of simulated Pacinian corpuscle neuron (PC) population responses when driven by a vibrometry dataset of whole-hand skin motion during commonly performed gestures. We assess the amount of information preserved in these peripheral population responses at various spatiotemporal scales using several non-parametric classification methods. We find that retaining the spatial structure of the whole-hand population responses is important for encoding touch gestures while conserving the temporal structure becomes more consequential for gesture representation in the responses of PCs located in the palm. In addition, preserving spatial structure is more beneficial for capturing gestures involving single rather than multiple digits. This work contributes to further understanding the sense of touch by introducing novel measurement-driven computational methods for analyzing the population-level neural representations of natural touch gestures over multiple spatiotemporal scales.

4.1 Introduction

Touch interactions performed with the hands elicit mechanical vibrations that propagate throughout the skin [1, 2, 4, 13, 55]. These propagating vibrations facilitate touch perception by exciting responses in widespread populations of sensory neurons [12, 17, 14], including those innervating Pacinian corpuscles (PCs). PCs have large receptive fields [72] and are exquisitely sensitive to vibrations elicited by touch interactions such as fine manipulation, texture scanning, and tool use [85, 89, 27]. While spiking responses of isolated PCs elicited by laboratory stimuli are thoroughly characterized [93, 90, 99], the responses of PC populations throughout the hand are not well understood. In addition, few studies have examined PC responses to propagating vibrations originating at locations far removed from the PC locations. This is partly due to experimental limitations that preclude the measurement of signals from PC populations in an unconstrained hand [133].

Previous research has underscored the significance of investigating population encoding in understanding the sense of touch [150, 83]. Numerous studies have characterized the responses of tactile neuron populations to controlled laboratory stimuli, examining parameters such as intensity [98, 246], frequency [112], textural vibration content [130, 241, 115], and edge orientation [247], and demonstrated that touch information is encoded at various spatial and temporal scales. To explore the spatiotemporal structure of information encoded in population responses, several investigations, including those in other areas of sensory neuroscience, have utilized stimulus discrimination tasks conducted via metric space and classification methods [248, 249, 112, 247, 113, 250, 111, 251]. However, our understanding of information encoding within the spatiotemporal organization of PC population responses in natural contexts remains limited.

In this paper, we employ a novel measurement-driven approach for simulating the responses of a spatially distributed population of PCs in the hand during natural touch

interactions. Leveraging existing vibrometry measurements of whole-hand skin motion collected during commonly performed tapping, sliding, and grasping gestures involving contact at the digits [1, 2], we drive an ensemble of neuron models developed in prior research [67]. We then utilize several machine learning techniques to investigate the spatiotemporal encoding of information generated by these touch interactions in PC population responses. We find that preserving spatial structure in whole-hand PC responses is beneficial for capturing gesture-specific information, particularly for single-digit gestures, while retaining spike timing becomes more informative for gesture representation by PCs located in the palm. The findings and methodologies presented here may contribute to knowledge about the spatiotemporal organization of touch information in PC population responses and may inform the engineering of new haptic or robotic technologies that reflect attributes of tactile sensing and perception in the human hand [189, 202, 203, 207].

In the following section, we describe our methods for integrating spiking neuron models [67] with mechanical measurements [1, 2], computing population spiking response representations by multi-scale spatiotemporal integration, and analyzing information content preserved by these representations using machine-learning techniques. We then discuss and analyze the results of these studies and their implications for touch information encoding in PC population responses. We conclude by synthesizing these findings and discussing their significance for haptic science and engineering and opportunities for future research.

4.2 Methods

Using the methods detailed in this section, we sought to quantify how much touch gesture information was retained in PC population responses at different spatial and temporal scales. PC population responses were generated by driving physiologically-

informed neuron models adapted from previous research [67] with an existing vibrometry dataset of skin motion measurements collected during everyday touch interactions[1, 2]. To modify the spatiotemporal structure of these population responses, we summed spiking data over spatial and temporal bins of different sizes, allowing us to capture touch gesture information at multiple spatiotemporal scales. We then used machine learning classifiers to analyze how much gesture information was preserved in these spatiotemporal response representations.

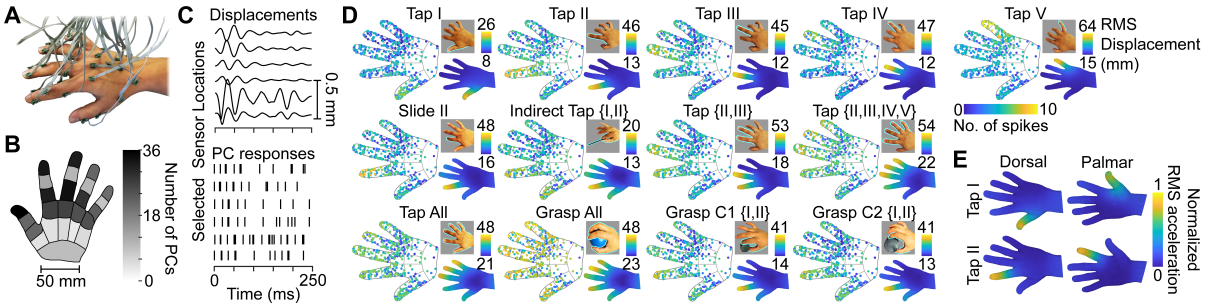

Figure 4.1: A) Placement of the accelerometer array on the dorsal surface of a participant's hand [1, 2]. B) Number of PCs uniformly distributed within each region of the hand, derived from [3]. C) Skin displacements (top) and corresponding PC spiking responses (bottom) at selected sensor locations during one trial of the Slide II gesture. D) Shown for each of the 13 performed gestures: number of spikes produced by each PC in the hand averaged across all trials of the gesture (left), an image of a participant executing the gesture (top right), and RMS skin displacements elicited across the whole hand during the gesture (bottom right). E) RMS skin accelerations elicited across the dorsal (left column) and volar (right column) surfaces of the hand during one trial of the Tap I gesture (top row) and one trial of the Tap II gesture (bottom row), normalized by the maximum skin acceleration produced during each trial [2].

4.2.1 Whole-Hand Skin Vibrometry Data

Our methodology leveraged an existing dataset of whole-hand skin vibration measurements captured in a prior experiment during manual touch gestures performed by four participants using an array of 30 miniature accelerometers [1, 2]. The accelerometers were worn on the dorsal surface of the hand during data collection, allowing unob-

structed movement during gesture execution (Fig. 4.1A). Accelerometers were placed at the same relative anatomical positions on each hand, standardizing their locations across participants. The gestures were comprised of commonly performed manual interactions (Fig. 4.1D). Each gesture was repeated for either 100 (grasping gestures) or 200 (all other gestures) trials. The patterns of skin vibrations elicited during gestures involving fingertip movement were found to be similar between the volar and dorsal surfaces of the hand in a prior investigation (Fig. 4.1E) [2], allowing the utilization of the dorsal skin oscillation measurements as an approximation of volar skin motion.

Data from each trial were time-aligned with respect to the instant of surface or object contact, truncated to a duration of 250 ms, and band-pass filtered between 20-500 Hz. Acceleration measurements were converted to displacement via double integration. To facilitate analysis, the three-axis data from each sensor were independently projected to a principal axis of oscillation through principal component analysis (PCA). The projection maximally preserved variance in the data. The processed data from each trial consisted of time-varying signals of 250 ms duration sampled at 2.0 kHz from each of 30 accelerometers, yielding 15000 samples per trial. The dataset consisted of 4564 trials in total.

4.2.2 Vibrometry-Driven Neural Simulations

The processed skin displacement signals were used as inputs to a population of K physiologically-informed PC neuron models [67] that produced spiking responses for each trial, where $K = 490$ unless otherwise specified (Fig. 4.1C, D). The highly stereotyped and reproducible responses of PCs were captured with high fidelity by the utilized neuron models, which were trained and extensively validated on microneurography data collected from macaque monkeys in prior research [98]. PCs were distributed across a 3D hand

model according to a recent MRI study on PC distribution in the glabrous skin that dictated the number of PCs that were uniformly distributed within each hand region (Fig. 4.1B) [3]. Skin displacements were interpolated to each PC location using an inverse distance filter informed by biomechanical measurements and described in a previous publication [2], with distance calculated on the dorsal surface of the 3D hand model.

4.2.3 Spatiotemporal Spike Count Representations

To analyze the PC population responses at various temporal scales, six time bin widths, Δt, were defined in decreasing order of preserved temporal resolution. These widths were $\Delta t \in \{5, 10, 25, 50, 125, 250\}$ ms, and the number of time bins was calculated as $N = \frac{250}{\Delta t} = \{50, 25, 10, 5, 2, 1\}$. To analyze the PC population responses at various spatial scales, two distinct collections of sets of spatial bins were defined, with one collection encompassing the whole hand (WH) and the other encompassing only the palm (P). A set of spatial bins was defined as a set of M non-overlapping contiguous spatial regions in the hand based on anatomical regions defined in Fig. 4.2A. To analyze the whole-hand PC population responses, four sets of spatial bins, each denoted as $\mathbf{s}$, were defined in decreasing order of preserved spatial resolution, as illustrated in Fig. 4.2B. They were as follows:

1. $\mathbf{s} =$ WH1, $M = K$: Each PC in the hand ($K = 490$, unless otherwise specified),
2. $\mathbf{s} =$ WH2, $M = 25$: the distal phalanges (DP), medial phalanges (MP), proximal phalanges (PP), metacarpophalangeal joint regions (MCP), and metacarpal (MC) regions corresponding to each digit (I-V) and the carpal (C) region of the palm,
3. $\mathbf{s} =$ WH3, $M = 6$: each digit (I-V) and the palm,
4. $\mathbf{s} =$ WH4, $M = 1$: and the whole hand.

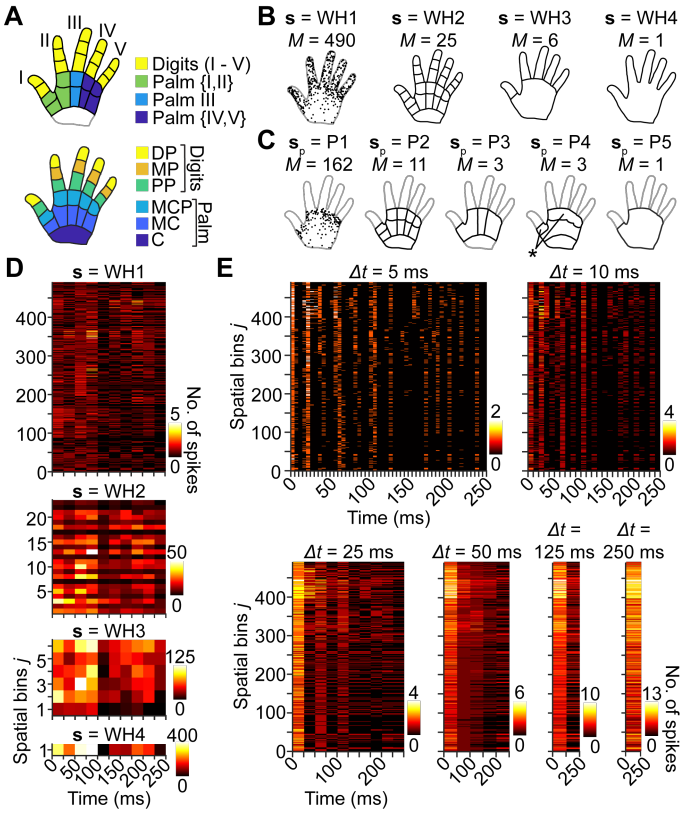

Figure 4.2: A) Anatomically-based hand regions defined for spatial resolution analyses. Within the digits, DP are distal phalanges, MP are medial phalanges, and PP are proximal phalanges. Within the palm, MCP are metacarpophalangeal joint regions, MC are metacarpal regions, and C is the carpal region. B) Four sets of spatial bins ($\mathbf{s}$ = WH1-WH4) defined for whole-hand analyses where M is the size of each set. Each PC in the hand is considered a separate spatial bin in WH1. Each spatial bin in WH2-WH4 is outlined by solid black lines. C) Five sets of spatial bins ($\mathbf{s}_p$ = P1-P5) defined for analyses in the palm where M is the size of each set. Each PC in the palm is considered a separate spatial bin in P1. Each spatial bin in P2-P5 is outlined by solid black lines. Regions outlined by light gray lines are not included in the spatial bins. Regions indicated by the star label (*) in P4 are part of the same spatial bin. D) Binned spike train matrices representing a PC population response elicited by one trial of the Grasp All gesture shown across all sets of whole-hand spatial bins $\mathbf{s}$ = WH1-WH4 when $\Delta t = 25$ ms. E) Binned spike train matrices representing a PC population response elicited by one trial of the Tap V gesture shown across all time bin widths Δt when $\mathbf{s}$ = WH1.

To analyze PC population responses from the palm, five sets of spatial bins, each denoted as $\mathbf{s}_p$, were defined in decreasing order of preserved spatial resolution, as illustrated in Fig. 4.2C. They were as follows:

1. $\mathbf{s}_p = \text{P1}$, $M = 162$: Each PC in the palm,
2. $\mathbf{s}_p = \text{P2}$, $M = 11$: the MCP and MC regions corresponding to each digit (I-V) and C,
3. $\mathbf{s}_p = \text{P3}$, $M = 3$: the Palm {I,II}, Palm III, and Palm {IV,V} regions,
4. $\mathbf{s}_p = \text{P4}$, $M = 3$: all MCP, MC, and C regions without digit separation,
5. $\mathbf{s}_p = \text{P5}$, $M = 1$: and the whole palm.

Using these bins, the PC population spiking response for each trial was quantified as a binned spike train matrix B of size $M \times N$, where M was the number of spatial bins and N was the number of time bins. The element B_{ij} contained the number of spikes generated in time bin j by PCs situated in spatial bin i. This representation allowed us to control the spatiotemporal resolution of the population responses by manipulating the bin sizes without employing dimensionality reduction methods that would complicate the analysis.

The sets of spatial bins ranged from preserving individual neuron identity of spikes ($\mathbf{s} = \text{WH1}$ or $\mathbf{s}_p = \text{P1}$) to aggregating spikes across the whole PC population ($\mathbf{s} = \text{WH4}$ or $\mathbf{s}_p = \text{P5}$), as shown for one trial of the Grasp All gesture (Fig. 4.2D). Similarly, the time bin widths varied from capturing detailed spike timing ($\Delta t = 5\,\text{ms}$) to summing spike counts over the entire trial ($\Delta t = 250\,\text{ms}$), as demonstrated for one trial of the Tap V gesture (Fig. 4.2E). These variations in spatiotemporal representations impacted the degree to which differences in PC population responses evoked by various natural touch gestures were captured.

4.2.4 Evaluation of Touch Information in Spatiotemporal Spike Count Representations

We employed four non-parametric classification methods to elucidate the amount of information encoded in the spatiotemporal structure of PC population responses elicited by natural touch gestures. These methods included a linear kernel support vector machine (SVM), a k-nearest neighbors classifier (kNN), a peristimulus spike timing histogram (PSTH) template-based classifier (PTB) [248, 249], and an average pairwise distance classifier (APD). These techniques were applied to binned spike train matrices to analyze the extent to which PC population responses retained information across spatiotemporal scales.

For the SVM and kNN classifiers, reported classification accuracies were averaged over a 10-fold cross-validation procedure with a random 90-10 train-test split. For the SVM classifier, each feature was standardized using the mean and standard deviation calculated from the training dataset. For kNN, $k = 5$ was chosen based on parameter selection during pre-testing. The kNN and APD classifiers utilized a distance matrix composed of pairwise Euclidean distances between binned spike train matrices for all trials. For the PTB and APD classifiers, results were averaged over a leave-one-out cross-validation procedure where each trial was successively designated as the test set while the rest of the dataset comprised the training set. For the PTB classifier, template PSTHs were calculated for each gesture by taking the element-wise average over binned spike train matrices from all trials of the gesture, excluding the test trial. The test trial was then classified as the gesture corresponding to the PSTH for which the pairwise Euclidean distance was the smallest. The APD classifier classified each test trial as the gesture corresponding to the training samples for which the average pairwise Euclidean distance to the test trial was the smallest.

4.3 Results

The responses of tactile neuron populations encode information about mechanical stimuli in both the spike timing and the identity of neurons generating each spike[130, 247, 112, 115]. Here, we presented the results of our investigation on how information about natural touch gestures was preserved in spike count representations at multiple spatiotemporal scales and within hand regions away from the contact location. We quantified the captured information through the overall and per-gesture classification accuracies achieved by several non-parametric classification methods.

4.3.1 Varying the Spatiotemporal Resolution of Spike Count Representations

Whole-Hand PC Population Responses

Our analysis showed that modifying the spatial resolution of spike count representations had a greater impact on touch gesture classification than modifying the temporal resolution. When individual neuron identity was preserved and temporal structure eliminated ($\mathbf{s}$ = WH1, Δt = 250 ms), the average classification accuracy was 75 % for SVM, 73 % for kNN, and 46 % for PTB and APD (Fig. 4.3A). On the other hand, when precise spike timing was preserved and spatial structure eliminated ($\mathbf{s}$ = WH4, Δt = 5 ms), the average classification accuracy dropped significantly: by 33 % for SVM, 28 % for kNN, 15 % for PTB, and 18 % for APD. Additionally, the median range of classification accuracies across changes in spatial resolution was greater than that across changes in temporal resolution by a factor of at least 2 for all classifiers (Fig. 4.3B). When some spatial structure was preserved ($\mathbf{s}$ = WH1, WH2, or WH3), all classifiers performed best at Δt = 25-50 ms, suggesting that an intermediate level of temporal integration was

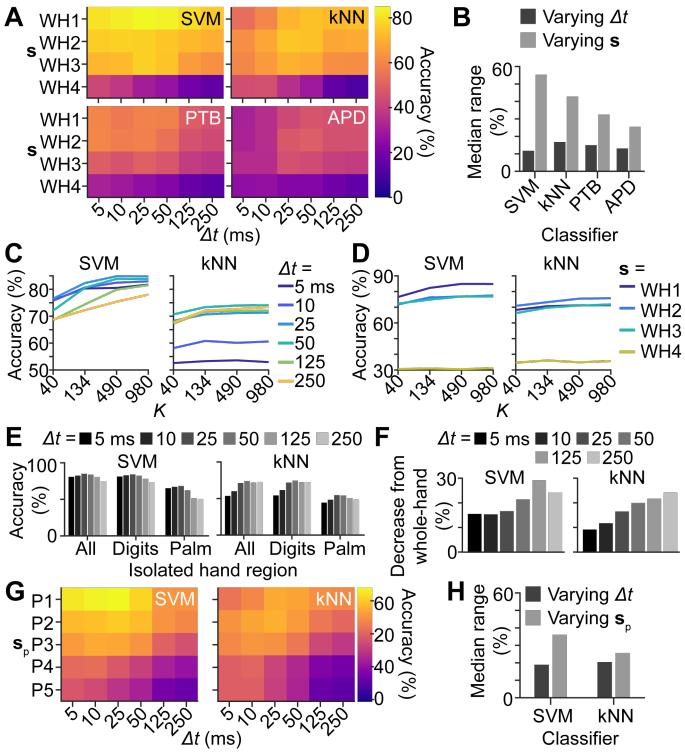

Figure 4.3: A) Matrix of average classification accuracies achieved using whole-hand PC responses for all combinations of Δt and $\mathbf{s}$ by all classifiers. B) Median range of classification accuracies using whole-hand PC responses across changes in Δt (dark gray) and across changes in $\mathbf{s}$ (light gray) for all classifiers. C) Classification accuracy as the total number of PCs in the hand K varies for all Δt when $\mathbf{s}$ = WH1. D) Classification accuracy as the total number of PCs in the hand K varies for all $\mathbf{s}$ when $\Delta t = 25$ ms. C) and D) are shown for both SVM (left) and kNN (right). E) Average classification accuracies using PC responses from the whole hand (All), from only the digits (Digits), and from only the palm (Palm) for all Δt. Shown for SVM (left) and kNN (right). F) Decrease in average classification accuracy from using whole-hand PC responses to using PC responses from the palm for all Δt. Shown for SVM (left) and kNN (right). There was no spatial integration performed for E) and F); each PC was a separate spatial bin. G) Matrix of average classification accuracies achieved using PC responses from the palm for all combinations of Δt and $\mathbf{s}_p$ by SVM (left) and kNN (right). H) Median range of classification accuracies using PC responses from the palm across changes in Δt (dark gray) and across changes in $\mathbf{s}_p$ (light gray) for SVM (left) and kNN (right).

beneficial in accommodating variations in touch information across trials.

While the goal of this research was not to analyze the suitability of classification methods for this gesture discrimination task, the findings showed that SVM performed best for all spatiotemporal representations except when $\mathbf{s} = \text{WH4}$, where it was outperformed by kNN for $\Delta t \leq 25\,\text{ms}$. On the other hand, PTB and APD achieved the lowest average classification accuracies except at coarse spatiotemporal resolution ($\Delta t \geq 125\,\text{ms}$ and $\mathbf{s} = \text{WH4}$), demonstrating that they were more sensitive than other methods to small perturbations between trials. The remaining analyses focus on SVM and kNN, as they performed better than PTB and APD in almost all cases and are sufficient to represent our overall findings, which are consistent across all classifiers. Additionally, as the results were robust to scaling of the PC population size (Fig. 4.3C, D), $K = 490$ was utilized for all other analyses.

PC Population Responses From the Palm

Analyses of responses from PCs restricted to the digits yielded gesture classification accuracies nearly as high as those obtained from whole-hand PC responses at all temporal resolutions (Fig. 4.3E), likely due in part to the large proportion of touch contacts that occurred at the digits in the utilized dataset. However, prior findings have demonstrated that tactile neurons remote from the stimulus location can encode touch information via mechanical wave propagation [112, 12, 17]. This motivated our subsequent analysis of gesture encoding at various spatiotemporal scales by PC subpopulations restricted to the palm.

Consistent with the findings from the aforementioned studies, our results showed that gestures were readily recognized when PCs were isolated in the palm. Average classification accuracy was 66 % in the best case (SVM, $\mathbf{s}_p = \text{P1}$, $\Delta t = 25\,\text{ms}$) (Fig. 4.3E, G). The smallest decrease in performance from whole-hand classification occurred at fine

temporal resolutions ($\Delta t \leq 10\,\text{ms}$) (Fig. 4.3F). This finding demonstrates that without the contribution of spiking responses from PCs located in the digits, precise spike timing played a larger role in gesture discrimination.

Similar to whole-hand analysis results (Fig. 4.3B), classification accuracy varied more across changes in spatial resolution than temporal resolution (Fig. 4.3H). However, the median range of classification accuracies increased by 5 % for changes in temporal resolution while decreasing by nearly 20 % for changes in spatial resolution compared to the whole-hand analysis results for both classifiers. This finding again indicates that the preservation of temporal structure became more consequential for the representation of touch gestures by PC subpopulations in the palm.

Nonetheless, spatial structure still impacted the encoding of gesture information in the palm. Classification accuracy was significantly higher when PC responses were integrated across palmar regions oriented along the axis of the digits ($\mathbf{s}_p$ = P3) than when integrated across regions oriented orthogonal to the digits ($\mathbf{s}_p$ = P4), despite both sets containing an equal number of spatial regions ($M = 3$) (Fig. 4.3G). The integration of spikes over $\mathbf{s}_p$ = P3 effectively preserved information about individual digits or pairs of digits, while such preservation was absent in the integration of spikes over $\mathbf{s}_p$ = P4. These results demonstrate the importance of retaining a minimal level of digit separation within the spatial structure of the spike count representations.

4.3.2 Varying the Spatiotemporal Resolution of Gesture-Level Spike Count Representations

We next explored the representation of touch information associated with individual gestures across variations in the spatiotemporal resolution of whole-hand spike count representations. Single-digit gestures were better represented than multi-digit gestures

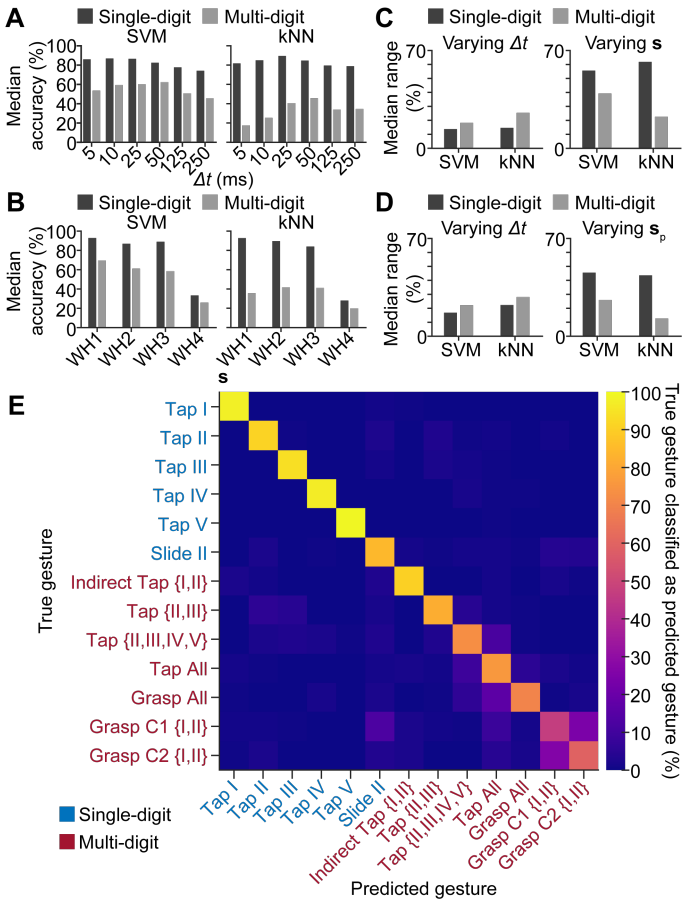

Figure 4.4: A) Median classification accuracy of single-digit (dark gray) and multi--digit (light gray) gestures for all Δt using whole-hand PC responses. The median is computed across all $\mathbf{s}$ and all single- or multi-digit gestures. B) Median classification accuracy of single-digit (dark gray) and multi-digit (light gray) gestures for all $\mathbf{s}$ using whole-hand PC responses. The median is computed across all Δt and all single- or multi-digit gestures. C) Median range of classification accuracies of single-digit (dark gray) and multi-digit (light gray) gestures across changes in Δt (left) and across changes in $\mathbf{s}$ (right) using whole-hand PC responses. D) Median range of classification accuracies of single-digit (dark gray) and multi-digit (light gray) gestures across changes in Δt (left) and across changes in $\mathbf{s}_p$ (right) using PC responses from the palm. In C) and D), when varying Δt, the median is computed over all $\mathbf{s}$ or $\mathbf{s}_p$ and all single- or multi-digit gestures. Similarly, when varying $\mathbf{s}$ or $\mathbf{s}_p$, the median is computed over all Δt and all single- or multi-digit gestures. E) Confusion matrix showing the percent of each gesture (True) classified as another gesture (Predicted) for the best-performing classifier (SVM, $\mathbf{s}$ = WH1, $\Delta t = 25$ ms) using whole-hand PC responses. Per-gesture classification accuracy is read from the diagonal of the matrix. False positives are read from the columns, and false negatives are read from the rows.

under most spatiotemporal conditions, except when spatial information was eliminated ($\mathbf{s}$ = WH4) (Fig. 4.4A, B). In addition, single-digit gestures were classified most accurately when Δt = 10-25 ms, while multi-digit gestures were best captured at a lower temporal resolution ($\Delta t = 50$ ms). These performance differences between gesture types may have been a consequence of high trial-to-trial variability in the timing of contact with the target surface or object by the individual digits involved in the multi-digit gestures.

Additionally, we found that spatial structure played a larger role in representing single-digit gestures, while temporal structure was more consequential for capturing multi-digit gestures. The median range of classification accuracies when varying spatial resolution was greater for single-digit gestures, while the median range when varying temporal resolution was slightly greater for multi-digit gestures (Fig. 4.4C). This trend was preserved for PC responses from the palm (Fig. 4.4D). Though spatial structure still played a significant role in encoding multi-digit gestures, it was more beneficial for representing single-digit gestures.

For the best-performing classifier (SVM, Δt = 25 ms, $\mathbf{s}$ = WH1), most misclassifications occurred between cylinder grasps (Grasp C1 {I,II} and Grasp C2 {I,II}) and between gestures requiring most or all of the digits (Tap {II,III,IV,V}, Tap All, and Grasp Ball All) (Fig. 4.4E). Cylinder grasps were commonly confused because they were identical apart from the cylinder sizes, varying in radius by only 1.6 cm. Misclassifications also occurred between single-digit tapping gestures and between Slide II and cylinder grasps. PC population responses in the palm contained less information enabling the distinction between multi-digit gestures and their component single-digit gestures. This was demonstrated by misclassifications between Tap {II,III} and its corresponding single-digit gestures Tap II and Tap III and between the cylinder grasps and their constituent single-digit gestures Tap I and Tap II. Further misclassifications occurred between multi-digit taps and grasps.

4.4 Discussion and Conclusion

Our work investigated the spatiotemporal organization of touch information in PC population spiking responses elicited during common touch gestures. We examined the amount of gesture information preserved within the responses at different spatiotemporal scales via a novel vibrometry-driven neural simulation method adapted from prior research [67, 1, 2]. The elicited PC population responses were spatiotemporally integrated and analyzed using several machine learning techniques. Our results showed that the spatial structure of PC population responses played a significant role in encoding information about touch gestures, especially single-digit gestures. The temporal structure of PC population responses was also meaningful, particularly for PCs in the palm.

While these findings necessarily reflect the scope of the included gestures, which do not capture the full range of manual interactions involved in all activities, they nevertheless furnish insight into the spatiotemporal organization of natural touch information in PC population responses in conditions with greater ecological validity than are generally probed in many laboratory experiments. The analyzed dataset included several multi-finger tapping and grasping gestures and many gestures engaging one or two digits. The selection of gestures was informed by prior studies demonstrating that the majority of natural contact events occur at the fingertips [252]. Our findings suggest that the relative importance of temporal structure in touch information encoding within PC population responses may have been enhanced if the analyzed dataset placed greater emphasis on grasping or multi-digit gestures.

Although the methods employed here are approximate, few alternatives are available since existing methods preclude the measurement of neural population responses in the periphery during natural touch behavior. Multiple classification methods and parameters were employed to validate the findings presented here. Despite variations between

results obtained with different classifiers, which may reflect differences in their expressive capacity, qualitatively similar findings were obtained from different classification techniques. In addition, results were consistent across changes in PC population size for all spatiotemporal parameters. Moreover, the spatiotemporal spike count representations employed for classification analysis condensed the raw spiking data without the need for intermediary assumptions or dimensionality reduction techniques.

The findings of our study are generally consistent with prior research on the neural processing of tactile inputs and attributes of somatosensory representations in the periphery and brain. Highlighting the role of spatial structure in tactile encoding, studies have shown that representations of different digits in the primary somatosensory cortex (S1) have distinct spatial properties, with larger areas dedicated to the digits that are most sensitive and agile, such as the thumb and index finger [253]. Recent work has also indicated that biomechanical coupling in the hand facilitates a hierarchical organization of tactile information in a gradient from fine (individuated digits) to coarse (whole-hand) spatial representations [2]. Though the correspondence of those findings to representations in the brain remains unclear, they point to the utility of spatial structure in peripheral tactile processing. Our results further underscore the importance of digit-specific spatial structure in peripheral neural representations of tactile interactions.

Prior research has also shown that tactile neurons in the periphery and S1 exhibit a high degree of temporal precision, demonstrating the role of temporal structure in the encoding of touch events[254, 112]. Additionally, our results reflected dependence on the gesture or action being represented, aligning with prior research showing that the involvement of spatial and temporal information in somatosensory processing is task and stimulus-dependent [130, 247, 115]. Furthermore, prior studies have demonstrated that tactile neurons terminating at locations far from the location of skin-object contact can encode information about haptic properties, such as surface roughness, due to

biomechanical coupling in the skin[13, 12, 17]. Those observations support our findings that substantial information is contained in responses of PC populations in palmar areas and highlight the potential significance of biomechanical coupling in tactile information encoding.

It is important to note that several of the aforementioned studies reflect the processing of peripheral spiking inputs from multiple mechanoreceptive pathways within the dorsal column and effects of cortical processing in S1 [255, 256, 257], which were not accounted for in our study. Further analysis is needed to relate our findings to research on the spatiotemporal organization of touch information in early and cortical processing. Nonetheless, our results underline the significance of spatial and temporal organization at multiple scales for the peripheral neural processing of tactile information.

The methodology applied here illustrates how mechanisms of tactile information processing can be investigated through the combination of mechanical measurements and neural simulations. Our findings may inform the development of novel computational models of tactile information encoding by populations of sensory neurons and contribute to the engineering of technologies for haptic feedback or robotic touch sensing [189, 202, 203, 207]. Future studies may incorporate other mechanoreceptive neuron types (SA1 and RA), larger datasets of natural touch interactions, or analysis techniques drawn from other areas of sensory neuroscience [238, 237].

Chapter 5

A Smart Bracelet for Tactile Communication and Interaction

Chapter 3 demonstrated that skin oscillations are biomechanically transmitted across large distances during touch interactions. Chapter 4 further revealed that these oscillations carry information about the touch interactions that produce them. This chapter leverages these insights to develop a wrist-worn device that captures touch-elicited skin oscillations using accelerometers and interprets the encoded tactile information using simple classifiers. Specifically, the device digitally transcribes tactile sign language (TSL) letters performed on the hand, addressing an unmet need for the Deafblind community. The ideas and methods presented here can be leveraged in other haptic devices that aim to turn the skin into a digital input interface for interpreting remote touch interactions. Furthermore, the toolbox presented in Chapter 6 for computationally investigating biomechanical transmission in the upper limb can guide the design of such devices, saving experimental time and resources.

The content of Chapter 5 is adapted from [20], © 2022 IEEE. Reprinted, with permission, from

S. Dinulescu, N. Tummala, G. Reardon, B. Dandu, D. Goetz, S. Topp, Y. Visell, A Smart Bracelet for Tactile Communication and Interaction, *2022 IEEE Haptics Symposium (HAPTICS)*, 2022. DOI: `https://doi.org/10.1109/HAPTICS52432.2022.9765616`.

Tummala's contributions to this research included designing and conceptualizing the research, designing and developing the bracelet, collecting and curating the data, designing and implementing the feature extraction and classification algorithms, analyzing the results, preparing the figures, and writing and editing the manuscript.

Abstract

The sense of touch can convey semantic and emotional information in social or computer-mediated interactions. Touch plays an essential role in communication with individuals affected by multiple sensory loss, many of whom use modes of touch communication that can be broadly described as tactile sign languages. Few technologies exist today to support such interactions. Here, we present a smart bracelet for facilitating tactile communication and interaction. The smart bracelet captures and analyzes vibrations that are elicited in the skin via touch gestures performed on the hand. We demonstrate the utility of this system for supporting communication via the Deafblind Manual alphabet, which is a tactile sign language. This smart bracelet can classify signed letters with greater than 90 % per-letter accuracy. These results show how existing modes of tactile communication can be integrated with information technologies. This work may furnish new paradigms for human-computer interaction via self- and interpersonal-touch contact.

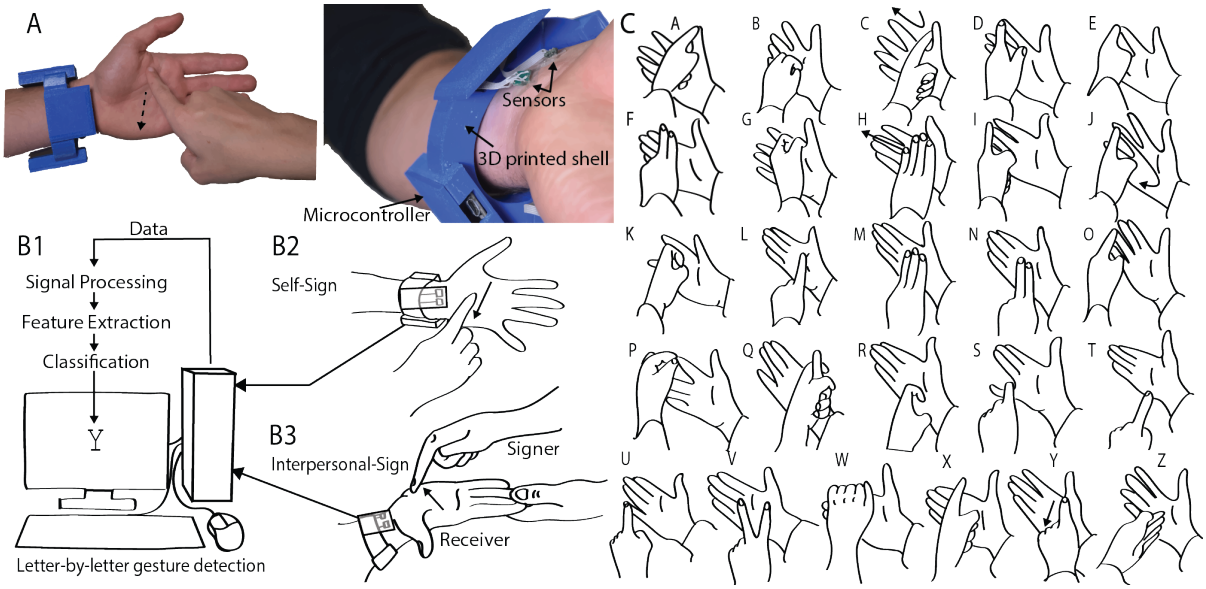

Figure 5.1: A) Wrist-worn acoustic sensing interface to encode and detect touch gestures on the hand. B) System overview and envisioned applications for detection of touch gestures on the skin. B1) Touch signals signed on the palm are transmitted to a PC via serial communication with the microcontroller. The data is processed and features are extracted to be used for classification. B2) Wearable interface enables self-signing on the palm of the hand to encode semantic meaning for note-taking purposes, sending a remote text message via touch, or transcription/record-keeping in the tactile domain. B3) Wearable interface translates interpersonal touch gestures as they are being signed. This could facilitate learning of TSL gestures, transcription of conversations in the tactile domain, and translation of TSL in real-time when the wearer is uncertain of the semantic mappings of the alphabet. C) The 26 letters of the Deafblind Manual alphabet.

5.1 Introduction

The skin is a highly expressive medium used for perceiving and interacting with the world, including communication through touch. Indeed, touch interaction can convey significant meaning, intent, and sentiment. The diverse repertoire of touch interactions encountered in everyday settings, including interpersonal touch, contrasts starkly with the limited communicative and expressive range of touch found in most computing systems today. In some interpersonal interactions, including those involving individuals with multiple sensory impairments such as deafblindness, touch is the principal medium

of communication [258, 259, 260]. Several languages, organizations, and educational systems exist to support the needs of individuals with deafblindness, but there exists a lack of accessibility for digital communication, which is crucial to address due to its ubiquity. However, current interaction paradigms primarily lie in the audiovisual domains. New technologies are needed that can enable individuals with all ranges of sensory abilities to engage with information technologies and digital resources.

Here, we present a smart bracelet for supporting tactile communication and interaction (Fig. 5.1A). This system captures vibration signals elicited in the skin by touch contact gestures performed on the hand; these gestures could be initiated by the wearer or by another person. The captured vibrations are analyzed using signal processing and machine learning methods that can recognize, from a designated lexicon, which gestures are performed (Fig. 5.1B1). We demonstrate the ability of this system to capture and classify touch gestures from the Deafblind Manual alphabet (Fig. 5.1C), a tactile sign language (TSL) used by individuals in Australia who are deafblind, in order to support digital tactile communication.

While several researchers have investigated *output* technologies for reproducing TSL [261, 262, 263, 264], the present work is, to the best of the authors' knowledge, the first *input device* specifically directed at supporting digital TSL communication. Such a device could address important unmet needs, such as those of transcribing information conveyed via TSL communications in court proceedings, emergencies, policy forums, scholarly meetings, or moments of personal or historical significance, especially where transcripts might otherwise be unavailable. Our TSL input device enables the letter-by-letter translation of touch gestures performed on the hand. One might, for example, use the palm of one's own hand to enter text, take notes, or send a text message normally requiring a standard phone interface (Fig. 5.1B2). Such a system could assist individuals with limited vision, for whom usage of mobile devices can be challenging.

In other applications, smart bracelets like the one presented here could also support the training of TSL interpreters. When combined with an output device capable of reproducing TSL gestures, such a smart bracelet could provide a means of TSL communication over the internet, including remote TSL interpretation, improving access to such services by many individuals. When combined with computer translation algorithms, such a smart bracelet could also facilitate conversation between individuals who communicate via different languages, including deafblind individuals who may not use the same TSL (Fig. 5.1B3). Indeed, a diverse variety of TSLs are used around the world [263].

5.1.1 Deafblindness and Tactile Communication

Research and development in automatic speech recognition and language processing over the past 50 years has yielded algorithms and systems for capturing, computationally understanding, and interacting with computers via speech. More recently, analogous methods to speech recognition have been used to support computer-based communication by detecting hand poses during visual sign languages, such as American Sign Language [265]. To date, little attention has been given to achieving similar goals in tactile communication, particularly TSLs.

A recent report by the World Federation of the Deafblind indicates that between 0.2 to 2 % of people are impacted by sensory impairment of both vision and hearing. Deafblind individuals use a variety of languages for tactile communication, depending on their region, community, and individual factors, such as the onset and severity of sensory impairment. Many TSLs exist today supporting critical daily activities and social interaction [266]; in addition, many of the TSLs are letter-based semantic touch communication methods. Here, we demonstrate a system for supporting TSL communication, specifically utilizing the Deafblind Manual alphabet, which involves the performance of touch ges-

tures, including tapping, lightly pinching, and sliding on the surface of the hand. Each of the 26 gesture patterns corresponds to a letter in the English alphabet [263] (Fig. 5.1C).

Other technologies for supporting communication by individuals with visual and auditory sensory loss include Braille interfaces, emerging methods for tactile graphic displays, and more commonly available screen-based accessibility features for those with low vision. However, such methods do not support the communication needs of all individuals who are deafblind. More recently, researchers have engineered systems to translate text or speech into tactile patterns [261, 262], including TSL gestures [263, 266, 267]. However, the authors are not aware of any prior efforts to facilitate or develop a computational encoding of tactile input. A system such as the one presented here could support TSL communication by enabling transcription, analysis, or reproduction of TSL interactions.

5.1.2 Capturing Touch Gestures via Vibration Signatures

Touch interactions with the skin elicit vibrations that travel far from the point of contact, encoding information about the contact location and nature of the gesture [1, 58, 2, 17, 59]. This physical process makes it feasible to collect information about tactile interactions using vibration sensors that are positioned remotely from the contact location. Human-computer interaction research has utilized such processes to provide means of computational input via contact with the skin, as in the Skinput device [60]. Many other sensing methods can be used for capturing information from skin contact, including capacitive, electromyography, ultrasound, force, and other sensing techniques [223, 183, 268, 269]. However, the propensity of touch-elicited vibrations to travel great distances in the skin and the efficiency with which such signals can be captured electronically via low-cost, readily available sensors makes this approach particularly attractive for interactive device engineering, especially in settings where it is

preferable to leave the hand unencumbered.

5.1.3 Summary of Contributions

We present a smart wrist wearable for capturing and recognizing touch gestures that occur on the hand during skin-to-skin contact. To inform the design of this smart bracelet, including the number and placement of sensors, we captured the signal profiles of a subset of letters of the Deafblind Manual alphabet with high spatial resolution using a sensor array encompassing the whole hand. By analyzing this data, we identified that even letters that are highly similar to one another in tactile sign contain unique signal profiles, even when measured at locations removed from the gesture contact. Informed by this finding, we designed a compact, wrist-worn device to capture these propagating signals without hindering natural manual movements and tactile interactions. To demonstrate the utility of this system for tactile communication, we illustrate the capacity of our device to classify 26 different touch gestures—in this case, the letters of the Deafblind Manual alphabet. We find that the device can accurately discriminate between different touched contact locations (e.g., digit II, digit V, or palm) and between different types of touch contact (e.g., slides, impulses, pinches, or squeezes). We show using simple, supervised machine learning methods that such a device is able to identify these 26 different gestures with above 90 % accuracy, even when trained on a small dataset.

5.2 Whole-Hand Sensing

5.2.1 Materials and Methods

In a first experiment, we surveyed the whole-hand mechanical responses produced during the signing of a subset of letters from the Deafblind Manual alphabet. We used

two 42-channel, 3-axis accelerometer arrays (Model LI3DSH, ST Microelectronics) [58]. We captured data at a rate of 1300 Hz via a field-programmable gate array (FPGA) based multichannel data acquisition board, with firmware on the FPGA and software on a Windows PC. We affixed each accelerometer in the array to the skin via doubled-sided adhesive, with one array attached to the dorsal side of the hand and the other to the palmar (Fig. 5.2B).

We captured the skin acceleration for 10 trials of 9 letters of the Deafblind Manual alphabet (A, D, E, F, I, M, N, O, U), signed on the palmar side of the hand through interpersonal touch (i.e., one person signs on the hand of another person). Letters were chosen for high frequency of use (i.e., vowels) and letter similarity (i.e., M and N, D and E). Because the palmar surface of the hand was also covered with sensors, we slightly shifted the signed location of M and N to avoid interfering with the sensors. The palm was held facing upwards, with the forearm stabilized against the edge of a table at chest-level to minimize noise from spurious hand movements. The data consisted of ten, 84-channel 3-axis acceleration signals for each letter. The data was de-meaned and bandpass filtered, then compressed to a single axis by computing the magnitude of the vector. We then computed the RMS of the acceleration magnitude.

To determine the spatial distribution of acceleration energy for each gesture class, we compute root mean square (RMS) acceleration over all trials. We interpolated these data using coordinates obtained from an anatomically plausible 3D hand model using squared distance weighting. We analyzed the differences between letters using this data and also computed the mean pairwise absolute correlation (Pearson's r) between the RMS acceleration of all trials and of all letters.

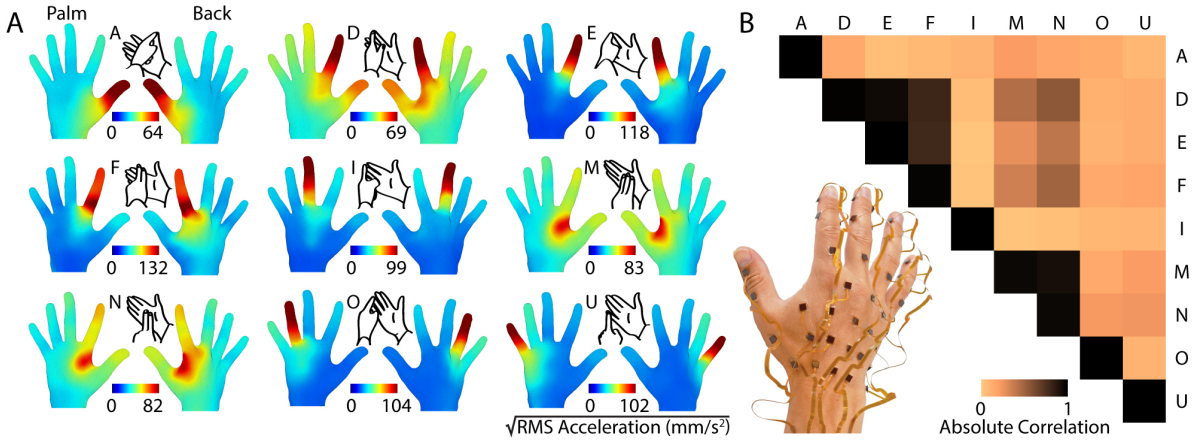

Figure 5.2: A) Measured whole-hand mechanical responses for a subset of the Deafblind Manual alphabet. We found that the contact is not only reflected in skin responses at the touched location, but also that this energy propagated outwards to regions on the skin, on both sides of the hand, far from the point of contact. B) We found that the tactile gestures produced consistent, repeatable patterns of RMS acceleration across the hand (mean absolute correlation > 0.95 within trials of the same gesture), while yielding very low correlations when comparing across trials of different gestures.

5.2.2 Results

Each tactile gesture class yielded distributions of RMS acceleration that reflected the contact location and the nature of the gesture (single touch - A, E, I, O, U and multi-touch - D, F, M, N) (Fig. 5.2A). For example, the peak RMS acceleration of the letter E was localized to the point of contact. Multi-touch gestures tended to deliver high RMS acceleration (relative to the peak RMS acceleration for that gesture) to locations far from the point of contact, reflecting that the contact location on the hand was much larger (2-3 times the size of the contact for single touch gestures). Furthermore, all gestures delivered energy to the wrist; the amount of RMS acceleration delivered at the wrist was a function of the distance from the contact location (e.g., the contact location for E is much further from the wrist than for M/N).

The tactile gestures elicited vibration patterns that were consistent across gesture instances (Fig. 5.2B), and were qualitatively distinct from the other gestures. Consistent

with the observations of the whole-hand patterns (Fig. 5.2A), some gestures produced similar distributions of RMS acceleration and thereby high correlations (i.e. M/N and D/E/F). For the subset of data captured by the ten accelerometers located on the wrist, averaged within-gesture mean absolute correlations of the RMS acceleration (0.94) were substantially larger than across-gesture correlations (0.48). These results suggested that acceleration information captured at the wrist could be used to classify varied tactile gestures.

5.3 Wrist-Worn Interface

Informed by the preceding findings, including the extent to which similar information could be captured via sensors at locations removed from the point of contact with the hand, we designed a smart bracelet using a minimal arrangement of sensors located at the wrist. We evaluated the utility of this device for classifying touch contact gestures performed on the hand, in the form of TSL gestures.

5.3.1 Materials and Methods

Device Design

The device was composed of an ABS shell enclosing two Adafruit Feather M0 WiFi microcontrollers. It employed a total of four 3-axis analog accelerometers (Analog Devices ADXL335) (Fig. 5.1A). Each sensor was adhered to the skin. Pairs of sensors were positioned 25 mm apart on both the palmar and dorsal sides of the wrist (Fig. 5.3A), at locations determined from the preceding experiment. The casing for the electronics was designed to avoid mechanically disturbing the sensing elements. The data was captured at a sampling frequency of 1250 Hz and at a resolution of 12 bits using the onboard ADC

of the microcontroller.

Collection of TSL Data

We collected accelerometer measurements during TSL touch contact in each of two conditions: one in which the signer performed gestures on their own hand (self-sign, or SS, depicted in Fig. 5.1B2) and one in which the signer contacts another person's hand (interpersonal-sign, or IS, depicted in Fig. 5.1B3). The palmar surface of the hand, held outstretched and flat, was facing upwards throughout data collection, with the dorsal side of the forearm stabilized against the edge of a table to minimize disturbance from unintentional limb movements. In both conditions, we recorded 40 trials of each of the 26 letters.

Signal Processing and Feature Extraction

The data for each letter were segmented, lowpass filtered at 250 Hz, and compressed from 3 axes to 1 axis using principal component analysis (PCA). After compression, the data for each trial was normalized independently,

$$y_{c,n} = \frac{y_{c,n}}{\max_{\{c,n\}} |y_{c,n}|}, \tag{5.1}$$

where n is the sample number and c is the channel number. This preserved the inter-channel differences between accelerometers, while also reducing inter-trial variability of the same gesture and improving the consistency of the feature estimates across gestures.

For every trial, we computed time-domain, frequency-domain, and spectro-temporal features for all 4 channels of each analyzed segment, yielding 96 features per trial. The

time-domain features were peak-to-peak amplitude

$$PTP_c = |\max_n y_{c,n} - \min_n y_{c,n}| \tag{5.2}$$

and mean absolute deviation

$$MAD_c = \frac{1}{N}\sum_{n=1}^{N} |y_{c,n} - \bar{y}_c|, \tag{5.3}$$

where $\bar{y}_c$ is the mean of signal $y_{c,n}$. This yielded a total of 8 time-domain features per segment.

For the second set of features, we computed the Discrete Fourier Transform (DFT) of each of the normalized signals, $Y_{c,k} = \mathcal{F}\{y_{c,n}\}$, where $\mathcal{F}$ is the DFT. From the frequency-domain representation of the signal, we computed the spectral centroid

$$SC_c = \frac{\sum_{k=1}^{N} f_k |Y_{c,k}|}{\sum_{k=1}^{N} |Y_{c,k}|}, \tag{5.4}$$

where f_k is the center frequency of bin k and $|Y_{c,k}|$ is the magnitude of bin k for channel c. In addition, we computed the center frequency of the DFT bin with the largest magnitude for each channel c,

$$F_c = f_{k^*} \text{ s.t. } k^* = \arg\max_k |Y_{c,k}|. \tag{5.5}$$

We computed the mean and standard deviation of the DFT bins over a 50 Hz bandwidth. Let the bandwidth $b_i \in \{[0\ 50], [50\ 100], [100\ 150], [150\ 200], [200\ 250]\}$ for $i = 1, ..., 5$. We associate the set of bins K_i whose center frequencies lie within bandwidth b_i and compute:

$$\mu_{c,b_i} = \frac{1}{|K_i|}\sum_{k \in K_i} |Y_{c,k}| \quad , \tag{5.6}$$

$$\sigma_{c,b_i} = \sqrt{\frac{1}{|K_i|}\sum_{k\in K_i}(|Y_{c,k}| - \mu_{c,b_i})^2}, \tag{5.7}$$

where $|K_i|$ is the size of set K_i. This produced 40 features (2 measures $\times$ 5 bandwidths $\times$ 4 channels), for a total of 48 frequency-domain features.

Finally, we composed a set of spectro-temporal features to capture temporal variations in the spectral envelope of the signal. We computed the Short-Time Fourier Transform (STFT) of the signals (window size $K = 256$ samples, 50 % overlap, Hanning window), yielding a matrix of Fourier coefficients ($M \times K$) for each channel c where each of the M rows is the DFT of the signal over different times. We computed the mean and standard deviation of the measure μ_{c,b_i} (see Eq. 5.6) for each row of the Fourier matrix. Let $\mu_{c,b_i,m}$ be the mean of bandwidth b_i for channel c for row m. We compute

$$\mu_{c,b_i}^{STFT} = \frac{1}{M}\sum_{m=1}^{M}\mu_{c,b_i,m} \quad , \tag{5.8}$$

$$\sigma_{c,b_i}^{STFT} = \sqrt{\frac{1}{M}\sum_{m=1}^{M}(\mu_{c,b_i,m} - \mu_{c,b_i}^{STFT})^2}. \tag{5.9}$$

This yielded another set of 40 features (2 measures $\times$ 5 bandwidths $\times$ 4 channels). All features (temporal, frequency, and spectro-temporal) were concatenated to form a 96-dimensional vector, used to train the machine learning model and classify the 26 different tactile gestures.

TSL Classification

To distinguish the 26 letters of the Deafblind Manual alphabet via our smart bracelet, we pass computed features into three common supervised machine learning classification models: a support vector machine with a linear kernel (SVM), logistic regression with PCA (LR), and a random forest model (RF). To minimize bias during training and

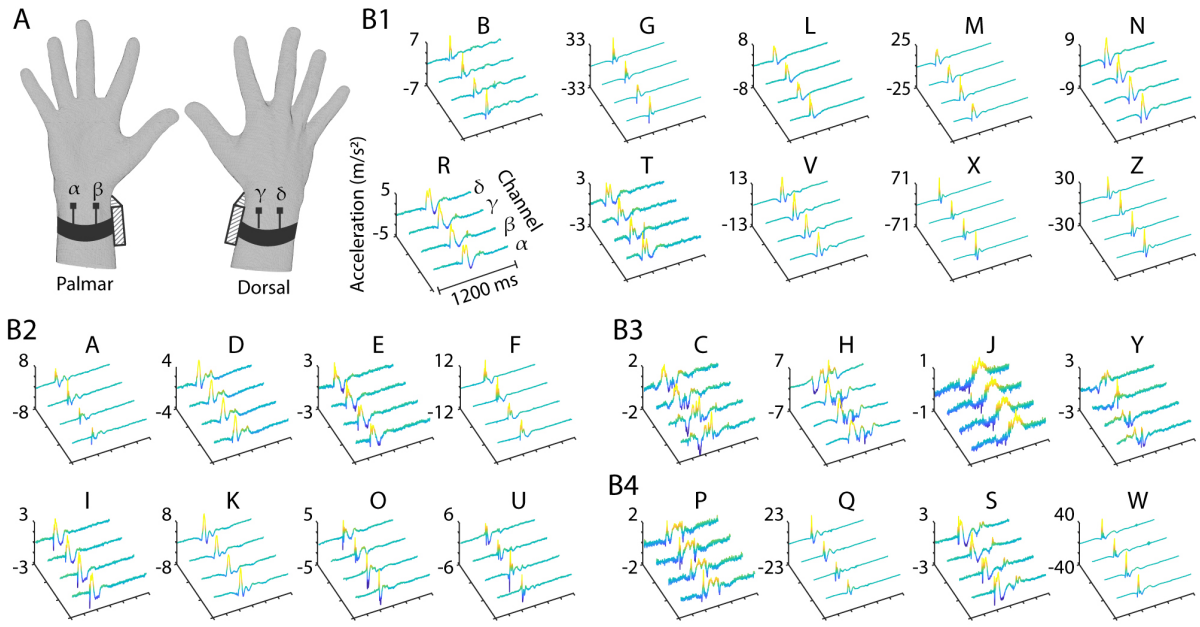

Figure 5.3: A) Wrist-wearable device using four accelerometers affixed to the skin to capture mechanical vibrations produced during tactile fingerspelling. B) Measured accelerometer signals produced during a single trial of each letter of Deafblind Manual alphabet. Palm tap and finger tap gestures (B1 and B2, respectively) produced transients that rapidly decayed. Finger taps tended to deliver less energy to the wrist when compared to palm taps, reflecting the difference in distance between the point of contact and the sensor. Sliding or pinching/grabbing gestures (B3 and B4, respectively) produced signals that tended to decay at a much slower rate on the skin, reflecting that the gesture occurs over a longer time scale than the tap gestures.

classification, we employed a 10-fold cross-validation procedure with a 90-10 train-test split. During each classification run, we computed the mean and variance of each feature in the training data and used these sample moments to whiten both the training and testing data. We performed classification for each mechanical dataset separately (SS and IS conditions, 40 trials per letter) and on both datasets (combined condition, 80 trials per letter).

5.3.2 Results and Discussion

Mechanical Signal Profiles

We found that the measured signals (Fig. 5.3B) yielded noticeably different time-domain acceleration responses, which became more prominent when we grouped the gestures by palm taps (Fig. 5.3B1), finger taps (Fig. 5.3B2), slides (Fig. 5.3B3), and pinches/grabs (Fig. 5.3B4). We found that tapping gestures yielded transient signals that decayed rapidly, while slides and pinches/grabs decayed at much slower rates in the skin. This likely reflects the variation in contact conditions between the gestures, for which slides and pinches/grabs occur at much longer time scales. We found that finger taps delivered less energy to the wrist when compared to palm taps, reflecting that the properties of the skin, which is a highly damped medium, play a role in encoding the distance from the contact location to the wrist, thereby differentiating the measured tactile gestures. Finally, we found that sliding gestures, regardless of contact location, tended to deliver less energy to the wrist, but that this energy was nonetheless measurable and informative.

TSL Classification

When utilizing data from all four sensors, the SVM classifier consistently outperformed the RF and LR classifiers in the SS and IS conditions, with average accuracies greater than 93 % across cross-validation folds; in the combined condition, the RF classifier slightly outperformed the others at close to 90 % average accuracy across folds (Table 5.1). High performance using SVM is promising for real-time applications, as a trained SVM model can easily be implemented on a micro-controller without the need for additional computational power. In the following analysis, we focus on the performance of the SVM model.

	Classifier		
Dataset	SVM	RF	LR
SS	93.9	88.7	90.6
IS	93.7	92.2	91.0
Combined	86.3	89.4	76.1

Table 5.1: Average Classification Accuracy (%) Across Datasets and Models for 4-Sensor Configuration

We further analyzed classification performance using different subsets of sensor channels (Fig. 5.3A) to determine the minimal number of sensing element required for robust classification. The subsets considered include all four channels ($\alpha, \beta, \gamma, \delta$), two channels on the palmar side of the wrist (α, β), two channels on the dorsal side of the wrist (γ, δ), one channel on the palmar side of the wrist (α), and one channel on the dorsal side of the wrist (γ). Table 5.2 summarizes the average classification accuracies across cross-validation folds for the SS, IS, and combined datasets. The use of all four channels yields the highest classification accuracies, but the employment of just two sensors maintains robust performance (above 85 % in the single subject conditions), indicating that they are sufficient for detecting various sets of tactile gestures. Mounting the sensors on the palmar or dorsal side of the wrist does not significantly change classification accuracies. On the other hand, classification accuracy drops significantly when using only one sensor, indicating that inter-channel differences encode relevant classification information that cannot be discarded. Close inspection of the signals shown in Fig. 5.3B shows differences in the phase and shape of signals between channels, most evident in the sliding gestures.

We found that the most commonly misclassified letters were L and N, which is expected due to the similarity of the tactile gestures; N is signed with two fingers in the center of the palm whereas L is signed with one finger in the same location (Fig. 5.4). Additionally, R and T are commonly mislabeled, as they are both taps occuring near the same palmar location: T with one finger and R with two fingers. Other commonly mis-

	Sensor Configuration					
Dataset	$\alpha, \beta, \gamma, \delta$	α, β	γ, δ	α, γ	α	γ
SS	93.9	86.5	86.8	87.1	76.3	73.8
IS	93.7	88.3	85.4	87.1	75.0	75.4
Combined	86.3	76.8	75.6	78.4	61.6	64.3

Table 5.2: Average Classification Accuracy (%) Across Datasets and Sensor Configurations for SVM Model

classified letter pairs include G and X, and W and Z. The former are gestures performed with the signer's whole hand, producing high acceleration signals at the palm; the latter produce similar high energy signals, but occur at different locations on the hand.

We also examined classification accuracy within each gesture grouping shown in Fig. 5.3B (i.e. palm taps, finger taps, slides, and pinches/grabs) for the combined dataset in the four channel configuration, averaged across cross-validation folds. Sliding gestures are classified with the highest accuracy (92.8 %), likely because they produce the most distinct mechanical signals. Finger taps are also accurately classified (90.8 % accuracy) and are generally only misclassified as other finger taps, likely because the captured signals often possess similar magnitudes and temporal profiles. Similarly, palm taps (81.1 % accuracy) are accurately recognized and are typically only misclassified as other palm taps. This is expected when considering the similarity between many of the palm taps; for example, L, M, N, and V are all signed in the middle of the palm but with different finger placements. Finally, pinch or grab gestures (83.8 % accuracy) are somewhat more likely to be misclassified as other types of gestures due to their heterogeneous nature.

Regardless of the classifier, dataset, or sensor configuration, we observe accuracies above 60 %, which is significantly higher than chance (3.9 % for 26 classes). In the majority of SS and IS conditions, accuracies are above 90 % when using four sensors, regardless of classifier used. This indicates that accuracies approaching 100 % can likely be achieved via standard techniques such as lexicon-based models that are widely used

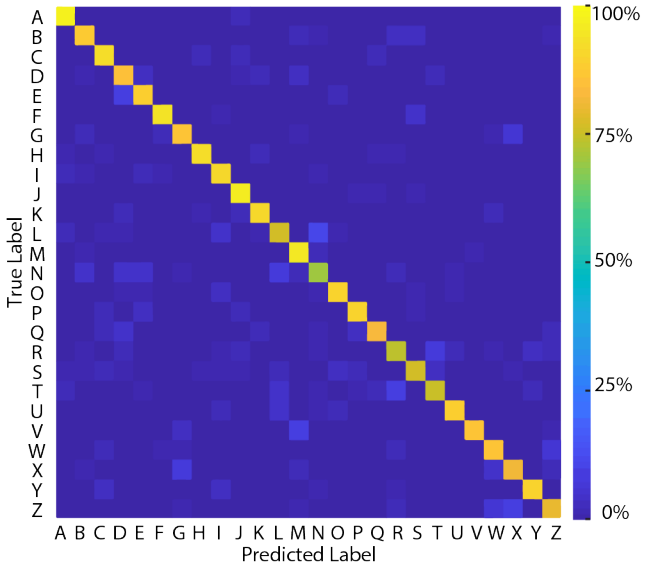

Figure 5.4: Confusion matrix for the linear SVM Classifier on the combined dataset, with per-letter accuracies along the diagonal. On the off-diagonal, type I (false positives) read column-wise and type II (false negatives) read row-wise. Commonly misclassified letter pairs can often be grouped into the subsets introduced in Fig. 5.3. For example. {E,D} are both taps on digit II, and {G, X, Z}, {L, N}, and {R, T} are all taps on the palm.

in natural language processing and automatic speech recognition. Further improvements might also be achieved through the use of state-of-the-art multi-layer neural network classifiers.

5.4 Conclusion

We present a smart bracelet system that transforms the skin into a touch gesture input interface. The bracelet can classify touch gestures of the Deafblind Manual alphabet, via integrated wrist-worn sensors, with significantly higher-than-chance accuracy. Our approach demonstrates the success of minimal accelerometer-based sensing that leaves the hand unencumbered for manual interactions and movements. Measurements from a whole-hand sensing array were used in an initial exploration to identify a subset of four

sensors that are able to capture enough salient information in a touch gesture, thus reducing cost and complexity. We demonstrated the utility of this device for supporting tactile communication via TSL. We present analyses of an experiment in which we captured and accurately classified signal profiles for all 26 letters of the Deafblind Manual alphabet, demonstrating promising uses of such systems for supporting tactile communication.

The smart bracelet can be used for input via tactile gestures performed on the hand of the user by the user, which could be useful for note-taking, transcription, or textual communication. Such a device could support interpersonal tactile communication by individuals who prefer using touch over other modalities, in addition to encoding touch in the digital domain. These findings may also enhance the utility of output devices for tactile communication. Utilizing input and output devices in conjunction could support communication between two or more individuals, including people who may communicate via different TSLs.

While we have demonstrated the capability to accurately classify the 26 gestures of the Deafblind Manual alphabet, more remains to generalize features for classification of larger mechanical datasets consisting of various TSL signers, receivers, and alphabets. Further investigation into individual differences between subjects, such as hand size, signing speeds, and emotion (i.e. happy, angry) conveyed through TSL, will be experimentally investigated.

We further envision supporting real-time classification of TSL, where signing occurs as fast as five letters per second [263]. In these cases, intentional or accidental movements of the hand (such as finger motion from a previously performed tactile gesture) must not interfere with signals captured from the sensors. Thus, further data capture and signal processing methods will be explored, examples of which include capturing data from two devices worn on both the signer's and receiver's wrist, or capturing false positive dataset examples (such as muscle contractions, finger twitches, etc.) to help identify gestural

noise versus salient gesture data. We will additionally explore multi-layer classification and feature optimization by additional meta-analysis of similarities and differences between tactile signals in a gesture set, as well as natural language processing as previously applied in speech technologies. Such advancements are expected to improve accuracy and robustness, aiding applications in natural communication. This system holds promise for supporting tactile communication, including scenarios where it is paired with a haptic communication output device, to address communication needs of individuals who are deafblind.

Chapter 6

SkinSource: A Data-Driven Toolbox for Predicting Touch-Elicited Vibrations in the Upper Limb

This chapter presents a free-to-use software toolbox for predicting spatiotemporal patterns of skin oscillations across the entire upper limb elicited by tactile stimuli applied at one or more locations on the hand. The underlying dataset consists of impulse responses measured with an array of accelerometers placed on the upper limbs of four different individuals. Similar to Chapter 3, the toolbox utilizes the measured impulse responses to predict skin oscillations elicited by arbitrary inputs in software. This work enables researchers or designers to computationally investigate the design of wearable haptic sensing or feedback devices, making measurement-informed design processes like that used in Chapter 5 more efficient. This chapter also reports experiments that validate the accuracy of the linear systems method used to predict the skin oscillations produced by any user-designed tactile stimuli, lending support to the methodology used in Chapter 3.

The content of Chapter 6 is adapted from [21], © 2024 IEEE. Reproduced, with permission, from

N. Tummala*, G. Reardon*, S. Fani, D. Goetz, M. Bianchi, Y. Visell, SkinSource: A Data-Driven Toolbox for Predicting Touch-Elicited Vibrations in the Upper Limb. *2024 IEEE Haptics Symposium (HAPTICS)*, 2024. DOI: https://doi.org/10.1109/HAPTICS59260.2024.10520852
(*contributed equally)

Abstract

Vibrations transmitted throughout the hand and arm during touch contact play a central role in haptic science and engineering but are challenging to model or experimentally characterize. Here, we present SkinSource, a data-driven toolbox for predicting skin vibrations across the upper limb in response to user-specified input forces. The toolbox leverages impulse response measurements that encode the physics of vibration transmission across the hands and arms of four participants and provides software tools for analyzing the predicted skin responses. We show that the SkinSource predictions closely match experimental measurements and confirm the underlying assumption of linear vibration transmission in the skin. We also demonstrate through several usage examples how SkinSource can act as a versatile computational platform for haptic research applications, such as characterizing vibrotactile transmission in the skin, engineering haptic interfaces, and investigating touch perception.

6.1 Introduction

Manual touch interactions and haptic feedback supplied to the hand generate vibrations that are transmitted throughout the hand and arm [12, 1]. These evoked vibrations encode perceptually relevant information about the contact events that elicit them [17, 55, 2]. Characterizing this mechanical process has played an important role in understanding the interplay between biomechanics and neural encoding in touch perception [48, 174, 13, 67, 14, 149, 61, 16]. Investigations of vibration transmission in the upper limb have also informed the engineering of vibrotactile feedback techniques [4, 227] and inspired new approaches for engineering robotic or prosthetic sensing systems [206, 270, 208]. Moreover, touch-elicited skin vibrations have been leveraged in the design of wearable sensing and haptic feedback devices [222, 60, 271, 58, 20]. Outside of haptic technology, vibration transmission in the upper limb has been characterized to inform the development of occupational safety standards for power tool usage [185] and diagnostic tests for skin diseases [38].

However, vibration transmission in the upper limb is a complex function of the anatomical structure and tissue biomechanics of the hand and arm [37, 13, 4, 56, 32]. It has thus proven challenging to accurately predict the whole-limb response from numerical modeling. Such models have been most effective at characterizing the mechanical response of localized tissues near the stimulation site [272, 37] or capturing the dynamics of the musculoskeletal system [273] rather than predicting vibration transmission across the entire limb. Further, due to the widespread transmission of touch-elicited vibrations throughout the hand and arm [12, 1], experimental measurements require time-consuming procedures and specialized equipment [13, 38, 2, 4]. As a result, measurements are often limited in scope, employing a single stimulation location and application-specific test signals.

Here, we introduce SkinSource, a data-driven, open-source toolbox for accurately predicting skin vibrations across the upper limb in response to input forces applied at any of 20 distinct locations on the hand. The toolbox integrates a vibrometry dataset containing impulse response measurements captured at 72 locations on the hands and arms of four participants and exploits the linearity of vibration transmission in the skin to predict the mechanical response of the upper limb. SkinSource also includes MATLAB tools that enable users to design their own stimuli to apply at one or more hand locations and analyze the predicted skin vibrations in the time or frequency domains.

The functionalities provided by SkinSource are intended to aid haptics research, engineering, and design, like other recently released haptics datasets and tools [274, 67]. SkinSource can serve researchers in sensory neuroscience and perception by providing a means for investigating the mechanical basis of touch perception. The toolbox may also aid engineers in designing haptic interfaces, wearable sensors, or assistive devices while reducing the need for laboratory experiments (Fig. 6.1A). In the remainder of the paper, we provide an overview of the toolbox and potential use cases (Section 5.2), describe the data collection (Section 5.3), report results validating the toolbox predictions (Section 5.4), and confirm the linearity of vibration transmission in the upper limb (Section 5.5).

6.2 The SkinSource Toolbox

SkinSource contains a vibrometry dataset (Sec. 5.2.1) and accompanying MATLAB software tools that allow users to specify time-varying force inputs at any of 20 locations on the hand. Skin vibrations are predicted at 72 locations on four upper limb models via convolution with impulse responses measured from four participants (Sec. 5.2.2). These predictions are returned to users as an array of 3-axis skin accelerations. SkinSource also provides data exploration tools that allow users to project vibrations onto selected axes,

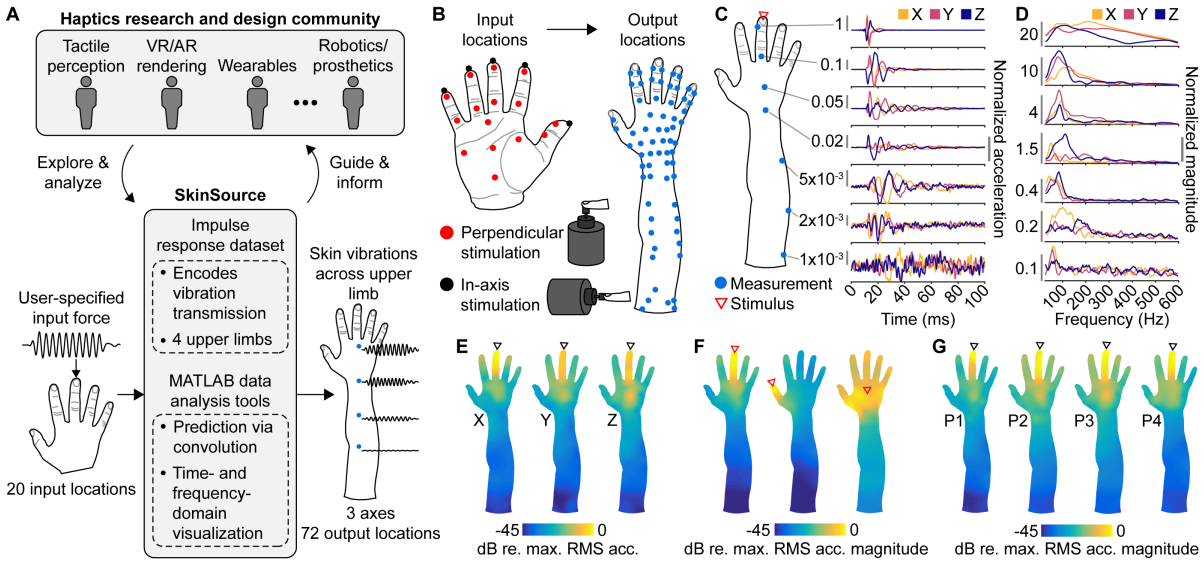

Figure 6.1: **Overview of SkinSource and impulse response dataset.** A) Users in the haptics community can utilize SkinSource to explore and analyze vibration transmission in the upper limb and use the outputs to guide and inform research and design applications. B) Force inputs can be supplied at any of 20 locations on the palmar surface of the hand (left) perpendicular to the hand surface (red dots) or in-axis with the digits (black dots). Skin vibrations (accelerations) are predicted at 66 locations on the dorsal surface (and 6 locations on the volar surface, not pictured) of the upper limb (right). C) Normalized 3-axis impulse responses at selected output locations (blue dots) on the upper limb of Participant 4 (P4) for an input applied at the tip of digit III (perpendicular). D) Normalized 3-axis frequency magnitude spectra of the impulse responses shown in C. E) Normalized RMS of 3-axis impulse responses across each measurement axis for an input at the tip of digit III (in-axis) of P3. F) Normalized RMS of impulse response acceleration magnitudes for inputs applied at 3 locations (red arrows, all perpendicular) on the hand of P1. G) Normalized RMS of impulse response acceleration magnitudes for an input at the tip of digit III (perpendicular) on the hands of all participants.

compute frequency-domain spectra, and visualize vibrations on a 2D upper limb model. The results shown in Fig. 6.1 and Fig. 6.2 were generated using SkinSource and demonstrate the versatility of the toolbox for applications in characterizing the mechanical response of the upper limb, designing haptic devices, and investigating touch perception. SkinSource can be found at `https://doi.org/10.5281/zenodo.10547601` along with documentation and usage examples.

6.2.1 Impulse Response Dataset

SkinSource integrates a dataset of more than 5000 impulse responses obtained from 3-axis vibrometry measurements of skin acceleration on the upper limbs of four participants (sample rate: 1300 Hz), as described in detail in Section 5.3. The impulse responses encode the physics of vibration transmission from 20 input locations on the palmar surface of the hand to 72 output locations on the hand and arm (66 dorsal, 6 volar; Fig. 6.1B). The measured impulse responses capture previously reported features of vibration transmission in the skin. These features include frequency-dependent transmission speed (phase velocity) [13], demonstrated by the temporal spreading of a wave packet with increasing transmission distance (Fig. 6.1C), and frequency-dependent attenuation, with lower frequency vibrations generally exhibiting less attenuation [4] (Fig. 6.1D). Moreover, the impulse responses demonstrate that measurable mechanical energy is transmitted to the wrist and forearm, also reflecting findings from prior work [12, 17, 20]. The dataset enables investigations of skin vibrations measured in different axes (Fig. 6.1E) and analyses of vibration transmission for different input locations (Fig. 6.1F). Additionally, the dataset allows users to investigate the differences in vibration transmission across different upper limbs by providing data collected from four participants (Fig. 1G; see Section 5.3).

6.2.2 Toolbox Implementation

To predict skin vibrations in the upper limb elicited by a user-specified input stimulus, SkinSource leverages the measured impulse response dataset. This implementation relies on the assumption that vibration transmission in the skin is approximately linear for some small signal regime and can therefore be described compactly as impulse responses or, equivalently, as frequency domain transfer functions. This assumption of linearity

is validated and discussed in Section 5.5. In this linear regime, vibrations elicited by arbitrary time-varying forces $f_{\mathbf{y}_n}(t)$ applied normal to the skin at location $\mathbf{y}_n$ can be efficiently computed as

$$u^{\alpha}(\mathbf{x},t) = \sum_{n=1}^{N} h^{\alpha}_{\mathbf{y}_n}(\mathbf{x},t) * f_{\mathbf{y}_n}(t), \tag{6.1}$$

where $*$ is convolution in time, N is the number of input locations, $u^{\alpha}(\mathbf{x},t)$ is the time-varying skin vibration in direction α at location $\mathbf{x}$, and $h^{\alpha}_{\mathbf{y}_n}(\mathbf{x},t)$ is the time-varying skin vibration in direction α at location $\mathbf{x}$ elicited by a unit impulsive force applied normal to the skin at location $\mathbf{y}_n$ (the impulse response). Measuring the impulse responses eliminates the need for multiple experimental measurements of skin vibrations elicited by different input stimuli of interest. Instead, resulting vibration responses can be predicted efficiently *in silico* (< 100 ms computation time).

SkinSource provides four different data-driven models built on measurements obtained on the upper limbs of four different participants. Although anatomical features and therefore distances between accelerometers varied across participants (hand lengths: 165 to 185 mm), input and output locations were mapped to a single 2D dorsal hand surface for visualization and analysis purposes. Measured skin vibrations were extrapolated to points on the boundary of the 2D hand surface using weights proportional to the distance of the two accelerometers closest to each boundary point. Skin vibrations at intermediate locations on the 2D hand surface were then determined using natural neighbor interpolation. SkinSource also integrates a number of MATLAB software tools to aid users in analyzing the predicted skin vibrations, including projecting the 3-axis vibrations onto specified axes (e.g., the tangential or principle component axis) and computing frequency domain spectra.

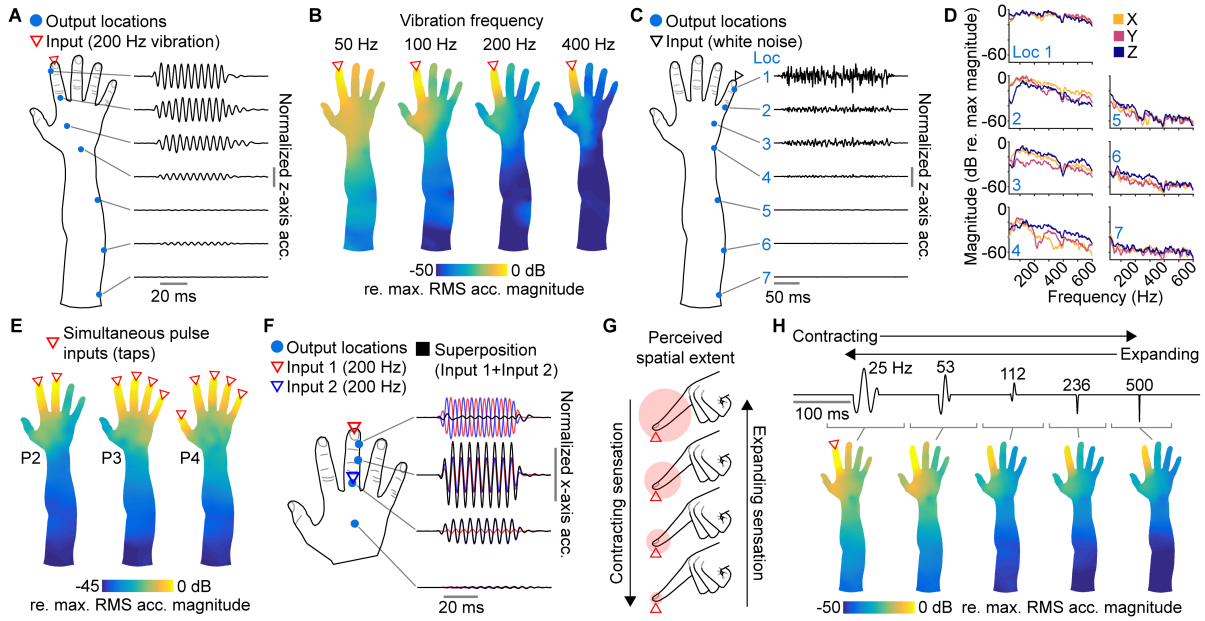

Figure 6.2: **SkinSource usage examples.** A) Normalized z-axis skin acceleration at selected locations (blue dots) on the upper limb of Participant 1 (P1) elicited by a 200 Hz sinusoidal vibration applied at the tip of digit II (perpendicular). B) Normalized RMS of skin acceleration magnitudes for 4 input sinusoids of varying frequencies (50, 100, 200, 400 Hz) applied to the tip of digit II (perpendicular) of P1. C) Normalized z-axis skin acceleration at selected locations (blue dots) on the upper limb of P2 elicited by a white noise stimulus applied at the tip of digit V (in-axis). D) Normalized 3-axis frequency spectrum magnitudes of skin accelerations shown in C. E) Normalized RMS of skin acceleration magnitudes elicited by the simultaneous application of pulses at the locations marked by red arrows (perpendicular) across three different participants (P2, P3, and P4). F) Normalized x-axis skin acceleration at selected locations (blue dots) on the hand of P3 elicited by a 200 Hz vibration applied at the tip of digit III (red, perpendicular), a 200 Hz vibration applied at the base of digit III (blue, perpendicular), and the superposition of both input vibrations (black). G) Perceived spatial extent of vibrations provided to the tip of digit II in a haptic illusion created by [4] that elicits a spatially contracting (top to bottom) or expanding (bottom to top) sensation using a single actuator. H) Normalized RMS of skin acceleration magnitudes within 5 consecutive time windows elicited by the stimulus that produces the illusion in G, which is a train of wavelets varying in frequency (top, black trace) applied at the tip of digit II (perpendicular) of P4.

6.2.3 Toolbox Usage and Examples

In this section, we briefly explore several potential applications of SkinSource.

Designing Haptic Devices

SkinSource can facilitate the haptic device design process by predicting skin vibrations elicited by mechanical stimuli. For example, users can input sinusoidal vibrations of various frequencies to the hand (Fig. 6.2A) and analyze properties of vibration transmission in the upper limb, such as frequency-dependent attenuation (Fig. 6.2B). Such observations of vibration transmission have led to the establishment of device guidelines like the optimal configuration of vibrotactile stimulators in haptic feedback displays [59, 225] and to the engineering of haptic sensing devices that leverage touch-elicited vibrations [222, 60, 271, 58, 20].

Understanding Tactile Perception

Prior studies of vibration transmission in the skin have demonstrated that texture-elicited vibrations play a role in human tactile perception [12, 55]. To aid in such investigations in the future, SkinSource can be used to examine skin vibrations elicited during texture exploration. For example, users can predict the skin vibrations elicited by a texture approximated as white Gaussian noise during transmission across the entire upper limb in both the time (Fig. 6.2C) and frequency domains (Fig. 6.2D). SkinSource can also be easily integrated with texture datasets captured during scanning of the fingerpad [275, 55].

Investigating Complex Manual Interactions

Many manual touch interactions, such as grasping a cup or typing on a keyboard, involve multiple points of touch contact on the hand. With SkinSource, users can investigate vibrations elicited by interactions that can be approximated as the superposition of force inputs at multiple hand locations. For example, pulse inputs applied simultaneously

at several fingertips (Fig. 6.2E) closely resemble whole-hand vibrometry measurements collected during multi-finger tapping gestures [1]. Moreover, the exploration of superimposed inputs can produce interesting results, such as constructive and destructive interference at various regions on the skin after the application of simultaneous vibrations at multiple locations (Fig. 6.2F, top trace: destructive, second-to-top trace: constructive). Similar investigations enabled by SkinSource could be used to engineer multi-input stimuli for focusing vibrations in the skin [227] or to optimize actuator locations in virtual reality gloves [276].

Engineering Tactile Feedback Techniques

Examining vibration transmission in the skin can guide the creation of new tactile feedback techniques. This process is clearly exemplified in [4], where the authors observed frequency-dependent attenuation of skin vibrations in their mechanical measurements and used this observation to engineer a novel perceptual effect of spatial expansion or contraction using only a single actuator (Fig. 6.2G). This iterative design process could be accelerated with SkinSource, which allows users to rapidly explore skin vibrations elicited by different test signals. For example, users can observe frequency-dependent attenuation in the skin by inputting sinusoidal vibrations (Fig. 6.2B). They can then design and test novel vibrotactile stimuli exploiting this phenomenon, such as the expanding/contracting stimulus designed in [4]. The spatial extent of the skin vibrations predicted by SkinSource in response to this stimulus do, in fact, contract and expand (Fig. 6.2H), indicating a promising perceptual effect for users to later test. The iterative design process described in this section can also be employed for many other applications, including the design of wearable and robotic sensing technology.

6.3 Impulse Response Dataset Capture

6.3.1 Experimental Setup

Skin accelerations were measured using custom accelerometer arrays [1] placed on the right hands and arms of four participants (two female, two male, ages in years: mean 27.5 ± 3.1 SD; Fig. 6.3A). The experimental protocol was approved by the Human Subjects Committee at UC Santa Barbara and complied with the Declaration of Helsinki. All participants gave their written and informed consent. Each of the 72 accelerometers in the array was adhered to the skin using double-sided adhesive (66 on the dorsal surface, 6 on the volar surface). Though hand sizes differed (165 to 185 mm), the relative anatomical positioning of each accelerometer was preserved across participants. The stimuli were applied with an electromagnetic actuator (Mini Shaker Type 4810, Brüel & Kjær, Denmark) at 20 input locations on the volar surface of the hand either perpendicular to the volar hand surface (Fig. 6.3B) or in-axis with the digits (Fig. 6.3C). The actuator probe tip (square profile, 49 mm^2 contact area) was attached to the skin with double-sided adhesive to ensure that there was no decoupling during the application of the stimuli. Each participant was seated with their hand and forearm placed palm-down in a comfortable resting position on a pneumatically-isolated table. The volar side of the hand and forearm were supported by foam in all areas except where the stimulus was applied. The upper limb was otherwise unconstrained. Participants were instructed to keep their hands relaxed throughout the experiment without applying force to the probe tip beyond that applied through their resting posture. Thus, the actuator preload was minimal, and the probe tip was primarily secured in place via the double-sided adhesive.

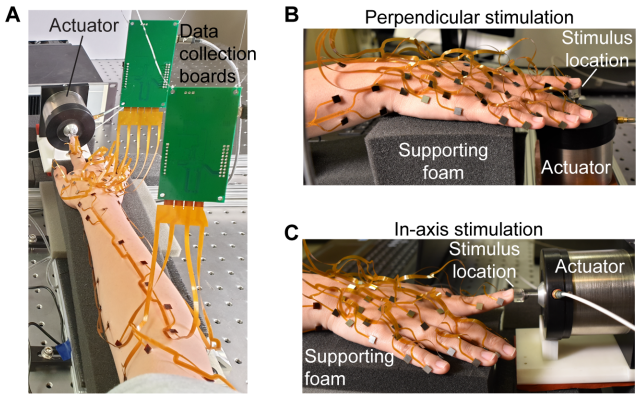

Figure 6.3: **Impulse response dataset capture.** A) Data was captured using an accelerometer array on the upper limb, which was supported by foam but otherwise unconstrained. Stimuli were delivered both B) perpendicular to the palmar surface of the hand and C) in-axis with the digits.

6.3.2 Data Collection and Processing

Skin accelerations were collected in 3 axes at a sample rate of 1300 Hz. The z-axis was normal to the skin surface, while the x- and y-axes were tangential to the skin surface. However, the x- and y-axes were not oriented with respect to consistent global axes across accelerometers. Input stimuli were rectangular impulses, which were lowpass filtered (passband: 600 Hz) to satisfy the Nyquist sampling criterion. The full width at half maximum of the impulse input was 1 ms, and the average peak input acceleration at the actuator probe tip was 22.9 m/s^2 across contact conditions. The measured skin accelerations were averaged across 8 trials and de-meaned to produce the impulse responses, which were 400 ms in duration. Input stimuli were measured at the actuator probe tip for P1 and averaged across 7 trials. These input signals are provided with the toolbox to enable compensation of the actuator response in the impulse response measurements if desired. Data collection took approximately 2 hours per participant.

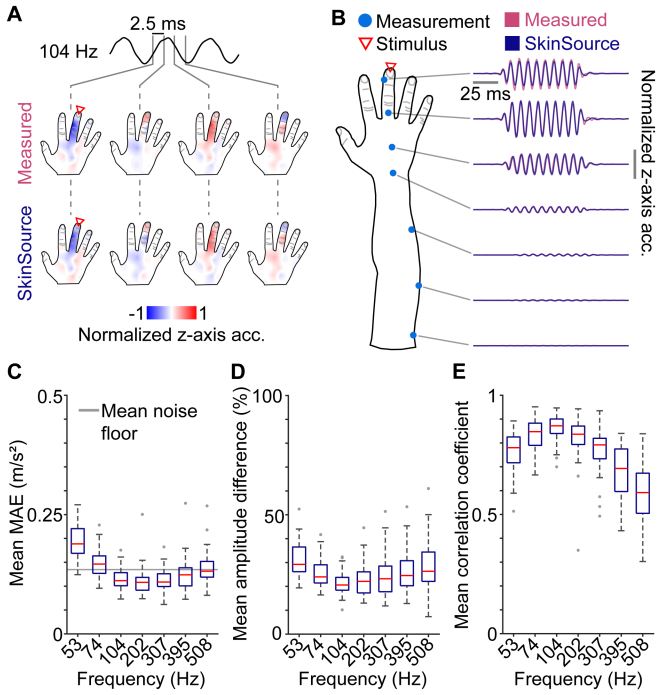

Figure 6.4: **Comparison of measurements and SkinSource predictions.** A) Normalized z-axis skin accelerations from measurements (top) and SkinSource predictions (bottom) at consecutive time steps for a 104 Hz sinusoid applied at the tip of digit III (perpendicular) of Participant 1 (P1). Top trace shows the measured z-axis skin acceleration at the measurement location closest to the input location. B) Normalized z-axis skin accelerations at selected points (left, blue dots) on the upper limb of P1 from measurements (pink) and SkinSource predictions (dark blue) for a 104 Hz sinusoid applied at the tip of digit III (perpendicular). C) Mean MAE (mean absolute error), D) mean percent amplitude difference, and E) mean Pearson correlation coefficient between measurements and SkinSource predictions across input sinusoid frequency. In C-E, the mean is taken across all measurement locations and axes, then summarized as box plots across all participants and input locations for each frequency. Box limits: lower and upper quartiles; red center lines: median; whiskers: 1.5x interquartile range; gray dots: outliers.

6.4 Evaluating SkinSource Predictions

SkinSource employs the impulse response dataset and computational methods described in the prior sections to predict skin vibrations evoked in the upper limb for the conditions and input forces specified by the user. To evaluate the accuracy of this methodology, we compared SkinSource predictions to experimental measurements of skin

vibrations elicited by sinusoidal inputs (7 sinusoids spaced on a logarithmic scale from 53 to 508 Hz, 10 cycles, averaged across 5 trials). The experimental measurement procedure was identical to that used to measure the impulse responses (Section 5.3). We computed the SkinSource predictions (Eq. 6.1) and assessed their similarity to the experimental measurements (Fig. 6.4A, B). To compare results across these two conditions, data was normalized by the average RMS signal amplitude within each condition. Skin vibrations were only compared at locations where the vibration amplitudes were at least twice the average measurement noise floor.

We analyzed errors averaged across measurement locations and axes for all participants and input frequencies. The errors quantified phase and amplitude differences between the SkinSource predictions and the measurements. The mean absolute error (MAE), which captured both phase and amplitude differences, was comparable to the average noise floor of the measurements (Fig. 6.4C). The median percent amplitude differences, which captured only amplitude errors, remained below 30 % across all frequencies (Fig. 6.4D). Additionally, median Pearson correlation coefficients, which captured only phase differences, were above 0.5 across all frequencies (Fig. 6.4E). Though correlations decreased at higher frequencies, which also led to an increase in MAE, prior work suggests that this may have little effect on perception [277]. Overall, the SkinSource predictions were in qualitative and quantitative agreement with the measurements. The small discrepancies between the two conditions may be due to differences in contact conditions, signal-to-noise ratio (SNR), or time alignment. Notably, measurement collection took approximately 2 hours per participant, while the SkinSource predictions were obtained in less than 5 s, highlighting the utility of SkinSource's data-driven methodology.

6.5 Linearity of Vibration Transmission in the Upper Limb

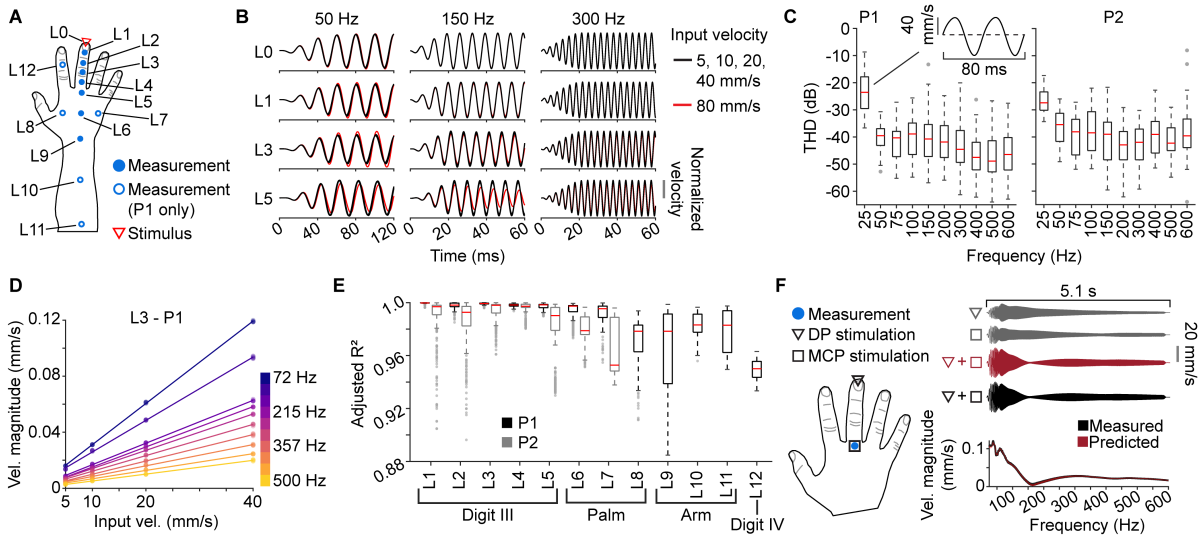

Figure 6.5: **Validation of the linearity of vibration transmission in the upper limb.** A) Skin velocity was measured via laser Doppler vibrometry at selected locations (blue dots, L0-L12) on the dorsal surface of the hands of two participants (P1 and P2) during stimulation on the volar side of the distal phalanx of digit III (red arrow). L0 denotes the measurement location on the actuator probe tip. B) Measured velocity normalized by input velocity at 4 locations (L0, L1, L3, and L5) and 3 frequencies (50, 150, and 300 Hz), with measurements at all input velocities overlaid. Red trace corresponds to highest input velocity (80 mm/s). C) Boxplot of total harmonic distortion (THD) for the set of sinusoidal input signals, aggregated across all measured locations for each stimulus frequency. Shown for P1 (left) and P2 (right). Inset shows unloaded actuator response at 25 Hz. Box limits: lower and upper quartiles; red center lines: median; whiskers: 1.5x interquartile range; gray dots: outliers. D) Linear fits (lines) of input velocity versus measured velocity magnitude for all trials of sine sweep measurements (dots). Shown for P1 at L3 for selected frequency bins (denoted by color). E) Boxplots of adjusted R^2 from linear fits of sine sweep measurement frequency spectra (25-600 Hz for P1, 25-500 Hz for P2, 2 Hz resolution) aggregated across all trials and frequency bins for each measurement location (L1-L12). Box color: participant (P1: black, P2: gray); box limits: lower and upper quartiles; red center lines: median; whiskers: 1.5x interquartile range; gray dots: outliers. F) Predicted (red) versus measured (black) skin velocity at a selected location (blue dot) in the time and frequency domains during simultaneous DP (triangle) and MCP (square) stimulation. Predicted skin velocity is computed as the sum of measurements during DP-only and MCP-only stimulation (top, gray).

SkinSource leverages impulse responses that encode the physics of vibration transmission in the upper limb and enable the computational experiments described in this work. This approach relies upon the linearity of vibration transmission in the skin. Prior work has established the validity of this assumption within a stimulated digit [54]. Here, we confirm that vibration transmission across the entire upper limb behaves linearly over a wide range of input velocities, including those at which the SkinSource impulse response dataset was collected. To perform this validation, we conducted two experiments evaluating linearity via amplitude scaling (Linearity Experiment 1) and superposition (Linearity Experiment 2).

6.5.1 Experimental Setup

Skin velocities were measured at selected locations on the right hands and arms of two participants (P1 and P2; Fig. 6.5A) using a laser Doppler vibrometer (LDV; model PDV-100, Polytec, Irvine, CA; 48 kHz sample rate) placed normal to the skin at a distance of 30 cm above the participants' hands and arms. To ensure high SNR, small squares of adhesive retro-reflective tape (5 mm^2 area) were placed on the participants' skin at the measurement locations. The experimental setup was otherwise identical to that described in Section 5.3.

6.5.2 Linearity Experiment 1: Amplitude Scaling

To test amplitude scaling, sinusoids (10 frequencies between 25 and 600 Hz) and a linear sine sweep (25 to 600 Hz; 5 s duration) were applied to the tip of digit III at 5 amplitude levels (5, 10, 20, 40, and 80 mm/s zero-to-peak loaded actuator velocities). Each input was repeated for 5 trials, and a compensation filter was applied to ensure that the actuator response was flat in frequency (within 10 % of the target velocity). In

the SkinSource impulse response dataset, the maximum input velocity across all contact conditions was 21.6 mm/s.

After normalizing the sinusoid measurements by the input velocity, the responses of the lowest four amplitude levels were nearly indistinguishable (Fig. 6.5B, overlapped black traces). At the highest amplitude level (80 mm/s), nonlinearities became noticeable below 200 Hz and became more pronounced with increasing distance from the actuator (Fig. 6.5B, red trace). We found evidence of modest shifts (approximately 25°) of the fundamental and large contributions of third-order harmonics, the latter of which is consistent with observations in brain tissue [278]. Due to the observed nonlinearities, we restricted further analysis to the lowest four amplitude levels ($\leq$ 40 mm/s). We also found that the average total harmonic distortion (THD) of the sinusoid responses across all measured locations was -40 dB (Fig. 6.5C). The increased THD at 25 Hz was primarily due to displacement limitations of the actuator (Fig. 6.5C, inset). The outliers present for P2 at 600 Hz were due to a large compensation factor that degraded actuator performance. For this reason, subsequent analyses for P2 were performed only up to 500 Hz.

We used the sine sweep measurements to analyze linearity across the entire frequency spectrum (25 to 600 Hz for P1, 25 to 500 Hz for P2, 2 Hz resolution). For each repetition and measured location, we computed the frequency spectrum of the skin vibrations and performed a linear regression on the spectrum amplitudes (Fig. 6.5D). The quality of the linear fit was assessed using the adjusted coefficient of determination (adjusted R^2), with a high adjusted R^2 indicating linearity. Amplitude levels that fell within 10 % of the average noise floor or that lacked consistent estimates across trials (index of dispersion > 0.02) were removed. The mean linear fit across the frequency spectra was nearly 1 at all locations (mean adjusted $R^2 = 0.99$; Fig. 6.5E). We found variations in the distributions of fits as we moved beyond digit III, likely due to lower SNR and spurious

arm movements resulting in the deviation of the laser off of the reflective tape at the measurement locations.

6.5.3 Linearity Experiment 2: Superposition

Stimuli were applied in three contact conditions: at the distal phalanx (DP) of digit III (Condition 1), at the metacarpophalangeal joint (MCP) of digit III (Condition 2), and at the DP and MCP of digit III simultaneously (Condition 3; Fig. 6.5F, left). Stimuli were applied at only a single amplitude level (20 mm/s zero-to-peak loaded actuator velocity).

To confirm that vibrotactile transmission in the upper limb followed the superposition principle, we compared the measured vibrations during Condition 3 to the sum of independent measurements made during Conditions 1 and 2. Even in cases where significant destructive interference occurred at the measured location, the simultaneous application of sine sweeps at two locations (Condition 3) was nearly identical to the sum of skin vibrations elicited by sine sweeps applied at the two locations independently (Condition 1 + Condition 2; Fig. 6.5F, right). Across all locations for both participants, both the mean time-domain and frequency-domain Pearson correlation coefficients between Condition 1 + Condition 2 and Condition 3 were greater than 0.99, indicating that the superposition principle held.

6.5.4 Discussion

The SkinSource predictions (Eq. 6.1) rely on the principles of both amplitude scaling and superposition (i.e., linearity) to compute skin vibrations in the upper limb in response to arbitrary input forces applied at multiple input locations. The results of both experiments in this section indicate that the vibration transmission in the upper limb is linear at or below 40 mm/s (zero-to-peak), though the upper bound of this range may

depend on actuator dynamics. Thus, for the ranges at which the SkinSource dataset was captured (maximum 21.6 mm/s peak velocity), impulse responses can be used to entirely characterize the upper limb vibration response.

6.6 Conclusion

SkinSource provides data-driven upper limb models that allow users to predict the skin's vibration response to specified time-varying input forces supplied to numerous locations across the hand. In evaluations, we found that the SkinSource predictions accurately matched measurements of skin vibrations elicited under similar experimental conditions. Further, we confirmed that the entire upper limb can be considered as a linear medium for vibration transmission for input velocities within the range employed in SkinSource (< 40 mm/s zero-to-peak). These results are generally consistent with prior literature on linearity within a stimulated digit [54]. The toolbox and dataset contributed by SkinSource provide a versatile framework for supporting haptics research at the intersection of mechanics, perception, and neuroscience. By reducing the need for time-intensive measurements using a data-driven computational methodology, SkinSource may aid in modeling vibrotactile transmission in the upper limb, understanding the neuromechanical basis of touch perception, and accelerating the design and engineering of novel haptic technologies.

Similar data-driven modeling techniques can be found in the field of audio engineering. These approaches involve encoding sound transfer from points in 3D space to the human ear, analogous to encoding vibration transmission in the skin. Measurements over large numbers of participants have enabled the personalization of 3D audio rendering based on user-specific anthropometric features, which has significantly improved the quality and accessibility of 3D audio reproduction over headphones [279, 280, 281]. Though Skin-

Source currently integrates only four upper limb models, which limits its ability to generalize across a more diverse population, the data-driven modeling techniques employed here may enable similar personalization for haptic rendering given larger datasets.

In its current form, SkinSource nevertheless provides a versatile computational testbed enabling the systematic study of vibration transmission in the hand and arm for applications in haptic research and design. However, our characterization of vibration transmission in the upper limb is not exhaustive and does not capture skin vibrations for all possible contact conditions, upper limbs, input locations, or output locations. Notably, the spatial resolution of SkinSource output locations does not satisfy the spatial Nyquist sampling criterion, which requires that high-frequency skin vibrations ($\geq 300\,\text{Hz}$) be sampled at $\leq 1\,\text{cm}$ spacing to accurately predict vibrations at points between measurement locations [13]. In addition, to mitigate low-frequency artifacts and satisfy the temporal Nyquist sampling criterion at high frequencies, SkinSource input signals should be bandlimited between 25 and 600 Hz. This frequency range nonetheless encompasses a large proportion of frequencies relevant to vibrotactile perception, particularly for Pacinian and Meissner corpuscle mechanoreceptors [97]. Finally, SkinSource predicts skin vibrations in response to stimuli applied normally to the skin surface using a contact surface with dimensions of $7\times7\,\text{mm}$. Some differences in the amplitude and phase of the upper limb skin response would be expected for stimuli applied in shear directions or with different contact conditions. These constraints highlight several opportunities for extending this work in the future.

Chapter 7

Conclusion

The sense of touch is fundamental to our interactions with the environment, yet our understanding of its underlying biomechanical and neural mechanisms—especially away from the location of touch contact—remains limited. Recent work has demonstrated that touch-elicited skin oscillations transmitted far from the contact location are relevant to touch perception [4, 17, 18], but little is known about their role in the tactile system. This dissertation advances our knowledge of human tactile sensing by characterizing the widespread biomechanical transmission of touch-elicited skin oscillations and analyzing its influence on the spiking responses of mechanoreceptor populations in the hand. Employing data-driven modeling and simulation methods, the work here addresses and overcomes experimental challenges in capturing skin measurements and neural recordings.

Chapter 3 introduces a data-driven approach for simulating whole-hand mechanoreceptor population responses. High-resolution optical vibrometry measurements of skin oscillations were collected to drive physiologically validated neuron models distributed across the hand. The vibrometry measurements demonstrated that touch-elicited skin oscillations are biomechanically filtered in a frequency- and location-dependent manner

as they are transmitted across the hand. This filtering process pre-neuronally modifies the tactile inputs to widespread Pacinian corpuscle mechanoreceptors (PCs), diversifying their response characteristics and neural activity across the hand. This diversity enables PCs away from the contact location to capture touch information not encoded by PCs within the contact region, supporting encoding efficiency in the tactile system. While touch research often focuses on the mechanical and neural responses near locations of contact, Chapter 3 emphasizes the need for a spatially distributed, populational-level understanding of the tactile system. This chapter also builds upon research highlighting the importance of both neural and non-neural mechanisms in sensory systems, including the tactile [175], auditory [157, 158], visual [159, 160], and vestibular [156] systems. By incorporating both aspects, the findings shed light on surprising and unexplained aspects of the human tactile system, including the perception of complex vibrotactile stimuli [4, 119, 120, 121], intact sensation despite tactile impairment [17, 18], and PC distribution [3, 103] and density [81, 82] in the hand.

Leveraging the data-driven methodology introduced in Chapter 3, Chapter 4 investigates how whole-hand PC populations encode natural touch interactions. This work explores neural sensory coding in natural settings, which has been recognized as critically important in neuroscience [122, 123, 124, 125] yet remains challenging to study in the tactile system due to experimental constraints. Specifically, Chapter 4 investigates the spatiotemporal organization of touch information within PC population responses, addressing topics in sensory neuroscience such as rate versus spike timing codes and spatiotemporal integration. While previous studies have focused on the temporal organization of information in PC responses [15, 112], this chapter provides novel insights into the spatial organization. The spatial organization had a greater impact on gesture encoding than the temporal organization, and it was crucial for digit separation to be preserved within the spatial structure of the PC population responses. These results

align with a previous study showing that whole-hand skin oscillations during the same touch interactions could be efficiently described by a small set of basis functions emphasizing digit individuation [2]. This observation complements findings from Chapter 3 about the influence of biomechanical transmission on PC activity. Further reflecting insights from Chapter 3, Chapter 4 demonstrates that PCs far from the contact locations encode significant information about the touch interactions, showing that biomechanical transmission enables remote tactile encoding [12, 17, 18].

Chapter 5 presents a wrist-worn device that utilizes the information carried by widespread skin oscillations to digitally transcribe tactile sign language (TSL) letters performed on the hand. This work builds upon an expanding body of research that employs acoustic measurements to transform the skin into a touch-input interface [60, 221, 222, 223]. Several temporal, spectral, and spectrotemporal features were extracted from the skin oscillations captured by four accelerometers mounted on the wrist and passed into simple classifiers, such as an SVM and a random forest. The classification accuracy was high, even with simple and un-optimized methods: 94 % with four accelerometers and 87 % with two. This work addresses a significant accessibility gap by developing the first digital input device for TSL, facilitating digital transcription and communication. Additionally, the ideas and methods underlying this device have broader applications for consumer wearables, such as smartwatches, by enabling the skin to act as a medium for digital gesture inputs and leaving the hand free.

Motivated by the demonstrated significance of biomechanical transmission in the tactile system and in haptic device applications, as well as the practical challenges associated with acquiring skin measurements, Chapter 6 introduces a versatile toolbox for the computational analysis of biomechanical transmission in the upper limb. This toolbox enables users to predict skin oscillations generated by arbitrary tactile stimuli applied at one or more locations on the hand entirely in software. The toolbox utilizes

over 5000 measured impulse responses that fully encode the physics of biomechanical transmission, employing a data-driven methodology similar to that in Chapter 3. This approach was validated by confirming the linearity of biomechanical transmission in the upper limb and by comparing the toolbox outputs to independent measurements across a wide frequency range (25 to 600 Hz). This work addresses limitations in prior models of biomechanical transmission, which are typically restricted to small skin areas or rely on simplifying assumptions that reduce spatiotemporal resolution. Furthermore, the toolbox offers an accessible, inexpensive, and efficient alternative to the specialized, expensive, and time-intensive methods traditionally required to characterize biomechanical transmission. While it does not eliminate the need for skin measurements, Chapter 6 can inform research on the neuromechanical basis of touch, similar to that in Chapters 3 and 4, and guide the design of haptic devices, as demonstrated in Chapter 5. It may provide valuable direction and insight for experiments and device designs to save time and resources.

7.1 Future Research Directions

Overall, this dissertation presents many promising avenues of future research with implications for a number of areas. Specifically, Chapters 3 and 4 address several unanswered question in touch neuroscience by investigating the role of biomechanical transmission in modulating the activity of mechanoreceptors across the whole hand. Chapter 5 demonstrates a practical application of characterizing biomechanical transmission by leveraging skin oscillations to decode touch interactions within a haptic sensing device. Finally, Chapter 6 enables the investigation of biomechanical transmission *in silico*, providing a computational testbed for applications in neuroscience and haptics.

7.1.1 Tactile Neuroscience

- The findings from Chapter 3 regarding the influence of biomechanical transmission on mechanoreceptor population responses present opportunities for future research into unexplained aspects of human touch perception. For example, the perception of polyharmonic stimuli remains unexplained by current knowledge of peripheral tactile encoding. Previous research has suggested that the perception of signals with complex frequency spectra might be mediated by subpopulations of mechanoreceptors tuned to different frequencies [120, 121], although direct evidence for such subpopulations is lacking. Chapter 3 provides circumstantial evidence supporting these hypotheses by demonstrating that PC subpopulations are tuned to frequencies outside their typical range by pre-neuronal biomechanical filtering. In the future, psychophysical and perceptual experiments are needed to further elucidate the role of biomechanical transmission and filtering in shaping our sensory experience. The methodologies and findings in Chapter 3 offer a promising foundation for such explorations.

- The results in Chapter 3 suggest that pre-neuronal biomechanical filtering in the hand performs a biomechanical mapping analogous to the frequency-place transform affected by the basilar membrane in the cochlea. The similarities between the tactile and auditory systems have been noted in previous studies as well [237, 238, 282]. This suggests that in the future, insights and methodologies from auditory neuroscience could be applied to develop a better understanding of peripheral tactile encoding.

- Findings in Chapter 3 may shed light on aspects of mechanoreceptor distribution and density in the hand. Notably, regions such as the knuckles where larger oscillation amplitudes were observed coincide with areas previously identified as having

higher densities of PCs [3, 103]. Additionally, Chapter 3 provides insight into how biomechanical filtering may explain why there are hundreds or more PCs in the hand despite their large receptive fields suggesting significant response redundancy. Further research is necessary to more definitively connect the biomechanical findings of Chapter 3 with the anatomical and morphological characteristics of mechanoreceptors in the hand.

- Neuroscience research has increasingly emphasized the importance of studying neural circuitry within the natural settings where it evolved. However, investigating peripheral tactile encoding in these unconstrained, natural settings remains challenging. Chapter 4 contributes to this research by developing a computational framework for examining how populations of PCs encode natural, unconstrained touch interactions. This study provides a foundation for future research into tactile encoding in natural settings.

- The data-driven methodologies introduced in Chapters 3, 4, and 6 take a step toward developing a general computational model of human touch in the hand. Such a model would be capable of predicting biomechanical transmission, mechanoreceptor population responses, and touch perception in response to arbitrary tactile stimuli. In the immediate future, the research from this dissertation could be expanded toward this goal by including additional types of mechanoreceptors beyond PCs and incorporating data from more participants.

7.1.2 Health and Medicine

- Aging and medical conditions such as scleroderma can alter the mechanical properties of the skin and affect mechanoreceptors by reducing their number or changing their nerve conduction velocity. Such changes can negatively impact tactile sen-

sitivity and dexterous manipulation capabilities, potentially diminishing quality of life. The research presented in Chapters 3, 4, and 6 may provide insights into how these mechanical and neural changes influence biomechanical transmission and mechanoreceptor population responses, potentially contributing to new diagnostic or treatment methods.

7.1.3 Haptic Technologies

- Skin oscillations can be leveraged in haptic sensing devices because they transmit touch information across large areas of skin, as demonstrated in Chapter 5. This information can be captured and interpreted remotely by wearable sensors, like those in commercial smartwatches. Chapter 6 presents a toolbox that enables users to generate large datasets of upper limb skin oscillations in response to various touch interactions. The toolbox facilitates computational analyses, such as feature extraction on time- and frequency-domain signals, which could inform design decisions for haptic sensing devices, such as optimal sensor number, strategic sensor placements, and overall device feasibility.

- Because skin oscillations play a role in touch perception, they can be harnessed for haptic feedback devices. This has led to novel haptic feedback methods, such as creating patterns of spatial sensation [4] and focusing waves in the skin [227]. The toolbox presented in Chapter 6 enables the efficient and systematic analysis of biomechanical transmission in the upper limb for a large and diverse set of stimuli that includes various amplitude and frequency components. This may inform feedback patterns in a haptic device, such as a glove designed for use in virtual or augmented reality environments.

- The data-driven methodology introduced in Chapter 6 holds the potential for per-

sonalizing haptic rendering based on individual differences in hand anatomy and skin biomechanics. This approach is similar to data-driven modeling techniques used in audio engineering, where measurements of head-related transfer functions have enabled the customization of spatial audio rendering in headphones [279, 280, 281]. By applying similar principles and gathering more data across a diverse range of participants, the work in Chapter 6 could be leveraged to tailor haptic feedback to each user's unique physiological traits.

7.1.4 Tactile Sensory Prostheses and Robotic Tactile Sensing

- Research has shown that biomimetic methods of peripheral nerve stimulation can improve the experience and manipulation capabilities of prosthetic users [199, 201]. The findings in Chapters 3 and 4 on biomechanical transmission and its influence on mechanoreceptor populations may provide insights into improving these biomimetic stimulation techniques to produce more informative and immersive tactile feedback.

- Improving artificial tactile sensing and perception for robotic manipulation remains an active area of research, with many promising approaches inspired by the human tactile system [206, 207, 208, 209, 210]. The findings from this dissertation may provide valuable insights for improving these technologies. For example, the work presented here demonstrates how an acoustic transmission medium, akin to skin, can distribute tactile information across large areas and perform passive feature extraction. Therefore, sensors can be positioned remotely from the contact location, reducing device complexity and improving computational efficiency. Such insights may provide potential methods for improving artificial tactile technologies.

Technology that seeks to interface with or emulate the sense of touch is becoming increasingly prevalent, supporting the continued relevance of the research presented here.

This dissertation highlights the critical role of biomechanical transmission within the human tactile system and introduces data-driven tools that advance our understanding of the interplay between biomechanical and neural processes underlying the sense of touch. The methodologies and insights developed here not only contribute to current scientific knowledge but also establish a foundation for future innovations in haptic technologies.

Bibliography

[1] Y. Shao, V. Hayward, and Y. Visell, *Spatial patterns of cutaneous vibration during whole-hand haptic interactions*, *Proceedings of the National Academy of Sciences* **113** (2016), no. 15 4188–4193.

[2] Y. Shao, V. Hayward, and Y. Visell, *Compression of dynamic tactile information in the human hand*, *Science Advances* **6** (2020), no. 16.

[3] C. Germann, R. Sutter, and D. Nanz, *Novel observations of Pacinian corpuscle distribution in the hands and feet based on high-resolution 7-T MRI in healthy volunteers*, *Skeletal Radiology* **50** (2021), no. 6 1249–1255.

[4] B. Dandu, Y. Shao, and Y. Visell, *Rendering spatiotemporal haptic effects via the physics of waves in the skin*, *IEEE Transactions on Haptics* **14** (2020), no. 2 347–358.

[5] J. Cole, *Losing Touch: A man without his body*. Oxford University Press, 2016.

[6] A.-S. Augurelle, A. M. Smith, T. Lejeune, and J.-L. Thonnard, *Importance of cutaneous feedback in maintaining a secure grip during manipulation of hand-held objects*, *Journal of Neurophysiology* **89** (2003), no. 2 665–671.

[7] R. Johansson, "The effects of anesthesia on motor skills." YouTube. [Online]. Available: `https://www.youtube.com/watch?v=0LfJ3M3Kn80`.

[8] J. C. Rothwell, M. M. Traub, B. L. Day, J. A. Obeso, P. K. Thomas, and C. D. Marsden, *Manual motor performance in a deafferented man*, *Brain: A Journal of Neurology* **105 (Pt 3)** (1982) 515–542.

[9] B. S. Wilson, C. C. Finley, D. T. Lawson, R. D. Wolford, D. K. Eddington, and W. M. Rabinowitz, *Better speech recognition with cochlear implants*, *Nature* **352** (1991), no. 6332 236–238.

[10] A. A. Eshraghi, R. Nazarian, F. F. Telischi, S. M. Rajguru, E. Truy, and C. Gupta, *The cochlear implant: Historical aspects and future prospects*, *The Anatomical Record* **295** (2012), no. 11 1967–1980.

[11] D. R. Moore and R. V. Shannon, *Beyond cochlear implants: Awakening the deafened brain*, *Nature Neuroscience* **12** (2009), no. 6 686–691.

[12] B. Delhaye, V. Hayward, P. Lefèvre, and J.-L. Thonnard, *Texture-induced vibrations in the forearm during tactile exploration*, *Frontiers in Behavioral Neuroscience* **6** (2012), no. 37.

[13] L. R. Manfredi, A. T. Baker, D. O. Elias, J. F. D. Iii, M. C. Zielinski, V. S. Polashock, and S. J. Bensmaia, *The effect of surface wave propagation on neural responses to vibration in primate glabrous skin*, *PLOS ONE* **7** (2012), no. 2 e31203.

[14] J. W. Andrews, M. J. Adams, and T. D. Montenegro-Johnson, *A universal scaling law of mammalian touch*, *Science Advances* **6** (2020), no. 41 eabb6912.

[15] G. Corniani, M. A. Casal, S. Panzeri, and H. P. Saal, *Population coding strategies in human tactile afferents*, *PLOS Computational Biology* **18** (2022), no. 12 e1010763.

[16] N. Tummala, Y. Shao, and Y. Visell, *Spatiotemporal organization of touch information in tactile neuron population responses*, in *2023 IEEE World Haptics Conference*, (Delft, Netherlands), pp. 183–189, IEEE, 2023.

[17] X. Libouton, O. Barbier, Y. Berger, L. Plaghki, and J.-L. Thonnard, *Tactile roughness discrimination of the finger pad relies primarily on vibration sensitive afferents not necessarily located in the hand*, *Behavioural Brain Research* **229** (2012), no. 1 273–279.

[18] S. S. Nagi, S. McIntyre, K. K. W. Ng, D. A. Mahns, I. Birznieks, and R. M. Vickery, *Contribution of remote Pacinian corpuscles to flutter-range frequency discrimination in humans*, *Research Square* (2023).

[19] N. Tummala, G. Reardon, B. Dandu, Y. Shao, H. P. Saal, and Y. Visell, *Pre-neuronal biomechanical filtering modulates and diversifies whole-hand tactile encoding*, *bioRxiv* (2024).

[20] S. Dinulescu, N. Tummala, G. Reardon, B. Dandu, D. Goetz, S. Topp, and Y. Visell, *A smart bracelet supporting tactile communication and interaction*, in *2022 IEEE Haptics Symposium*, (Santa Barbara, CA, USA), pp. 1–7, IEEE, 2022.

[21] N. Tummala, G. Reardon, S. Fani, D. Goetz, M. Bianchi, and Y. Visell, *SkinSource: A data-driven toolbox for predicting touch-elicited vibrations in the upper limb*, in *2024 IEEE Haptics Symposium*, (Long Beach, CA, USA), pp. 53–60, IEEE, 2024.

[22] S. J. Lederman and R. L. Klatzky, *Hand movements: A window into haptic object recognition*, *Cognitive Psychology* **19** (1987), no. 3 342–368.

[23] Z.-M. Li and A. D. Nimbarte, *Peripheral median nerve block impairs precision pinch movement*, *Clinical Neurophysiology* **117** (2006), no. 9 1941–1948.

[24] S. J. Bensmaia and M. Hollins, *The vibrations of texture*, *Somatosensory & Motor Research* **20** (2003), no. 1 33–43.

[25] R. S. Johansson and J. R. Flanagan, *Coding and use of tactile signals from the fingertips in object manipulation tasks*, *Nature Reviews Neuroscience* **10** (2009), no. 55 345–359.

[26] A. J. Brisben, S. S. Hsiao, and K. O. Johnson, *Detection of vibration transmitted through an object grasped in the hand*, *Journal of Neurophysiology* **81** (1999), no. 4 1548–1558.

[27] L. E. Miller, L. Montroni, E. Koun, R. Salemme, V. Hayward, and A. Farnè, *Sensing with tools extends somatosensory processing beyond the body*, *Nature* **561** (2018), no. 7722 239–242.

[28] L. A. Jones and S. J. Lederman, *Human Hand Function*, ch. 2. Oxford University Press, 1 ed., 2006.

[29] B. P. Delhaye, F. Schiltz, A. Barrea, J.-L. Thonnard, and P. Lefèvre, *Measuring fingerpad deformation during active object manipulation*, *Journal of Neurophysiology* **126** (2021), no. 4 1455–1464.

[30] L. Willemet, N. Huloux, and M. Wiertlewski, *Efficient tactile encoding of object slippage*, *Scientific Reports* **12** (2022), no. 11 13192.

[31] S. du Bois de Dunilac, D. Córdova Bulens, P. Lefèvre, S. J. Redmond, and B. P. Delhaye, *Biomechanics of the finger pad in response to torsion*, *Journal of the Royal Society Interface* **20** (2023), no. 201 20220809.

[32] G. Corniani, Z. S. Lee, M. J. Carré, R. Lewis, B. P. Delhaye, and H. P. Saal, *Sub-surface deformation of individual fingerprint ridges during tactile interactions*, *eLife* **13** (2024) RP93554.

[33] X. Liu, R. Maiti, Z. H. Lu, M. J. Carré, S. J. Matcher, and R. Lewis, *New non-invasive techniques to quantify skin surface strain and sub-surface layer deformation of finger-pad during sliding*, *Biotribology* **12** (2017) 52–58.

[34] N. Nakazawa, R. Ikeura, and H. Inooka, *Characteristics of human fingertips in the shearing direction*, *Biological Cybernetics* **82** (2000), no. 3 207–214.

[35] Q. Wang and V. Hayward, *In vivo biomechanics of the fingerpad skin under local tangential traction*, *Journal of Biomechanics* **40** (2007), no. 4 851–860.

[36] X. Liang and S. A. Boppart, *Biomechanical properties of in vivo human skin from dynamic optical coherence elastography*, *IEEE Transactions on Biomedical Engineering* **57** (2010), no. 4 953–959.

[37] M. Wiertlewski and V. Hayward, *Mechanical behavior of the fingertip in the range of frequencies and displacements relevant to touch*, *Journal of Biomechanics* **45** (2012), no. 11 1869–1874.

[38] S. P. Kearney, A. Khan, Z. Dai, and T. J. Royston, *Dynamic viscoelastic models of human skin using optical elastography*, *Physics in Medicine & Biology* **60** (2015), no. 17 6975.

[39] J. W. Jor, M. D. Parker, A. J. Taberner, M. P. Nash, and P. M. Nielsen, *Computational and experimental characterization of skin mechanics: Identifying current challenges and future directions*, *WIREs Systems Biology and Medicine* **5** (2013), no. 5 539–556.

[40] E. R. Serina, E. Mockensturm, C. D. Mote, and D. Rempel, *A structural model of the forced compression of the fingertip pulp*, *Journal of Biomechanics* **31** (1998), no. 7 639–646.

[41] D. Sachs, A. Wahlsten, S. Kozerke, G. Restivo, and E. Mazza, *A biphasic multilayer computational model of human skin*, *Biomechanics and Modeling in Mechanobiology* **20** (2021), no. 3 969–982.

[42] K. Dandekar, B. I. Raju, and M. A. Srinivasan, *3-D finite-element models of human and monkey fingertips to investigate the mechanics of tactile sense*, *Journal of Biomechanical Engineering* **125** (2003), no. 5 682–691.

[43] D. E. W. John Z. Wu and R. G. Dong, *Three-dimensional finite element simulations of the mechanical response of the fingertip to static and dynamic compressions*, *Computer Methods in Biomechanics and Biomedical Engineering* **9** (2006), no. 1 55–63.

[44] D. T. Pawluk and R. D. Howe, *Dynamic lumped element response of the human fingerpad*, *Journal of Biomedical Engineering* **121** (1999), no. 2 178–183.

[45] M. J. Adams, S. A. Johnson, P. Lefèvre, V. Lévesque, V. Hayward, T. André, and J.-L. Thonnard, *Finger pad friction and its role in grip and touch*, *Journal of The Royal Society Interface* **10** (2013), no. 80.

[46] B. P. Delhaye, F. Schiltz, F. Crevecoeur, J.-L. Thonnard, and P. Lefèvre, *Fast grip force adaptation to friction relies on localized fingerpad strains*, *Science Advances* **10** (2024), no. 3 eadh9344.

[47] H. E. von Gierke, H. L. Oestreicher, E. K. Franke, H. O. Parrack, and W. W. von Wittern, *Physics of vibrations in living tissues*, *Journal of Applied Physiology* **4** (1952), no. 12 886–900.

[48] T. J. Moore, *A survey of the mechanical characteristics of skin and tissue in response to vibratory stimulation*, *IEEE Transactions on Man-Machine Systems* **11** (1970), no. 1 79–84.

[49] R. O. Potts, D. A. Chrisman, and E. M. Buras, *The dynamic mechanical properties of human skin in vivo*, *Journal of Biomechanics* **16** (1983), no. 6 365–372.

[50] B. Duvernoy, E. Kindström, A. Fridberger, and S. McIntyre, *Tracking submicrometer vibrations in depth in the glabrous skin*, in *2023 IEEE World Haptics Conference*, (Delft, Netherlands), IEEE, 2023.

[51] H. E. von Gierke, *Dynamic characteristics of the human body*, in *Perspectives in Biomedical Engineering* (R. M. Kenedi, ed.), pp. 193–202. Palgrave Macmillan London, Glasgow, Scotland, 1973.

[52] D. D. Reynolds and R. H. Keith, *Hand-arm vibration, part I: Analytical model of the vibration response characteristics of the hand*, *Journal of Sound and Vibration* **51** (1977), no. 2 237–253.

[53] D. D. Reynolds and E. N. Angevine, *Hand-arm vibration, part II: Vibration transmission characteristics of the hand and arm*, *Journal of Sound and Vibration* **51** (1977), no. 2 255–265.

[54] C. Fradet, L. R. Manfredi, S. Bensmaia, and V. Hayward, *Fingertip skin as a linear medium for wave propagation*, in *2017 IEEE World Haptics Conference*, (Munich, Germany), pp. 507–510, 2017.

[55] L. R. Manfredi, H. P. Saal, K. J. Brown, M. C. Zielinski, J. F. Dammann, V. S. Polashock, and S. J. Bensmaia, *Natural scenes in tactile texture*, *Journal of Neurophysiology* **111** (2014), no. 9 1792–1802.

[56] G. Reardon, B. Dandu, Y. Shao, and Y. Visell, *Shear shock waves mediate haptic holography via focused ultrasound*, *Science Advances* **9** (2023), no. 9 eadf2037.

[57] S. J. Kirkpatrick, D. D. Duncan, and L. Fang, *Low-frequency surface wave propagation and the viscoelastic behavior of porcine skin*, *Journal of Biomedical Optics* **9** (2004), no. 6 1311–1319.

[58] Y. Shao, H. Hu, and Y. Visell, *A wearable tactile sensor array for large area remote vibration sensing in the hand*, *IEEE Sensors Journal* **20** (2020), no. 12 6612–6623.

[59] K. O. Sofia and L. A. Jones, *Mechanical and psychophysical studies of surface wave propagation during vibrotactile stimulation*, *IEEE Transactions on Haptics* **6** (2013), no. 3 320–329.

[60] C. Harrison, D. Tan, and D. Morris, *Skinput: Appropriating the body as an input surface*, in *Proceedings of the SIGCHI Conference on Human Factors in Computing Systems*, CHI '10, (New York, NY, USA), pp. 453–462, Association for Computing Machinery, 2010.

[61] U. B. Rongala, A. Seyfarth, V. Hayward, and H. Jörntell, *The import of skin tissue dynamics in tactile sensing*, *bioRxiv* (2023).

[62] C. P. Carvalho, J. F. S. Costa-Júnior, C. d. S. Rangel, and W. C. d. A. Pereira, *Measurement of shear wave speed and normalized elastic modulus of human skin with and without dermal striae using shear wave elastography*, *Ultrasound in Medicine & Biology* **47** (2021), no. 3 454–470.

[63] M. Fritz, *An improved biomechanical model for simulating the strain of the hand-arm system under vibration stress*, *Journal of Biomechanics* **24** (1991), no. 12 1165–1171.

[64] G. Serhat and K. J. Kuchenbecker, *Free and forced vibration modes of the human fingertip*, *Applied Sciences* **11** (2021), no. 12 5709.

[65] J. Z. Wu, D. E. Welcome, K. Krajnak, and R. G. Dong, *Finite element analysis of the penetrations of shear and normal vibrations into the soft tissues in a fingertip*, *Medical Engineering & Physics* **29** (2007), no. 6 718–727.

[66] R. Panchal, L. Horton, P. Poozesh, J. Baqersad, and M. Nasiriavanaki, *Vibration analysis of healthy skin: toward a noninvasive skin diagnosis methodology*, *Journal of Biomedical Optics* **24** (2019), no. 1 015001–1–11.

[67] H. P. Saal, B. P. Delhaye, B. C. Rayhaun, and S. J. Bensmaia, *Simulating tactile signals from the whole hand with millisecond precision*, *Proceedings of the National Academy of Sciences* **114** (2017), no. 28 E5693–E5702.

[68] F. Badrieh, *Time Convolution with Impulse Response*, pp. 465–479. Springer International Publishing, Cham, 2018.

[69] C. Roads, *Musical sound transformation by convolution*, in *Proceedings of the International Computer Music Conference*, pp. 102–102, International Computer Music Association, 1993.

[70] J. Martindale, J. Mayhew, J. Berwick, M. Jones, C. Martin, D. Johnston, P. Redgrave, and Y. Zheng, *The hemodynamic impulse response to a single neural event*, *Journal of Cerebral Blood Flow & Metabolism* **23** (2003), no. 5 546–555.

[71] W. R. Peltier, *The impulse response of a Maxwell Earth*, *Reviews of Geophysics* **12** (1974), no. 4 649–669.

[72] R. S. Johansson and A. B. Vallbo, *Tactile sensory coding in the glabrous skin of the human hand*, *Trends in Neurosciences* **6** (1983) 27–32.

[73] L. A. Jones and A. M. Smith, *Tactile sensory system: encoding from the periphery to the cortex*, *WIREs Systems Biology and Medicine* **6** (2014), no. 3 279–287.

[74] V. E. Abraira and D. D. Ginty, *The sensory neurons of touch*, *Neuron* **79** (2013), no. 4.

[75] A. Zimmerman, L. Bai, and D. D. Ginty, *The gentle touch receptors of mammalian skin*, *Science* **346** (2014), no. 6212 950–954.

[76] A. Handler and D. D. Ginty, *The mechanosensory neurons of touch and their mechanisms of activation*, *Nature Reviews Neuroscience* **22** (2021), no. 9 521–537.

[77] P. Gillespie and R. Walker, *Molecular basis of mechanosensory transduction*, *Nature* **413** (2001), no. 6852 194–202.

[78] L. E. Bilston and C. L. Stucky, *Mechanotransduction in the nervous system*, in *Neural Tissue Biomechanics* (L. E. Bilston, ed.), pp. 231–245. Springer, Berlin, Heidelberg, 2011.

[79] J. Hao, C. Bonnet, M. Amsalem, J. Ruel, and P. Delmas, *Transduction and encoding sensory information by skin mechanoreceptors*, *Pflügers Archiv-European Journal of Physiology* **467** (2015), no. 1 10–119.

[80] K. O. Johnson, *The roles and functions of cutaneous mechanoreceptors*, *Current Opinion in Neurobiology* **11** (2001), no. 4 455–461.

[81] R. S. Johansson and A. B. Vallbo, *Tactile sensibility in the human hand: Relative and absolute densities of four types of mechanoreceptive units in glabrous skin.*, *The Journal of Physiology* **286** (1979), no. 1 283–300.

[82] G. Corniani and H. P. Saal, *Tactile innervation densities across the whole body*, *Journal of Neurophysiology* **124** (2020), no. 4 1229–1240.

[83] H. P. Saal and S. J. Bensmaia, *Touch is a team effort: Interplay of submodalities in cutaneous sensibility*, *Trends in Neurosciences* **37** (2014), no. 12 689–697.

[84] C. C. Hunt and A. K. McIntyre, *Characteristics of responses from receptors from the flexor longus digitorum muscle and the adjoining interosseous region of the cat*, *The Journal of Physiology* **153** (1960), no. 1 74–87.

[85] C. C. Hunt, *On the nature of vibration receptors in the hind limb of the cat*, *The Journal of Physiology* **155** (1961), no. 1 175–186.

[86] R. T. Verrillo, *Vibrotactile sensitivity and the frequency response of the Pacinian corpuscle*, *Psychonomic Science* **4** (1966), no. 1 135–136.

[87] R. S. Johansson, *Tactile sensibility in the human hand: receptive field characteristics of mechanoreceptive units in the glabrous skin area.*, *The Journal of Physiology* **281** (1978), no. 1 101–125.

[88] Y. Tanaka, T. Ito, M. Hashimoto, M. Fukasawa, N. Usuda, and A. Sano, *Collagen fibers induce expansion of receptive field of Pacinian corpuscles*, *Advanced Robotics* **29** (2015), no. 11 735–741.

[89] S. Bensmaia and M. Hollins, *Pacinian representations of fine surface texture*, *Perception & Psychophysics* **67** (2005), no. 5 842–854.

[90] S. J. Bolanowski and J. J. Zwislocki, *Intensity and frequency characteristics of Pacinian corpuscles. I. Action potentials*, *Journal of Neurophysiology* **51** (1984), no. 4 793–811.

[91] D. C. Pease and T. A. Quilliam, *Electron microscopy of the Pacinian corpuscle*, *The Journal of Biophysical and Biochemical Cytology* **3** (1957), no. 3 331–342.

[92] N. Cauna and G. Mannan, *The structure of human digital Pacinian corpuscles (corpuscula lamellosa) and its functional significance*, *Journal of Anatomy* **92** (1958), no. Pt 1.

[93] J. Bell, S. Bolanowski, and M. H. Holmes, *The structure and function of Pacinian corpuscles: A review*, *Progress in Neurobiology* **42** (1994), no. 1 79–128.

[94] W. R. Loewenstein and M. Mendelson, *Components of receptor adaptation in a Pacinian corpuscle*, *Journal of Physiology* **177** (1965), no. 3 377–397.

[95] W. R. Loewenstein and R. Skalak, *Mechanical transmission in a Pacinian corpuscle. An analysis and a theory*, *The Journal of Physiology* **182** (1966), no. 2 346–378.

[96] J. C. Quindlen, H. K. Stolarski, M. D. Johnson, and V. H. Barocas, *A multiphysics model of the Pacinian corpuscle*, *Integrative Biology* **8** (2016), no. 11 1111–1125.

[97] R. S. Johansson, U. Landström, and R. Lundström, *Responses of mechanoreceptive afferent units in the glabrous skin of the human hand to sinusoidal skin displacements*, *Brain Research* **244** (1982), no. 1 17–25.

[98] M. A. Muniak, S. Ray, S. S. Hsiao, J. F. Dammann, and S. J. Bensmaia, *The neural coding of stimulus intensity: Linking the population response of mechanoreceptive afferents with psychophysical behavior*, *Journal of Neuroscience* **27** (2007), no. 43 11687–11699.

[99] M. Sato, *Response of Pacinian corpuscles to sinusoidal vibration*, *The Journal of Physiology* **159** (1961), no. 3 391–409.

[100] W. H. Talbot, I. Darian-Smith, H. H. Kornhuber, and V. B. Mountcastle, *The sense of flutter-vibration: Comparison of the human capacity with response patterns of mechanoreceptive afferents from the monkey hand*, *Journal of Neurophysiology* **31** (1968), no. 2 301–334.

[101] E. P. Gardner, *Touch*, in *Principles of Neural Science* (E. R. Kandel, J. H. Schwartz, T. M. Jessell, S. A. Siegelbaum, and A. J. Hudspeth, eds.), ch. 19, pp. 435–469. McGraw-Hill Medical, New York, 5 ed., 2013.

[102] V. B. Mountcastle, R. H. LaMotte, and G. Carli, *Detection thresholds for stimuli in humans and monkeys: comparison with threshold events in mechanoreceptive afferent nerve fibers innervating the monkey hand.*, *Journal of Neurophysiology* **35** (1972), no. 1 122–136.

[103] B. Stark, T. Carlstedt, R. G. Hallin, and M. Risling, *Distribution of human Pacinian corpuscles in the hand: A cadaver study*, *Journal of Hand Surgery* **23** (1998), no. 3 370–372.

[104] V. B. Mountcastle, *The Sensory Hand: Neural Mechanisms of Somatic Sensation*. Harvard University Press, 2005.

[105] E. D. Adrian, *The messages in sensory nerve fibres and their interpretation*, *Proceedings of the Royal Society of London. Series B, Containing Papers of a Biological Character* **109** (1931), no. 760 1–18.

[106] M. D. Plumbley and S. A. Abdallah, *Information theory and sensory perception*, in *Design and Information in Biology: From Molecules to Systems* (J. A. Bryant, M. A. Atherton, and M. W. Collins, eds.), vol. 2, ch. 7, pp. 205–233. WIT Press, 2007.

[107] J. J. Atick, *Could information theory provide an ecological theory of sensory processing?*, *Network: Computation in Neural Systems* **3** (1992), no. 2 213–251.

[108] H. B. Barlow, *Possible principles underlying the transformations of sensory messages*, in *Sensory Communication* (W. A. Rosenblith, ed.), ch. 13, pp. 217–234. The MIT Press, 1961.

[109] E. P. Simoncelli and B. A. Olshausen, *Natural image statistics and neural representation*, *Annual Review of Neuroscience* **24** (2001), no. 1 1193–1216.

[110] F. Attneave, *Some informational aspects of visual perception.*, *Psychological Review* **61** (1954), no. 3 183–193.

[111] Z. Pan, J. Wu, M. Zhang, H. Li, and Y. Chua, *Neural population coding for effective temporal classification*, in *2019 International Joint Conference on Neural Networks (IJCNN)*, pp. 1–8, 2019.

[112] E. L. Mackevicius, M. D. Best, H. P. Saal, and S. J. Bensmaia, *Millisecond precision spike timing shapes tactile perception*, *Journal of Neuroscience* **32** (2012), no. 44 15309.

[113] D. Aronov, D. S. Reich, F. Mechler, and J. D. Victor, *Neural coding of spatial phase in V1 of the macaque monkey*, *Journal of Neurophysiology* **89** (2003), no. 6 3304–3327.

[114] J. Gautrais and S. Thorpe, *Rate coding versus temporal order coding: a theoretical approach*, *Biosystems* **48** (1998), no. 1-3 57–65.

[115] M. A. Harvey, H. P. Saal, J. F. Dammann III, and S. J. Bensmaia, *Multiplexing stimulus information through rate and temporal codes in primate somatosensory cortex*, *PLOS Biology* **11** (2013), no. 5 e1001558.

[116] Y. Zuo, H. Safaai, G. Notaro, A. Mazzoni, S. Panzeri, and M. E. Diamond, *Complementary contributions of spike timing and spike rate to perceptual decisions in rat S1 and S2 cortex*, *Current Biology* **25** (2015), no. 3 357–363.

[117] A. W. Goodwin and H. E. Wheat, *Sensory signals in neural populations underlying tactile perception and manipulation*, *Annual Review of Neuroscience* **27** (2004) 53–77.

[118] A. W. Goodwin and H. E. Wheat, *Physiological mechanisms of the receptor system*, in *Human Haptic Perception: Basics and Applications* (M. Grunwald, ed.), ch. 7, pp. 93–102. Springer, 2008.

[119] T.-l. S. Le, G. Bailly, E. Vezzoli, M. Auvray, and D. Gueorguiev, *Tactile sensitivity to the frequency spectrum of complex vibrotactile signals*, *bioRxiv* (2023).

[120] S. Bensmaia, M. Hollins, and J. Yau, *Vibrotactile intensity and frequency information in the Pacinian system: A psychophysical model*, *Perception & Psychophysics* **67** (2005), no. 5 828–841.

[121] F. A. Russo, P. Ammirante, and D. I. Fels, *Vibrotactile discrimination of musical timbre*, *Journal of Experimental Psychology: Human Perception and Performance* **38** (2012), no. 4 822–826.

[122] G. Felsen and Y. Dan, *A natural approach to studying vision*, *Nature Neuroscience* **8** (2005), no. 12 1643–1646.

[123] W. Einhäuser and P. König, *Getting real—sensory processing of natural stimuli*, *Current opinion in neurobiology* **20** (2010), no. 3 389–395.

[124] A. Huk, K. Bonnen, and B. J. He, *Beyond trial-based paradigms: Continuous behavior, ongoing neural activity, and natural stimuli*, *Journal of Neuroscience* **38** (2018), no. 35 7551–7558.

[125] C. T. Miller, D. Gire, K. Hoke, A. C. Huk, D. Kelley, D. A. Leopold, M. C. Smear, F. Theunissen, M. Yartsev, and C. M. Niell, *Natural behavior is the language of the brain*, *Current Biology* **32** (2022), no. 10 R482–R493.

[126] M. S. Lewicki, *Efficient coding of natural sounds*, *Nature Neuroscience* **5** (2002), no. 44 356–363.

[127] E. Smith and M. Lewicki, *Efficient auditory coding*, *Nature* **439** (2006) 978–982.

[128] X. Pitkow and M. Meister, *Decorrelation and efficient coding by retinal ganglion cells*, *Nature Neuroscience* **15** (2012), no. 44 628–635.

[129] W. Młynarski and J. H. McDermott, *Learning midlevel auditory codes from natural sound statistics*, *Neural Computation* **30** (2018), no. 3 631–669.

[130] A. I. Weber, H. P. Saal, J. D. Lieber, J.-W. Cheng, L. R. Manfredi, J. F. Dammann III, and S. J. Bensmaia, *Spatial and temporal codes mediate the tactile perception of natural textures*, *Proceedings of the National Academy of Sciences* **110** (2013), no. 42 17107–17112.

[131] J. Turecek and D. D. Ginty, *Coding of self and environment by Pacinian neurons in freely moving animals*, *bioRxiv* (2023).

[132] A. M. S. Maallo, B. Duvernoy, H. Olausson, and S. McIntyre, *Naturalistic stimuli in touch research*, *Current Opinion in Neurobiology* **75** (2022) 102570.

[133] Å. Vallbo and K.-E. Hagbarth, *Activity from skin mechanoreceptors recorded percutaneously in awake human subjects*, *Experimental Neurology* **21** (1968), no. 3 270–289.

[134] Å. B. Vallbo, *Microneurography: how it started and how it works*, *Journal of Neurophysiology* **120** (2018), no. 3 1415–1427.

[135] R. Ackerley and R. H. Watkins, *Microneurography: Recordings from single neurons in human peripheral nerves*, in *Somatosensory Research Methods* (N. P. Holmes, ed.), pp. 305–331. Springer US, New York, NY, 2023.

[136] T. Hamano, R. Kaji, A. F. Diaz, N. Kohara, N. Takamatsu, T. Uchiyama, H. Shibasaki, and J. Kimura, *Vibration-evoked sensory nerve action pontentials derived from Pacinian corpuscles*, *Electroencephalography and Clinical Neurophysiology* **89** (1993), no. 4 278–286.

[137] I. Hashimoto, K. Yoshikawa, M. Sasaki, T. Gatayama, and M. Nomura, *Sensory nerve action potentials elicited by mechanical air-puff stimulation of the index finger in man*, *Electroencephalography and Clinical Neurophysiology* **72** (1989), no. 4 321–333.

[138] M. Sonekatsu and J. G. Gu, *Functional properties of mechanoreceptors in mouse whisker hair follicles determined by the pressure-clamped single-fiber recording technique*, *Neuroscience Letters* **707** (2019) 134321.

[139] M. Sonekatsu, H. Yamada, and J. G. Gu, *Pressure-clamped single-fiber recording technique: A new recording method for studying sensory receptors*, *Molecular Pain* **16** (2020).

[140] A. I. Kashkoush, R. A. Gaunt, L. E. Fisher, T. M. Bruns, and D. J. Weber, *Recording single-and multi-unit neuronal action potentials from the surface of the dorsal root ganglion*, *Scientific Reports* **9** (2019), no. 1 2786.

[141] S. S. Kim, A. P. Sripati, and S. J. Bensmaia, *Predicting the timing of spikes evoked by tactile stimulation of the hand*, *Journal of Neurophysiology* **104** (2010), no. 3 1484–1496.

[142] Y. Dong, S. Mihalas, S. S. Kim, T. Yoshioka, S. Bensmaia, and E. Niebur, *A simple model of mechanotransduction in primate glabrous skin*, *Journal of Neurophysiology* **109** (2013), no. 5 1350–1359.

[143] N. Katic, R. K. Siqueira, L. Cleland, N. Strzalkowski, L. Bent, S. Raspopovic, and H. Saal, *Modeling foot sole cutaneous afferents: FootSim*, *iScience* **26** (2023), no. 1 105874.

[144] D. Esposito, F. Lanotte, C. Mugnai, L. Massari, D. Camboni, A. Mazzoni, and C. M. Oddo, *A neuromorphic model to match the spiking activity of Merkel mechanoreceptors with biomimetic tactile sensors for bioengineering applications*, *IEEE Transactions on Medical Robotics and Bionics* **1** (2019), no. 2 97–105.

[145] I. Nemoto, S. Miyazaki, M. Saito, and T. Utsunomiya, *Behavior of solutions of the Hodgkin-Huxley equations and its relation to properties of mechanoreceptors*, *Biophysical Journal* **15** (1975), no. 5 469–479.

[146] A. W. Freeman and K. O. Johnson, *Cutaneous mechanoreceptors in macaque monkey: temporal discharge patterns evoked by vibration, and a receptor model*, *The Journal of Physiology* **323** (1982), no. 1 21–41.

[147] P. Slavík and J. Bell, *A mechanoreceptor model for rapidly and slowly adapting afferents subjected to periodic vibratory stimuli*, *Mathematical Biosciences* **130** (1995), no. 1 1–23.

[148] Q. Ouyang, J. Wu, Z. Shao, M. Wu, and Z. Cao, *A Python code for simulating single tactile receptors and the spiking responses of their afferents*, *Frontiers in Neuroinformatics* **13** (2019).

[149] D. Deflorio, M. Di Luca, and A. M. Wing, *Skin and mechanoreceptor contribution to tactile input for perception: A review of simulation models*, *Frontiers in Human Neuroscience* **16** (2022).

[150] K. O. Johnson, *Reconstruction of population response to a vibratory stimulus in quickly adapting mechanoreceptive afferent fiber population innervating glabrous skin of the monkey.*, *Journal of Neurophysiology* **37** (1974), no. 1 48–72.

[151] J. C. Quindlen-Hotek and V. H. Barocas, *A finite-element model of mechanosensation by a Pacinian corpuscle cluster in human skin*, *Biomechanics and Modeling in Mechanobiology* **17** (2018), no. 4 1053–1067.

[152] G. J. Gerling, I. I. Rivest, D. R. Lesniak, J. Scanlon, and L. Wan, *Validating a population model of tactile mechanotransduction of slowly adapting type I afferents at levels of skin mechanics, single-unit response and psychophysics*, *IEEE Transactions on Haptics* **7** (2014) 216–228.

[153] A. P. Sripati, S. J. Bensmaia, and K. O. Johnson, *A continuum mechanical model of mechanoreceptive afferent responses to indented spatial patterns*, *Journal of Neurophysiology* **95** (2006), no. 6 3852–3864.

[154] Q. Ouyang, J. Wu, Z. Shao, D. Chen, and J. W. Bisley, *A simplified model for simulating population responses of tactile afferents and receptors in the skin*, *IEEE Transactions on Biomedical Engineering* **68** (2021), no. 2 556–567.

[155] B. P. Delhaye, X. Xia, and S. J. Bensmaia, *Rapid geometric feature signaling in the simulated spiking activity of a complete population of tactile nerve fibers*, *Journal of Neurophysiology* **121** (2019), no. 6 2071–2082.

[156] J. Carriot, M. Jamali, M. J. Chacron, and K. E. Cullen, *Statistics of the vestibular input experienced during natural self-motion: Implications for neural processing*, *Journal of Neuroscience* **34** (2014), no. 24 8347–8357.

[157] P. Dallos, *The active cochlea*, *Journal of Neuroscience* **12** (1992), no. 12 4575–4585.

[158] S. S. Narayan, A. Temchin, A. Recio, and M. Ruggero, *Frequency tuning of basilar membrane and auditory nerve fibers in the same cochleae*, *Science* **282** (1998), no. 5395 1882–1884.

[159] J. Ruberti, A. S. Roy, and C. Roberts, *Corneal biomechanics and biomaterials.*, *Annual Review of Biomedical Engineering* **13** (2011) 269–95.

[160] P. Donaldson, A. Grey, B. M. Heilman, J. C. Lim, and E. Vaghefi, *The physiological optics of the lens*, *Progress in Retinal and Eye Research* **56** (2017) e1–e24.

[161] T. Furuta, N. E. Bush, A. E.-T. Yang, S. Ebara, N. Miyazaki, K. Murata, D. Hirai, K.-i. Shibata, and M. J. Z. Hartmann, *The cellular and mechanical basis for response characteristics of identified primary afferents in the rat vibrissal system*, *Current Biology* **30** (2020), no. 5 815–826.e5.

[162] Y. Ding and Y. Vlasov, *Pre-neuronal processing of haptic sensory cues via dispersive high-frequency vibrational modes*, *Scientific Reports* **13** (2023), no. 1 14370.

[163] K. Bagdasarian, M. Szwed, P. M. Knutsen, D. Deutsch, D. Derdikman, M. Pietr, E. Simony, and E. Ahissar, *Pre-neuronal morphological processing of object location by individual whiskers*, *Nature Neuroscience* **16** (2013), no. April 622–631.

[164] D. Edwards, *Neuromechanical simulation*, *Frontiers in Behavioral Neuroscience* **4** (2010) 40.

[165] S. P. Sane and M. J. McHenry, *The biomechanics of sensory organs*, *Integrative and Comparative Biology* **49** (2009), no. 6 i8–i23.

[166] A. Astreinidi Blandin, I. Bernardeschi, and L. Beccai, *Biomechanics in soft mechanical sensing: From natural case studies to the artificial world*, *Biomimetics* **3** (2018), no. 44 32.

[167] A. J. Hudspeth, *How the ear's works work*, *Nature* **341** (1989), no. 6241 397–404.

[168] R. W. Blob, K. M. Diamond, R. Lagarde, T. Maie, K. N. Moody, A. M. Palecek, J. L. Ward, and H. L. Schoenfuss, *Integrating biomechanics in evolutionary studies, with examples from the amphidromous goby model system*, *Journal of Experimental Biology* **226** (2023), no. Suppl_1 jeb244942.

[169] G. Taylor and A. Thomas, *Evolutionary Biomechanics*. Oxford University Press, 2014.

[170] D. P. Piñero and N. Alcón, *Corneal biomechanics: A review*, *Clinical and Experimental Optometry* **98** (2015), no. 2 107–116.

[171] T. Someya, T. Sekitani, S. Iba, Y. Kato, H. Kawaguchi, and T. Sakurai, *A large-area, flexible pressure sensor matrix with organic field-effect transistors for artificial skin applications*, *Proceedings of the National Academy of Sciences* **101** (2004), no. 27 9966–9970.

[172] J. H. Solomon and M. J. Z. Hartmann, *Robotic whiskers used to sense features*, *Nature* **443** (2006), no. 7111 525.

[173] W. T. Catton, *A comparison of the responses of frog skin receptors to mechanical and electrical stimulation*, *The Journal of Physiology* **187** (1966), no. 1 23–33.

[174] B. H. Pubols, *Effect of mechanical stimulus spread across glabrous skin of raccoon and squirrel monkey hand on tactile primary afferent fiber discharge*, *Somatosensory Research* **4** (1987), no. 4 273–308.

[175] H. P. Saal, I. Birznieks, and R. S. Johansson, *Memory at your fingertips: how viscoelasticity affects tactile neuron signaling*, *eLife* **12** (2023).

[176] K. J. Sandbrink, P. Mamidanna, C. Michaelis, M. Bethge, M. W. Mathis, and A. Mathis, *Contrasting action and posture coding with hierarchical deep neural network models of proprioception*, *eLife* **12** (2023) e81499.

[177] A. M. Vargas, A. Bisi, A. S. Chiappa, C. Versteeg, L. E. Miller, and A. Mathis, *Task-driven neural network models predict neural dynamics of proprioception*, *Cell* **187** (2024), no. 7 1745–1761.

[178] C. Escoffier, J. de Rigal, A. Rochefort, R. Vasselet, J.-L. Lévêque, and P. G. Agache, *Age-related mechanical properties of human skin: an in vivo study*, *Journal of Investigative Dermatology* **93** (1989), no. 3 353–357.

[179] M. Djaghloul, A. Abdouni, C. Thieulin, and H. Zahouani, *Wave propagation as a marker of structural and topographic properties of human skin*, *Surface Topography: Metrology and Properties* **6** (2018), no. 2 024008.

[180] J. Decorps, J. L. Saumet, P. Sommer, D. Sigaudo-Roussel, and B. Fromy, *Effect of ageing on tactile transduction processes*, *Ageing Research Reviews* **13** (2014) 90–99.

[181] R. T. Verrillo, S. J. Bolanowski, and G. A. Gescheider, *Effect of aging on the subjective magnitude of vibration*, *Somatosensory & Motor Research* **19** (2002), no. 3 238–244.

[182] J. C. Stevens, *Aging and spatial acuity of touch*, *Journal of Gerontology* **47** (1992), no. 1 P35–P40.

[183] Y. Zhang, W. Kienzle, Y. Ma, S. S. Ng, H. Benko, and C. Harrison, *ActiTouch: Robust touch detection for on-skin AR/VR interfaces*, in *Proceedings of the 32nd Annual ACM Symposium on User Interface Software and Technology*, UIST '19, (New Orleans, LA, USA), pp. 1151–1159, Association for Computing Machinery, 2019.

[184] A. R. Kao, C. Xu, and G. J. Gerling, *Using digital image correlation to quantify skin deformation with von frey monofilaments*, *IEEE Transactions on Haptics* **15** (2021), no. 1 26–31.

[185] R. G. Dong, J. Z. Wu, X. S. Xu, D. E. Welcome, and K. Krajnak, *A review of hand-arm vibration studies conducted by US NIOSH since 2000*, *Vibration* **4** (2021), no. 2 482–528.

[186] K. Ziegler-Graham, E. J. MacKenzie, P. L. Ephraim, T. G. Travison, and R. Brookmeyer, *Estimating the prevalence of limb loss in the United States: 2005 to 2050*, *Archives of Physical Medicine and Rehabilitation* **89** (2008), no. 3 422–429.

[187] M. C. Day, R. Wadey, and S. Strike, *Living with limb loss: everyday experiences of "good" and "bad" days in people with lower limb amputation*, *Disability and Rehabilitation* **41** (2018), no. 20 2433–2442.

[188] J. W. Sensinger and S. Dosen, *A review of sensory feedback in upper-limb prostheses from the perspective of human motor control*, *Frontiers in Neuroscience* **14** (2020).

[189] R. Ackerley and A. Kavounoudias, *The role of tactile afference in shaping motor behaviour and implications for prosthetic innovation*, *Neuropsychologia* **79** (2015) 192–205.

[190] E. L. Graczyk, A. Gill, D. J. Tyler, and L. J. Resnik, *The benefits of sensation on the experience of a hand: A qualitative case series*, *PLOS ONE* **14** (2019), no. 1 e0211469.

[191] M. A. Schiefer, E. L. Graczyk, S. M. Sidik, D. W. Tan, and D. J. Tyler, *Artificial tactile and proprioceptive feedback improves performance and confidence on object identification tasks*, *PloS One* **13** (2018), no. 12 e0207659.

[192] P. Svensson, U. Wijk, A. Björkman, and C. Antfolk, *A review of invasive and non-invasive sensory feedback in upper limb prostheses*, *Expert Review of Medical Devices* **14** (2017), no. 6 439–447.

[193] C. Antfolk, M. D'alonzo, B. Rosén, G. Lundborg, F. Sebelius, and C. Cipriani, *Sensory feedback in upper limb prosthetics*, *Expert Review of Medical Devices* **10** (2013), no. 1 45–54.

[194] K. Kim, *A review of haptic feedback through peripheral nerve stimulation for upper extremity prosthetics*, *Current Opinion in Biomedical Engineering* **21** (2022).

[195] T. Alldridge, M. Barlow, X. X. Teh, E. Barker, S. Sutherland-Dee, and A. Roudaut, *PaNDa-Glove: A sensory substitution glove for peripheral neuropathy*, in *Extended Abstracts of the 2020 CHI Conference on Human Factors in Computing Systems*, CHI EA '20, (New York, NY, USA), pp. 1–7, Association for Computing Machinery, 2020.

[196] D. M. Wrisley, G. McLean, and L. I. Oddsson, *Long-term use of a sensory prosthesis improves function in a patient with peripheral neuropathy: A case report*, *Frontiers in Neurology* **12** (2021).

[197] S. Raspopovic, G. Valle, and F. M. Petrini, *Sensory feedback for limb prostheses in amputees*, *Nature Materials* **20** (2021) 925–939.

[198] L. E. Osborn, R. Kaliki, A. Soares, and N. Thakor, *Neuromimetic event-based detection for closed-loop tactile feedback control of upper limb prostheses*, *IEEE Transactions on Haptics* **9** (2016), no. 2 196–206.

[199] G. Valle, A. Mazzoni, F. Iberite, E. D'Anna, I. Strauss, G. Granata, M. Controzzi, F. Clemente, G. Rognini, C. Cipriani, *et. al.*, *Biomimetic intraneural sensory feedback enhances sensation naturalness, tactile sensitivity, and manual dexterity in a bidirectional prosthesis*, *Neuron* **100** (2018), no. 1.

[200] G. Valle, N. Katic Secerovic, D. Eggemann, O. Gorskii, N. Pavlova, F. M. Petrini, P. Cvancara, T. Stieglitz, P. Musienko, M. Bumbasirevic, and S. Raspopovic, *Biomimetic computer-to-brain communication enhancing naturalistic touch sensations via peripheral nerve stimulation*, *Nature Communications* **15** (2024).

[201] J. A. George, D. T. Kluger, T. S. Davis, S. M. Wendelken, E. V. Okorokova, Q. He, C. C. Duncan, D. T. Hutchinson, Z. C. Thumser, D. T. Beckler, P. D. Marasco, S. J. Bensmaia, and G. A. Clark, *Biomimetic sensory feedback through peripheral nerve stimulation improves dexterous use of a bionic hand*, *Science Robotics* **4** (2019), no. 32 eaax2352.

[202] S. S. Kim, A. P. Sripati, R. J. Vogelstein, R. S. Armiger, A. F. Russell, and S. J. Bensmaia, *Conveying tactile feedback in sensorized hand neuroprostheses using a biofidelic model of mechanotransduction*, *IEEE Transactions on Biomedical Circuits and Systems* **3** (2009), no. 6 398–404.

[203] S. J. Bensmaia, *Biological and bionic hands: Natural neural coding and artificial perception*, *Philosophical Transactions of the Royal Society B: Biological Sciences* **370** (2015), no. 1677.

[204] E. V. Okorokova, Q. He, and S. J. Bensmaia, *Biomimetic encoding model for restoring touch in bionic hands through a nerve interface*, *Journal of Neural Engineering* **15** (2018), no. 6.

[205] H. Yousef, M. Boukallel, and K. Althoefer, *Tactile sensing for dexterous in-hand manipulation in robotics–A review*, *Sensors and Actuators A: Physical* **167** (2011), no. 2 171–187.

[206] R. Balasubramanian and V. J. Santos, eds., *The Human Hand as an Inspiration for Robot Hand Development*, vol. 95 of *Springer Tracts in Advanced Robotics*. Springer Cham, 2014.

[207] J. Dargahi and S. Najarian, *Human tactile perception as a standard for artificial tactile sensing–A review*, *The International Journal of Medical Robotics and Computer Assisted Surgery* **1** (2004), no. 1 23–35.

[208] L. Wang, L. Ma, J. Yang, and J. Wu, *Human somatosensory processing and artificial somatosensation*, *Cyborg and Bionic Systems* **2021** (2021).

[209] S. Sundaram, *How to improve robotic touch*, *Science* **370** (2020), no. 6518 768–769.

[210] F. Liu, S. Deswal, A. Christou, Y. Sandamirskaya, M. Kaboli, and R. Dahiya, *Neuro-inspired electronic skin for robots*, *Science Robotics* **7** (2022), no. 67 eabl7344.

[211] S. Chun, J.-S. Kim, Y. Yoo, Y. Choi, S. J. Jung, D. Jang, G. Lee, K.-I. Song, K. S. Nam, I. Youn, *et. al.*, *An artificial neural tactile sensing system*, *Nature Electronics* **4** (2021), no. 6 429–438.

[212] W. W. Lee, Y. J. Tan, H. Yao, S. Li, H. H. See, M. Hon, K. A. Ng, B. Xiong, J. S. Ho, and B. C. K. Tee, *A neuro-inspired artificial peripheral nervous system for scalable electronic skins*, *Science Robotics* **4** (2019), no. 32 eaax2198.

[213] Z. Yi, Y. Zhang, and J. Peters, *Biomimetic tactile sensors and signal processing with spike trains: A review*, *Sensors and Actuators A: Physical* **269** (2018) 41–52.

[214] H. Nguyen, L. Osborn, M. Iskarous, C. Shallal, C. Hunt, J. Betthauser, and N. Thakor, *Dynamic texture decoding using a neuromorphic multilayer tactile sensor*, in *2018 IEEE Biomedical Circuits and Systems Conference (BioCAS)*, pp. 1–4, 2018.

[215] M. M. Iskarous and N. V. Thakor, *E-skins: Biomimetic sensing and encoding for upper limb prostheses*, *Proceedings of the IEEE* **107** (2019), no. 10 2052–2064.

[216] K. E. Friedl, A. R. Voelker, A. Peer, and C. Eliasmith, *Human-inspired neurorobotic system for classifying surface textures by touch*, *IEEE Robotics and Automation Letters* **1** (2016), no. 1 516–523.

[217] J. M. Romano, K. Hsiao, G. Niemeyer, S. Chitta, and K. J. Kuchenbecker, *Human-inspired robotic grasp control with tactile sensing*, *IEEE Transactions on Robotics* **27** (2011), no. 6 1067–1079.

[218] U. B. Rongala, A. Mazzoni, D. Camboni, M. C. Carrozza, and C. M. Oddo, *Neuromorphic Artificial Sense of Touch: Bridging Robotics and Neuroscience*, pp. 617–630. Springer Proceedings in Advanced Robotics. Springer International Publishing, Cham, 2018.

[219] L. Chen, S. Karilanova, S. Chaki, C. Wen, L. Wang, B. Winblad, S.-L. Zhang, A. Özçelikkale, and Z.-B. Zhang, *Spike timing–based coding in neuromimetic tactile system enables dynamic object classification*, *Science* **384** (2024), no. 6696 660–665.

[220] H. Sun and G. Martius, *Guiding the design of superresolution tactile skins with taxel value isolines theory*, *Science Robotics* **7** (2022), no. 63 eabm0608.

[221] J. Bergström and K. Hornbæk, *Human-computer interaction on the skin*, *ACM Computing Surveys* **52** (2019), no. 4.

[222] T. Iwamoto and H. Shinoda, *Finger ring tactile interface based on propagating elastic waves on human fingers*, in *Second Joint EuroHaptics Conference and Symposium on Haptic Interfaces for Virtual Environment and Teleoperator Systems (WHC'07)*, pp. 145–150, 2007.

[223] A. Mujibiya, X. Cao, D. S. Tan, D. Morris, S. N. Patel, and J. Rekimoto, *The sound of touch: On-body touch and gesture sensing based on transdermal ultrasound propagation*, in *Proceedings of the 2013 ACM International Conference on Interactive Tabletops and Surfaces*, ITS '13, (St. Andrews, Scotland, United Kingdom), pp. 189–198, Association for Computing Machinery, 2013.

[224] J. Gong, A. Gupta, and H. Benko, *Acustico: Surface tap detection and localization using wrist-based acoustic TDOA sensing*, in *Proceedings of the 33rd Annual ACM Symposium on User Interface Software and Technology*, UIST '20, (New York, NY, USA), pp. 406–419, Association for Computing Machinery, 2020.

[225] V. A. Shah, M. Casadio, R. A. Scheidt, and L. A. Mrotek, *Vibration propagation on the skin of the arm*, *Applied Sciences* **9** (2019), no. 20.

[226] T. Hachisu, G. Reardon, Y. Shao, K. Suzuki, and Y. Visell, *Interpersonal transmission of vibrotactile feedback via smart bracelets: Mechanics and perception*, *IEEE Transactions on Haptics* (2023) 1–13.

[227] V. de Vlam, M. Wiertlewski, and Y. Vardar, *Focused vibrotactile stimuli from a wearable sparse array of actuators*, *IEEE Transactions on Haptics* **16** (2023), no. 4 511–517.

[228] J. J. Gibson, *The Senses Considered as Perceptual Systems*. Houghton Mifflin Co, 1966.

[229] R. T. Verrillo, G. A. Gescheider, B. G. Calman, and C. L. Van Doren, *Vibrotactile masking: Effects of one and two-site stimulation*, *Perception & Psychophysics* **33** (1983), no. 4 379–387.

[230] R. D. Gilson, *Vibrotactile masking: Some spatial and temporal aspects*, *Perception & Psychophysics* **5** (1969), no. 3 176–180.

[231] J. E. Gregory, A. K. McIntyre, and U. Proske, *Vibration-evoked responses from lamellated corpuscles in the legs of kangaroos*, *Experimental Brain Research* **62** (1986), no. 3 648–653.

[232] D. Bouley, C. Alarcon, T. Hildebrandt, and C. E. O'Connell-Rodwell, *The distribution, density and three-dimensional histomorphology of Pacinian corpuscles in the foot of the Asian elephant (Elephas maximus) and their potential role in seismic communication*, *Journal of Anatomy* **211** (2007), no. 4 428–435.

[233] J. Morley, M. Hawken, and P. Burge, *Vibratory detection thresholds following a digital nerve lesion*, *Experimental Brain Research* **72** (1988) 215–218.

[234] D. A. Mahns, N. M. Perkins, V. Sahai, L. Robinson, and M. J. Rowe, *Vibrotactile frequency discrimination in human hairy skin*, *Journal of Neurophysiology* **95** (2006), no. 3 1442–1450.

[235] S. S. Stevens, *Tactile vibration: Change of exponent with frequency*, *Perception & Psychophysics* **3** (1968), no. 3 223–228.

[236] R. T. Verrillo, A. J. Fraioli, and R. L. Smith, *Sensation magnitude of vibrotactile stimuli*, *Perception & Psychophysics* **6** (1969), no. 6 366–372.

[237] G. von Békésy, *Human skin perception of traveling waves similar to those on the cochlea*, *The Journal of the Acoustical Society of America* **27** (1955), no. 5 830–841.

[238] H. Saal, X. Wang, and S. Bensmaia, *Importance of spike timing in touch: An analogy with hearing?*, *Current Opinion in Neurobiology* **40** (2016) 142–149.

[239] J. Timmer and M. König, *On generating power law noise*, *Astronomy and Astrophysics* **300** (1995) 707–710.

[240] H. P. Saal, M. A. Harvey, and S. J. Bensmaia, *Rate and timing of cortical responses driven by separate sensory channels*, *eLife* **4** (2015) e10450.

[241] K. H. Long, J. D. Lieber, and S. J. Bensmaia, *Texture is encoded in precise temporal spiking patterns in primate somatosensory cortex*, *Nature Communications* **13** (2022), no. 1 1311.

[242] W. Bair, E. Zohary, and W. T. Newsome, *Correlated firing in macaque visual area MT: Time scales and relationship to behavior*, *Journal of Neuroscience* **21** (2001), no. 5 1676–1697.

[243] A. Kohn and M. A. Smith, *Stimulus dependence of neuronal correlation in primary visual cortex of the macaque*, *Journal of Neuroscience* **25** (2005), no. 14 3661–3673.

[244] M. R. Cohen and A. Kohn, *Measuring and interpreting neuronal correlations*, *Nature Neuroscience* **14** (2011), no. 7 811–819.

[245] M. Denker, A. Yegenoglu, and S. Grün, *Collaborative HPC-enabled workflows on the HBP Collaboratory using the Elephant framework*, in *Neuroinformatics 2018*, p. P19, 2018.

[246] S. J. Bensmaia, *Tactile intensity and population codes*, *Behavioural Brain Research* **190** (2008), no. 2 165–173.

[247] E. Hay and J. A. Pruszynski, *Orientation processing by synaptic integration across first-order tactile neurons*, *PLOS Computational Biology* **16** (2020), no. 12 e1008303.

[248] G. Foffani and K. A. Moxon, *PSTH-based classification of sensory stimuli using ensembles of single neurons*, *Journal of Neuroscience Methods* **135** (2004), no. 1 107–120.

[249] G. Foffani, J. K. Chapin, and K. A. Moxon, *Computational role of large receptive fields in the primary somatosensory cortex*, *Journal of Neurophysiology* **100** (2008), no. 1 268–280.

[250] A. J. Brockmeier, J. S. Choi, E. G. Kriminger, J. T. Francis, and J. C. Principe, *Neural decoding with kernel-based metric learning*, *Neural Computation* **26** (2014), no. 6 1080–1107.

[251] E. Satuvuori, M. Mulansky, A. Daffertshofer, and T. Kreuz, *Using spike train distances to identify the most discriminative neuronal subpopulation*, *Journal of Neuroscience Methods* **308** (2018) 354–365.

[252] F. Gonzalez, F. Gosselin, and W. Bachta, *Analysis of hand contact areas and interaction capabilities during manipulation and exploration*, *IEEE Transactions on Haptics* **7** (2014), no. 4 415–429.

[253] M. Sur, *Receptive fields of neurons in areas 3b and 1 of somatosensory cortex in monkeys*, *Brain research* **198** (1980), no. 2 465–471.

[254] R. S. Johansson and I. Birznieks, *First spikes in ensembles of human tactile afferents code complex spatial fingertip events*, *Nature neuroscience* **7** (2004), no. 2 170–177.

[255] F. Bengtsson, R. Brasselet, R. S. Johansson, A. Arleo, and H. Jörntell, *Integration of sensory quanta in cuneate nucleus neurons in vivo*, *PloS one* **8** (2013), no. 2 e56630.

[256] E. P. Gardner and R. M. Costanzo, *Spatial integration of multiple-point stimuli in primary somatosensory cortical receptive fields of alert monkeys*, *Journal of Neurophysiology* **43** (1980), no. 2 420–443.

[257] E. P. Gardner and R. M. Costanzo, *Temporal integration of multiple-point stimuli in primary somatosensory cortical receptive fields of alert monkeys*, *Journal of Neurophysiology* **43** (1980), no. 2 444–468.

[258] C. M. Reed, W. M. Rabinowitz, N. I. Durlach, L. D. Braida, S. Conway-Fithian, and M. C. Schultz, *Research on the tadoma method of speech communication*, *The Journal of the Acoustical Society of America* **77** (1985), no. 1 247–257.

[259] C. M. Reed, L. A. Delhorne, N. I. Durlach, and S. D. Fischer, *A study of the tactual and visual reception of fingerspelling*, *Journal of Speech, Language, and Hearing Research* **33** (1990), no. 4 786–797.

[260] J. M. Loomis, *On the tangibility of letters and braille*, *Perception & Psychophysics* **29** (1981), no. 1 37–46.

[261] H. Nicolau, K. Montague, T. Guerreiro, A. Rodrigues, and V. L. Hanson, *HoliBraille: Multipoint vibrotactile feedback on mobile devices*, in *Proceedings of the 12th International Web for All Conference*, no. 30 in W4A '15, (Florence, Italy), pp. 1–4, Association for Computing Machinery, 2015.

[262] U. Gollner, T. Bieling, and G. Joost, *Mobile Lorm Glove: Introducing a communication device for deaf-blind people*, in *Proceedings of the Sixth International Conference on Tangible, Embedded and Embodied Interaction*, TEI '12, pp. 127–130, Association for Computing Machinery, 2012.

[263] B. Duvernoy, I. Farkhatdinov, S. Topp, and V. Hayward, *Electromagnetic actuator for tactile communication*, in *Haptics: Science, Technology, and Applications* (D. Prattichizzo, H. Shinoda, H. Z. Tan, E. Ruffaldi, and A. Frisoli, eds.), Lecture Notes in Computer Science, (Pisa, Italy), pp. 14–24, Springer Cham, 2018.

[264] H. Z. Tan, C. M. Reed, Y. Jiao, Z. D. Perez, E. C. Wilson, J. Jung, J. S. Martinez, and F. M. Severgnini, *Acquisition of 500 english words through a TActile Phonemic Sleeve (TAPS)*, *IEEE Transactions on Haptics* **13** (2020), no. 4 745–760.

[265] C. Vogler and D. Metaxas, *Parallel hidden Markov models for American sign language recognition*, in *Proceedings of the Seventh IEEE International Conference on Computer Vision*, vol. 1, (Kerkyra, Greece), pp. 116–122, 1999.

[266] B. Duvernoy, S. Topp, and V. Hayward, *"HaptiComm", a haptic communicator device for deafblind communication*, in *Haptic Interaction* (H. Kajimoto, D. Lee, S.-Y. Kim, M. Konyo, and K.-U. Kyung, eds.), Lecture Notes in Electrical Engineering, (Incheon, Korea), pp. 112–115, Springer Singapore, 2018.

[267] A. Theil, L. Buchweitz, J. Gay, E. Lindell, L. Guo, N.-K. Persson, and O. Korn, *Tactile Board: A multimodal augmentative and alternative communication device for individuals with deafblindness*, in *Proceedings of the 19th International Conference on Mobile and Ubiquitous Multimedia*, MUM '20, (Essen, Germany), pp. 223–228, Association for Computing Machinery, 2020.

[268] S. Sundaram, P. Kellnhofer, Y. Li, J.-Y. Zhu, A. Torralba, and W. Matusik, *Learning the signatures of the human grasp using a scalable tactile glove*, *Nature* **569** (2019), no. 7758 698–702.

[269] R. Booth and P. Goldsmith, *A wrist-worn piezoelectric sensor array for gesture input*, *Journal of Medical and Biological Engineering* **38** (2018), no. 2 284–295.

[270] S. Fani, K. D. Blasio, M. Bianchi, M. G. Catalano, G. Grioli, and A. Bicchi, *Relaying the high-frequency contents of tactile feedback to robotic prosthesis users: Design, filtering, implementation, and validation*, *IEEE Robotics and Automation Letters* **4** (2019), no. 2 926–933.

[271] T. Hachisu, G. Reardon, Y. Shao, K. Suzuki, and Y. Visell, *Interpersonal vibrotactile feedback via waves transmitted through the skin: Mechanics and perception*, in *2020 IEEE Haptics Symposium*, (Washington, DC, USA), pp. 650–656, 2020.

[272] A. Z. Hajian and R. D. Howe, *Identification of the mechanical impedance at the human finger tip*, *Journal of Biomechanical Engineering* **119** (1997), no. 1 109–114.

[273] T. Tsuji, P. G. Morasso, K. Goto, and K. Ito, *Human hand impedance characteristics during maintained posture*, *Biological Cybernetics* **72** (1995) 475–485.

[274] H. Culbertson, J. J. López Delgado, and K. J. Kuchenbecker, *One hundred data-driven haptic texture models and open-source methods for rendering on 3D objects*, in *2014 IEEE Haptics Symposium*, (Houston, TX, USA), pp. 319–325, 2014.

[275] A. Devillard, A. Ramasamy, D. Faux, V. Hayward, and E. Burdet, *Concurrent haptic, audio, and visual data set during bare finger interaction with textured surfaces*, in *2023 IEEE World Haptics Conference*, (Delft, Netherlands), pp. 101–106, IEEE, 2023.

[276] V. Vechev, J. Zarate, D. Lindlbauer, R. Hinchet, H. Shea, and O. Hilliges, *Tactiles: Dual-mode low-power electromagnetic actuators for rendering continuous contact and spatial haptic patterns in VR*, in *2019 IEEE Conference on Virtual Reality and 3D User Interfaces*, pp. 312–320, IEEE, 2019.

[277] S. J. Bensmaia and M. Hollins, *Complex tactile waveform discrimination*, *The Journal of the Acoustical Society of America* **108** (2000), no. 3 1236–1245.

[278] K. Darvish and J. Crandall, *Nonlinear viscoelastic effects in oscillatory shear deformation of brain tissue*, *Medical Engineering & Physics* **23** (2001), no. 9 633–645.

[279] H. Møller, M. F. Sørensen, C. B. Jensen, and D. Hammershøi, *Binaural technique: Do we need individual recordings?*, *Journal of the Audio Engineering Society* **44** (1996), no. 6 451–469.

[280] K. Iida, Y. Ishii, and S. Nishioka, *Personalization of head-related transfer functions in the median plane based on the anthropometry of the listener's pinnae*, *The Journal of the Acoustical Society of America* **136** (2014), no. 1 317–333.

[281] E. A. Torres-Gallegos, F. Orduna-Bustamante, and F. Arámbula-Cosío, *Personalization of head-related transfer functions (HRTF) based on automatic photo-anthropometry and inference from a database*, *Applied Acoustics* **97** (2015) 84–95.

[282] G. von Békésy, *Similarities between hearing and skin sensations.*, *Psychological Review* **66** (1959), no. 1 1.